

# Quantitative structure–property relationship modelling for the prediction of singlet oxygen generation by heavy-atom-free BODIPY photosensitizers

Andrey A. Buglak,<sup>[a]</sup> Asterios Charisiadis,<sup>[b]</sup> Aimee Sheehan,<sup>[c]</sup> Christopher J. Kingsbury,<sup>[c]</sup> Mathias O. Senge\*<sup>[d]</sup> and Mikhail A. Filatov\*<sup>[c]</sup>

- [a] Dr. Andrey A. Buglak  
Faculty of Physics, Saint-Petersburg State University, University Emb. 7-9, 199034 St. Petersburg, Russia
- [b] Dr. Asterios Charisiadis, Dr. Christopher J. Kingsbury  
Chair of Organic Chemistry, School of Chemistry, Trinity Biomedical Sciences Institute, Trinity College Dublin, The University of Dublin, 152-160 Pearse Street, Dublin 2, Ireland
- [c] Aimee Sheehan, Dr. Mikhail A. Filatov  
School of Chemical and Pharmaceutical Sciences, Technological University Dublin, City Campus, Kevin Street, Dublin 8, Ireland  
E-mail: mikhail.filatov@tudublin.ie
- [d] Prof. Dr. Mathias O. Senge  
Institute for Advanced Study (TUM-IAS), Technical University of Munich, Lichtenberg-Str. 2a, 85748 Garching, Germany  
E-mail: [sengem@tcd.ie](mailto:sengem@tcd.ie); twitter: @mathiassenge

Supporting information for this article is given via a link at the end of the document.

**Abstract:** Heavy-atom-free sensitizers forming long-living triplet excited states *via* the spin-orbit charge transfer intersystem crossing (SOCT-ISC) process have recently attracted attention due to their potential to replace costly transition metal complexes in photonic applications. The efficiency of SOCT-ISC in BODIPY donor-acceptor dyads, so far the most thoroughly investigated class of such sensitizers, can be finely tuned by structural modification. However, predicting the triplet state yields and reactive oxygen species (ROS) generation quantum yields for such compounds in a particular solvent is still very challenging due to a lack of established quantitative structure-property relationship (QSPR) models. Herein, we analyzed the available data on singlet oxygen generation quantum yields ( $\Phi_{\Delta}$ ) for a dataset containing > 70 heavy-atom-free BODIPY in three different solvents (toluene, acetonitrile, and tetrahydrofuran). In order to build reliable QSPR model, we synthesized a series of new BODIPYs containing different electron donating aryl groups in the *meso* position, studied their optical and structural properties along with the solvent dependence of singlet oxygen generation, which confirmed the formation of triplet states *via* the SOCT-ISC mechanism. For the combined dataset of BODIPY structures, a total of more than 5000 quantum-chemical descriptors was calculated including quantum-chemical descriptors using Density Functional Theory (DFT), namely M06-2X functional. QSPR models predicting  $\Phi_{\Delta}$  values were developed using multiple linear regression (MLR), which perform significantly better than other machine learning methods and show sufficient statistical parameters ( $R = 0.88\text{--}0.91$  and  $q^2 = 0.62\text{--}0.69$ ) for all three solvents. A small root mean squared error of 8.2% was obtained for  $\Phi_{\Delta}$  values predicted using MLR model in toluene. As a result, we proved that QSPR and machine learning techniques can be useful for predicting  $\Phi_{\Delta}$  values in different media and virtual screening of new heavy-atom-free BODIPYs with improved photosensitizing ability.

## Introduction

Photosensitizers (PSs) which efficiently form long-lived triplet excited states are crucially important in such fields as photoredox catalysis,<sup>1</sup> photodynamic therapy (PDT)<sup>2</sup> and triplet-triplet annihilation upconversion.<sup>3</sup> Common approach for enhancing the triplet state yield ( $\Phi_T$ ) in organic chromophores relies on the introduction of heavy atoms, such as halogens (Br or I) or transition metals (e.g., Ru, Pd or Pt) in the structure (Figure 1A), which promote the intersystem crossing process *via* spin-orbit coupling interactions.<sup>4</sup> However, introduction of heavy atoms often requires tedious synthesis and thus leads to high cost of such photosensitizers.<sup>5</sup> Moreover, the presence of heavy atoms can also result in shortening the triplet state lifetimes.<sup>6</sup> The replacement of costly transition metal complexes in industrial-scale photocatalytic processes with organic PSs has drawn considerable attention,<sup>7</sup> and has stimulated a search for alternative methods to promote ISC, not relying on the heavy atom effect, e.g., using a spin converter,<sup>8</sup> exciton coupling,<sup>9</sup> doubly-substituted excited states,<sup>10</sup> twisting of the aromatic systems<sup>11</sup> and radical-induced ISC have been very actively studied in recent years.<sup>12</sup>

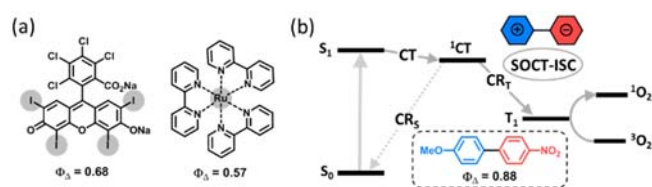


**Figure 1.** (a) Examples of heavy-atom-containing dyes.  $\Phi_{\Delta}$  – singlet oxygen quantum yield. (b) Jablonski diagram illustrating the formation of triplet excited state *via* the SOCT-ISC mechanism.

The formation of triplet excited states in electron donor-acceptor dyads *via* the process of spin-orbit charge transfer intersystem crossing (SOCT-ISC) does not require introduction of transition metals or other heavy atoms into the molecule. So far, it has

been observed in donor-acceptor dyads based on BODIPYs<sup>13</sup> and other difluoroboron complexes,<sup>14</sup> metal dipyrins,<sup>15</sup> phenoxazines,<sup>16</sup> biphenyls,<sup>17</sup> naphthalene and perylene imides.<sup>18</sup> In these molecules, photoinduced electron transfer between the donor and acceptor subunits leads to formation of a charge-transfer state (CT), which further undergoes a non-radiative charge recombination into the ground state (CR<sub>s</sub>) or into the lowest triplet excited state (CR<sub>T</sub>) via SOCT-ISC (Figure 1B).<sup>19</sup> The latter process is commonly observed for dyads with orthogonal mutual arrangement of donor and acceptor subunits, which induces a large variation of the orbital magnetic momentum during the recombination process and thus compensates the change of spin magnetic momentum.<sup>20</sup> High yields of triplet state formation are observed for molecules in which the CT state lies close in energy to the lowest singlet excited state (S<sub>1</sub>). In this case, the CR<sub>s</sub> process falls within the Marcus inverted region<sup>21</sup> and is relatively slow due to a large negative value of the free energy change ( $\Delta G_{CRS}$ ). Under such circumstances, the CR<sub>T</sub> process is considerably faster due to a smaller energy gap between the CT state and the lowest triplet excited state (T<sub>1</sub>).<sup>22</sup>

Many reported molecular systems undergoing SOCT-ISC exhibit triplet state yields and singlet oxygen generation quantum yields ( $\Phi_{\Delta}$ ) values that are comparable or even higher than those of transition metal complexes and halogenated dyes. Such dyes have other important advantages, e.g., synthetic accessibility, high phototoxicity in cells (nM- $\mu$ M range) with negligible dark toxicity,<sup>23</sup> long triplet excited state lifetimes (hundreds of  $\mu$ s),<sup>24</sup> and intense absorption in the 400-600 nm region (extinction coefficients up to 10<sup>5</sup>).<sup>25</sup>

BODIPY dyes have been actively employed in the design of SOCT-ISC photosensitizers due to their excellent photophysical properties, ease of derivatization and predictable structural parameters (1464 crystal structures reported in the CCDC CSD in 2020).<sup>26</sup> In particular, a series of BODIPY dyads, containing different electron donors, such as anthracene,<sup>27</sup> pyrene,<sup>28</sup> perylene,<sup>29</sup> phenothiazine,<sup>30</sup> carbazole,<sup>31</sup> and phenoxazine<sup>32</sup> has been systematically investigated. Recently, we reported biocompatible derivatives of such dyads, bearing polar solubilizing groups for enhancing cell penetration and studied their toxicity as well as fluorogenic response to singlet oxygen in cancer cells.<sup>33</sup> A library of BODIPYs having high  $\Phi_{\Delta}$  values (up to 70%) has been screened by us as candidates for PDT with potential clinical relevance.<sup>34</sup> Concurrently, we explored application of these sensitizers in the process of triplet-triplet annihilation upconversion (TTA-UC) and showed their unprecedented dual performance, namely the ability to play a role of either a sensitizer or an emitter component, depending on the media polarity.<sup>35</sup> We also found another unique feature of BODIPY dyads – a relatively strong fluorescence from the CT state and, using this property, developed a method for precise determination of TTA-UC quantum efficiency.<sup>36</sup>

As has been shown in previous works, the key factors which affect the efficiency of SOCT-ISC in BODIPY dyads are: 1) mutual orientation of the donor and acceptor subunits; 2) values of the driving force for the charge separation and recombination processes ( $\Delta G_{CT}$  and  $\Delta G_{CR}$ , respectively); 3) the ratio between the rates of charge recombination into the ground state and into the lowest triplet excited state ( $k_{CRS}$  and  $k_{CRT}$ , respectively). Orthogonal geometry between the electron donor and the acceptor, which is beneficial for efficient SOCT-ISC, can be

secured by introduction of substituents in positions 1 and 7 of the BODIPY core. On the other hand, the rates of charge transfer and recombination steps can be modulated by varying the number of alkyl substituents, which affect the reduction potentials of the BODIPY core.<sup>37</sup> Since the energy of the CT state, and consequently  $\Delta G_{CT}$  and  $\Delta G_{CR}$  values, is strongly affected by polarity of the media, triplet state formation and generation of singlet oxygen by SOCT-ISC sensitizers is solvent-dependent. Generally, most of BODIPY dyads studied so far showed higher  $\Phi_T$  and  $\Phi_{\Delta}$  values in polar solvents, where the CT state is stabilized, and the charge transfer process is energetically favorable. However, strong stabilization of the CT state in polar media leads to a reduced CT-S<sub>0</sub> energy gap that causes enhancement of the ground state recombination rate. For this reason, many dyads show reduced  $\Phi_T$  and  $\Phi_{\Delta}$  values in highly polar solvents, such as acetonitrile or water.<sup>38</sup> In particular, for dyads bearing electron accepting groups in the BODIPY core, which stabilize the CT states, photosensitization process is more efficient in non-polar solvents (hexane, toluene).<sup>39</sup> BODIPY dimers showed highest  $\Phi_{\Delta}$  values in solvents of intermediate polarity (chloroform, THF).<sup>40</sup> Overall, predicting  $\Phi_T$  and  $\Phi_{\Delta}$  in a specific solvent is difficult and relies on test-and-trial approach. This largely limits the potential of SOCT-ISC sensitizers, for instance in advanced PDT utilizing controlled generation of cytotoxic singlet oxygen in target cells.<sup>41</sup>

Computational methods for predicting the SOCT-ISC efficiency in media of a given polarity could be valuable for pre-synthetic screening of potential sensitizer structures. However, accurate computations of charge transfer excited states and triplets formation by charge recombination using first-principle techniques are rather challenging and time-demanding.<sup>42</sup> In recent years, quantitative structure-activity relationship (QSAR) and quantitative structure-property relationship (QSPR) modelling have emerged as a useful tool for the design of fluorophores and photoactive materials.<sup>43</sup> QSAR/QSPR analysis has been applied in the studies of photophysics<sup>44</sup> and photodynamic activity of BODIPYs,<sup>45</sup> proving that “big data” approach can provide a powerful platform for the design of new photosensitizers. Yet, QSAR modelling for predicting <sup>1</sup>O<sub>2</sub> generation quantum yields is rare.<sup>46</sup> However, earlier we showed that QSPR may be used for the analysis of <sup>1</sup>O<sub>2</sub> production by perins and flavins,<sup>47</sup> psoralens and angelicins,<sup>48</sup> porphyrins and metalloporphyrins.<sup>49</sup> In this regard, applying QSPR for the prediction of  $\Phi_{\Delta}$  values for heavy-atom-free BODIPYs in solvents of different polarity offers a means to estimate SOCT-ISC efficiency in these systems. Hence, we started to search BODIPY structures which undergo SOCT-ISC to correlate molecular features to singlet oxygen quantum yields with the aid of machine learning methods. To develop a reliable model we analyzed a dataset which includes several classes of compounds (Figure 2): 1) parent BODIPY compounds with different substitution patterns; 2) BODIPY dyads with different nature, position, or number of donor/acceptor subunits; 3) symmetrical and asymmetrical BODIPY dimers; 4) a validation set comprised of a newly synthesized library of BODIPYs with various meso-methoxyphenyl groups as electron donors. Previously reported and experimentally obtained data on  $\Phi_{\Delta}$  of these molecules in solvents of different polarity – toluene (non-polar), tetrahydrofuran (moderately polar) and acetonitrile (strongly polar) were used for analysis. We performed QSPR analysis and optimized models for each solvent to ensure

sufficient statistical parameters for photosensitizing ability prediction. To our knowledge, this is the first report of a QSPR model for predicting the activity of polarity-sensitive photosensitizers. The simplicity and versatility of this approach allows for virtual screening of structures with singlet oxygen quantum yields optimized for a desired range of polarities.

SOCT-ISC photosensitizers can be activated by recognition of the appropriate environment, e.g., cell membranes<sup>50</sup> and certain proteins.<sup>51</sup> We believe that the results obtained in this work will unlock a more target-oriented exploration of this class of photosensitizers in biomedical applications relying on a controlled ROS generation.

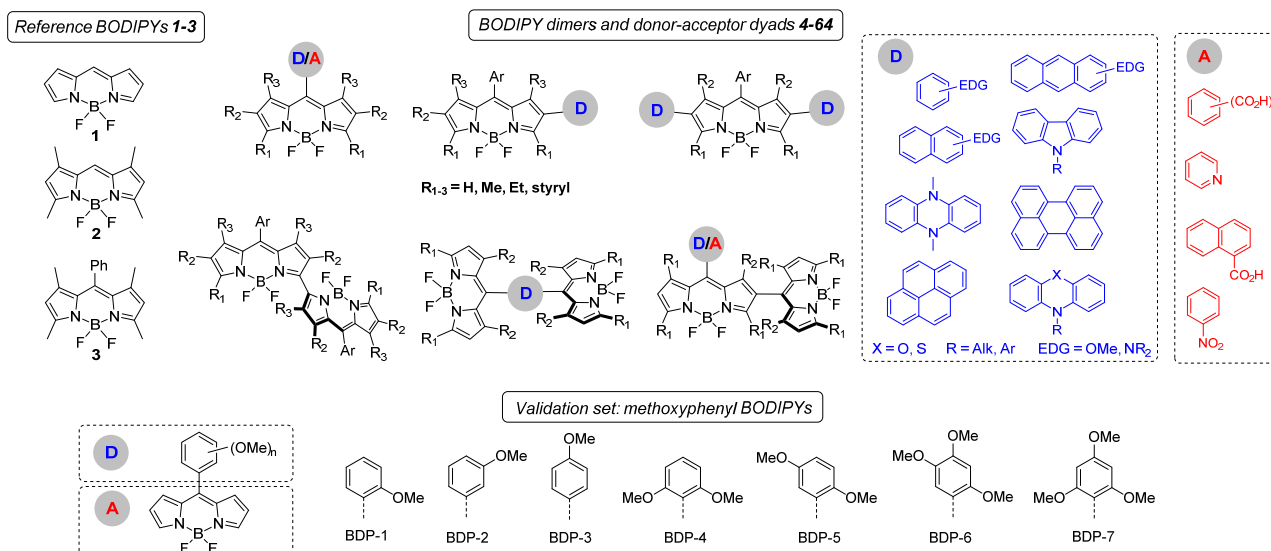


**Figure 2.** General structures of BODIPY dimers, donor-acceptor (D-A) dyads and reference compounds investigated in this work.

## Results and Discussion

### Compound dataset

The general dataset used here to build QSPR models includes compounds reported in experimental studies on triplets' formation in heavy-atom-free BODIPYs via SOCT-ISC. We examined all related works published before September 2020 and combined experimental values of  $\Phi_{\Delta}$  measured in various solvents using the method based on chemical trapping of singlet oxygen.<sup>52</sup> Several reference compounds (structures 1-3, Fig. 2) were included into the dataset to guarantee the reliability of models in cases when  $\Phi_{\Delta}$  values are very low. Other compounds in the dataset (4-64) include donor-acceptor dyads and dimers, with various substitution patterns of the BODIPY core and nature of electron donating (D) or electron accepting (A) subunits. Values of  $\Phi_{\Delta}$  measured in toluene ( $\epsilon_r = 2.4$ ), tetrahydrofuran ( $\epsilon_r = 7.6$ ), acetonitrile ( $\epsilon_r = 37.5$ ) were used for analysis since these solvents have been employed to study charge transfer and  $^1\text{O}_2$  generation for the highest number of compounds in the dataset.

To ensure the reliability of the QSPR models developed in this work for the development of practical sensitizers, several new BODIPY derivatives were also synthesized and investigated by us. BODIPY dyads bearing electron-donating aryl groups such as aminophenyl<sup>53</sup> or methoxyphenyl<sup>54</sup> groups were previously shown to undergo charge transfer and generate  $^1\text{O}_2$  both in polar and non-polar solvents. Such dyads are potentially interesting for application in PDT as alternative to cyclic

tetrapyrroles (porphyrins, chlorins, and bacteriochlorins), which often require tedious synthesis. Moreover, these common PDT agents are rather large molecules which must be injected and as a result retain in the bloodstream for long, leading to photodermatitis among other side-effects.<sup>55</sup> Thus there is a growing interest to non-porphyrin sensitizers, based on small photoactive molecules with higher absorption and excretion rates. With this in mind, we prepared compounds **BDP 1-7** (Figure 2) bearing different methoxyphenyl groups in the *meso*-position of the BODIPY core.

These seven BODIPY compounds (**BDP 1-7**) were synthesized in the stepwise manner as shown in Scheme S1. In the first step, a standard dipyrromethane synthesis was performed of each aldehyde and pyrrole in the presence of trifluoroacetic acid.<sup>56</sup> Dipyrromethanes (**DPM 1-7**) were prepared and purified by following earlier reports.<sup>57</sup> The second step involved the well-known one-pot two-step oxidation-deprotonation-complexation reaction for the synthesis of the desired BODIPY compounds.<sup>58</sup> More specifically, **DPM 1-7** derivatives were oxidized to dipyrromethenes using DDQ, which were subsequently treated with triethylamine (TEA) and  $\text{BF}_3\text{OEt}_2$ . All BODIPY products were isolated by silica gel column chromatography and final purification was performed through recrystallization in a MeOH/ $\text{H}_2\text{O}$  mixture in good to high yields. Mono-methoxy substituted BODIPY derivatives (**BDP-1**, **BDP-2** and **BDP-3**) were prepared as reference compounds following previously published procedures.<sup>59</sup>

All BODIPY compounds (**BDP 1-7**) were fully characterized through  $^1\text{H}$ ,  $^{13}\text{C}$ ,  $^{19}\text{F}$ ,  $^{11}\text{B}$  NMR spectroscopy and HRMS (see ESI). The spectroscopic data of the three reference derivatives (**BDP 1-3**) were identical with those reported previously.<sup>60</sup> The

successful formation of the final BODIPY products was confirmed by the appearance of the corresponding molecular ion peaks in their HRMS spectra. All  $^1\text{H}$  and  $^{13}\text{C}$  NMR spectroscopic data are in agreement with the proposed structures of the four newly reported compounds (**BDP 4-7**). Regarding the  $^{19}\text{F}$  NMR spectra of these four final products, the typical doublet of doublets signal<sup>61</sup> was observed for both **BDP-4** and **BDP-7** at approximately -145 ppm (Figures S3 and S18). On the other hand, the remaining two BODIPY compounds (**BDP-5** and **BDP-6**) presented two multiplets at  $\sim$ -144 and -146 ppm (Figures S8 and S13), which can be attributed to the single *ortho*-methoxy substituent forming an inequivalent environment for the F-atoms.<sup>58,62</sup> Finally, all compounds showed a typical triplet peak ( $\sim$ 0.3 ppm) in their  $^{11}\text{B}$  NMR spectra, as expected.<sup>60</sup>

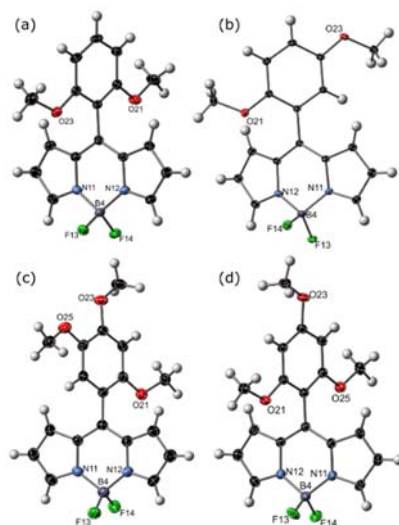


**Figure 3.** The individual molecular units of compound (a) **BDP-4**· $\frac{1}{2}$ **DCM** (solvate omitted), (b) **BDP-5**, (c) **BDP-6** and (d) **BDP-7**; thermal ellipsoids are shown at the 50% probability level, H-atoms are represented as spheres of fixed radius.

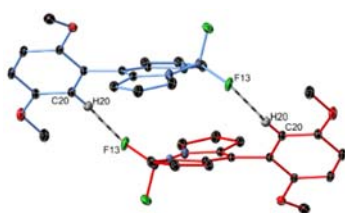


**Figure 4.** The dimeric C-H...F of 3.292 Å (C20-F13) interaction observed within the crystal structure of **BDP-5**; the symmetry-equivalent red and blue molecules are related by an inversion center. Thermal ellipsoids are shown at the 50% probability level, H-atoms not involved in this interaction have been omitted.

Furthermore, the structures of all four newly synthesized donor-acceptor dyads (**BDP 4-7**) were analyzed through single crystal X-ray crystallography. Compounds **BDP-4**, **BDP-5** and **BDP-7** were crystallized from dichloromethane at 4 °C, while **BDP-6** was crystallized from acetonitrile by slow evaporation; details of crystallographic refinement for these representative species are provided as supplementary information (Table S2). The crystal structures for **BDP 1-3** have been previously reported.<sup>58</sup>

Two crystallographically inequivalent molecules of **BDP-4** (Figure 3a), co-crystallize with a dichloromethane solvate; nearly perpendicular aryl components ( $81.54(5)^\circ$  and  $82.129(5)^\circ$  for the two inequivalent molecules) are as expected for the steric bulk of the bis(*o*-methoxy) units. This dihedral angle has been shown to be critically important for efficient SOCT-ISC process.<sup>28</sup> In **BDP-5** (Figure 3b), the aryl ring is inclined at  $50.163(13)^\circ$  to the plane of the BODIPY core. Molecules were found to adopt a dimeric arrangement in the solid state, mediated by weak aryl C-H...F of 3.292 Å (C20-F13) shown in Figure 4; the formation of dimers can modulate fluorescence behaviour.<sup>38</sup> The related compound **BDP-6** (Figure 3c) shows an aryl-BODIPY angle of  $66.14(6)^\circ$ ; although crystallizing in the chiral space-group  $P2_12_12_1$ , this compound exhibits no permanent chirality due to equivalency of the two rotamers. Close contact C-H...O interactions (3.28 Å C...O) form one-dimensional chains, shown in Figure S56. The aryl group in compound **BDP-7** (Figure 3d) is rotated  $72.04(3)^\circ$  to the BODIPY component. Molecules of **BDP-7** exhibit close  $\pi$ - $\pi$  stacks of pyrrole moieties, with a plane separation of 3.23 Å; directional C-H...F interactions are observed, at 3.316 Å C3...F14. Unit cell packing diagrams are shown in Figures S52-S55.

Increasing the number of methoxy substituents leads to reduced oxidation potentials<sup>63</sup> of the aryl subunit in these dyads and, as a consequence, promotes intramolecular charge transfer. The absorption and fluorescence emission parameters of the prepared dyads in different solvents are given in Table 1. Changing the solvent polarity significantly impacts the emission properties. For instance, dyad **BDP-7** in toluene exhibits fluorescence emission with quantum yield of 0.661, associated with  $S_0 \rightarrow S_1$  transition. On the other hand, in polar acetonitrile, the fluorescence is strongly quenched leading to quantum yield of  $< 0.001$ . This behavior is observed for other dyads and is the signature of intramolecular charge transfer.

**Table 1.** Spectroscopic data and singlet oxygen quantum yield for compounds **BDP 1-7**.

Compound	Solvent	$\lambda_{\text{abs}}$ (nm)	$\lambda_{\text{em}}$ (nm) [a]	$\Phi_{\text{em}}$ <sup>[b]</sup>	$\Phi_{\Delta}$ <sup>[c]</sup>
<b>BDP-1</b>	toluene	506	523	0.381	0.041
	THF	503	519	0.238	0.009
	ACN	500	516	0.104	0.011
<b>BDP-2</b>	toluene	504	522	0.057	0.004
	THF	501	518	0.029	0.005
<b>BDP-3</b>	toluene	501	518	0.093	0.007
	THF	498	513	0.044	0.005
<b>BDP-4</b>	toluene	507	524	0.988	0.059
	THF	504	521	0.904	0.022
<b>BDP-5</b>	toluene	506	525	0.028	0.003
	THF	502	513	0.001	0.251
<b>BDP-6</b>	toluene	507	521	0.002	0.004
	THF	503	517	0.0006	0.158
<b>BDP-7</b>	toluene	507	522	0.661	0.193
	THF	504	519	0.316	0.110
	ACN	500	518	0.0003	0.363

[a] The fluorescence was excited at the vibrational shoulder of the BODIPY absorption. Excitation wavelengths: 470 - 490 nm for **BDP 1-7**. [b] Fluorescence quantum yields were measured using Rhodamine 6G ( $\Phi_{\text{em}} = 0.95$  in ethanol). [c] Quantum yields were measured using 1,9-dimethylantracene as a  $^1\text{O}_2$  trap and 2,6-diiodo-8-phenylBODIPY as a reference photosensitizer ( $\Phi_{\Delta} = 0.85$  in toluene).

Singlet oxygen sensitization by **BDP 1-7** was evaluated using chemical trapping method with 1,9-dimethylantracene (DMA) in toluene, THF and acetonitrile to ensure the consistency of the resulting dataset. Upon irradiation of air-saturated solutions containing each BODIPY compound at 514 nm, DMA selectively reacts with singlet oxygen forming corresponding endoperoxide. The BODIPY absorption shows no change during irradiation, while the DMA absorption decreases. The change of DMA absorbance with time is linear (Figure 5, inset), allowing to obtain  $\Phi_{\Delta}$  value from comparison with reference sensitizers (2,6-diiodo-8-phenylBODIPY). As shown in Table 1, the resulting  $\Phi_{\Delta}$  values vary depending on the solvent and the structure of electron-donating aryl group. The most efficient  $^1\text{O}_2$  sensitization was observed for **BDP-7** in acetonitrile ( $\Phi_{\Delta} = 0.363$ ). This correlates with efficient charge transfer process in this solvent. Dyads **BDP-5** and **BDP-6** showed  $\Phi_{\Delta}$  values of 0.25 and 0.16, respectively, in THF and low  $^1\text{O}_2$  sensitization ability in the remaining two solvents. Dyads **BDP 1-4** showed very modest  $\Phi_{\Delta}$  values in all solvents.

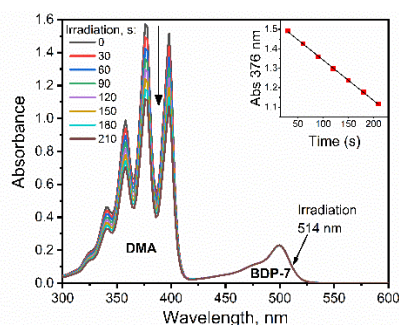


**Figure 5.** Photosensitized oxidation of 1,9-dimethylantracene in the presence of **BDP-7** in air saturated acetonitrile solution irradiated with 514 nm laser (12 mW cm<sup>-2</sup>). Inset: change of absorbance at 376 nm with time.

The resulting general dataset combining previously studied compounds and dyads **BDP 1-7** was divided into the training set (80% of the compounds) and the test set (20%) using random number generation. The activity of compounds, expressed as Log  $\Phi_{\Delta}$ , was used as a dependent variable during QSPR. Four newly synthesized compounds were put into the so-called external set. The toluene dataset was divided into the training set (35 compounds), the test set (9 compounds), and the external set (4 compounds). The acetonitrile dataset consisted of 33 compounds in the training set, 8 compounds in the test set, and 4 compounds in the external set. The tetrahydrofuran dataset was divided into the training set (30 compounds), the test set (7 compounds), and the external set (4 compounds).

### Molecular descriptors and model search

The QSPR approach employed here is based on the assumption that the efficiency of triplet state formation and singlet oxygen generation by the photosensitizer molecule depends on its structure and attempts to formulate mathematical relationship between calculated features of the structure (known as molecular descriptors) and its singlet oxygen quantum yield value.

The contribution of each descriptor to the model was estimated using equation (1):

$$\alpha(x_1) = \frac{R(x_1)}{R(x_1) + \dots + R(x_n)} \times 100 \quad (1)$$

where  $\alpha(x_1)$  is the relative contribution of the descriptor  $x_1$  to the model with several descriptors,  $R(x_n)$  is the correlation coefficient of the  $n$ th descriptor towards Log  $\Phi_{\Delta}$ .

Three different machine learning methods were used for models search: support vector regression (SVR), multiple linear regression (MLR), and random forest regression (RFR). QSPR models were selected on the basis of statistical parameters, such as  $R^2$  (determination coefficient of the training set) and  $R_{\text{test}}^2$  (predictive  $R^2$  for the test set of compounds). Predicting ability of the obtained models was evaluated for a test set of compounds,  $R_{\text{test}}^2$  parameter was used for model validation and comparison. A QSPR model is considered to be predictive if the following conditions are met:  $R^2 > 0.6$ ,  $q^2 > 0.6$ , and  $R_{\text{test}}^2 > 0.5$ .<sup>64</sup> Among the different machine learning methods applied, only MLR models showed satisfactory statistical parameters and thus was used in further analysis. Statistical parameters for toluene, acetonitrile, and tetrahydrofuran (THF) models are summarized in Table 2 and a detailed description of the statistical parameter calculation is given in the Experimental.

**Table 2.** Statistical parameters for multiple linear regression (MLR) models predicting the quantum yield of singlet oxygen generation by BODIPYs in toluene, acetonitrile, and tetrahydrofuran (THF).

Parameter	Toluene	Acetonitrile	THF
R	0.882	0.890	0.906
$R^2$	0.778	0.792	0.820
$R_{\text{adjusted}}^2$	0.739	0.744	0.773
SEE	0.282	0.319	0.325
RMSE	0.240	0.283	0.285
$q^2$	0.686	0.693	0.620
SDEP	0.306	0.344	0.414
$R_{\text{test}}^2$	0.800	0.823	0.879
$R_{\text{external}}^2$	0.635	0.722	0.584
RMS $\Phi_{\Delta}$ error	8.2	18.3	12.0
( $\Phi_{\Delta}$ in %)			

[a]  $R^2$ ,  $R_{\text{adjusted}}^2$ , SEE, and RMSE relate to the training set. SDEP and  $q^2$  relate to leave-one-out cross validation of the training set.  $R_{\text{test}}^2$  relates to the test set whereas  $R_{\text{external}}^2$  describes the external set of compounds. Root-mean-square (RMS)  $\Phi_{\Delta}$  error relates to the whole dataset, which combines the training set, the test set and the external set.

The resulting MLR equations have the following form:

$$y = c + a_1 \cdot x_1 + \dots + a_n \cdot x_n \quad (2)$$

where  $y$  is the dependent variable Log  $\Phi_{\Delta}$ ,  $c$  is a regression constant,  $a_1$  and  $a_n$  are regression coefficients,  $x_1$  and  $x_n$  are independent variables. The equation obtained for toluene model includes seven descriptors, whereas in the case of acetonitrile and THF the MLR models include six descriptors.

### Model 1 (toluene)

The model for predicting activity of photosensitizers in toluene was developed using data for the highest number of compounds – 48 BODIPYs from the general dataset. The MLR equation (9) for the model includes seven descriptors:

$\text{Log } \Phi_{\Delta} = 1.5424(\pm 0.2559) - 1.4403(\pm 0.3471) \text{DLS\_04} - 0.4718(\pm 0.1024) \text{Mor24m} + 0.536(\pm 0.0995) \text{ATSC6e} - 0.1479(\pm 0.0529) \text{F09[N-N]} - 4.1433(\pm 0.9008) \text{R6s+} + 0.8055(\pm 0.1948) \text{S1\_fosc} + 0.012(\pm 0.0031) \text{TPSA(Tot)}$   
 (Model 1)

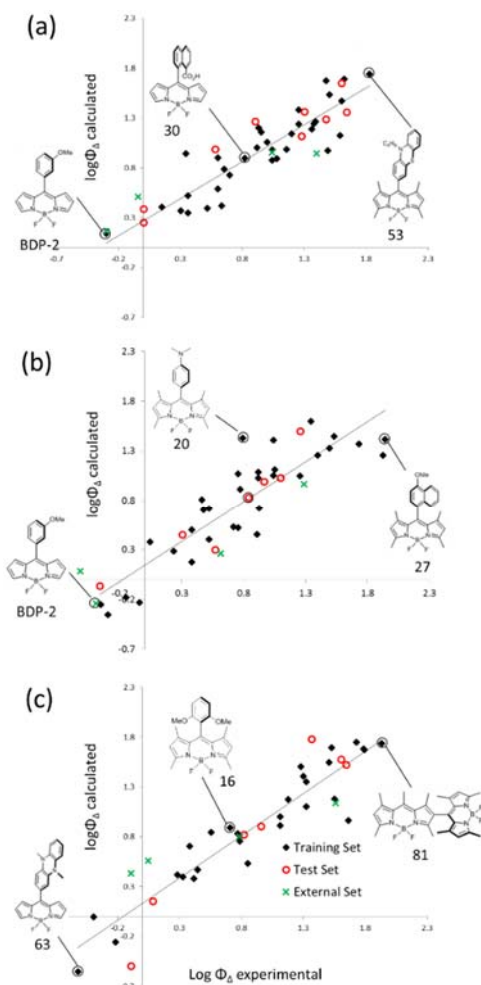


**Figure 6.** Experimental vs predicted  $\text{Log } \Phi_{\Delta}$  values for BODIPYs in toluene (a), acetonitrile (b), and THF (c). Three sample molecules from the general dataset are highlighted for each model.

Among the seven descriptors involved in Model 1, the two most influential are *R6s+* (relative contribution  $\alpha$  is equal to -29.9%) and *ATSC6e* ( $\alpha = 25.8\%$ ). *R6s+* is a GETAWAY descriptor, an R maximum autocorrelation of lag 6 (a path length, or topological distance between atoms) weighted by intrinsic state (I-state).<sup>65</sup> The I-state of the *i*-th atom is calculated by the formula:

$$I_i = \frac{(2/L_i)^2 \delta_i^y + 1}{\delta_i} \quad (3)$$

where  $L_i$  is the principal quantum number (2 for C, N, O, F, 3 for S),  $\delta_i^y$  is the number of valence electrons, and  $\delta_i$  is the number of sigma electrons of the *i*-th atom.

The I-state of an atom can be considered as the ratio of *n* and lone pair electrons to the count of the  $\sigma$  bonds. Thus, the I-state evaluates the possible partitioning of non-sigma electrons influence along the paths starting from the regarded atom; with less partitioning of the electron influence, the more available are the valence electrons for intermolecular interactions.<sup>66</sup> I-state is higher for electron withdrawing groups: for example, for  $-\text{CH}_2-$ ,  $-\text{NH}-$ , and  $-\text{O}-$  groups I-state is equal to 1.5 and 2.5, and 3.5, respectively. Hence, the descriptor captures the through-bond effects of the rest of the molecule on the electron density of atoms that can be involved in the charge transfer process.

*ATSC6e* descriptor is defined as the centered Broto-Moreau autocorrelation – lag 6 / weighted by the Sanderson electronegativities.<sup>67</sup> In general, the presence of electron withdrawing groups, such as F, Cl, and  $-\text{COOH}$  decrease *ATSC6e* values, whereas electron-donating alkyl and alkoxy groups increase the value of *ATSC6e*. In the obtained model, the descriptor is inversely correlated with  $\text{Log } \Phi_{\Delta}$ . Symmetrical BODIPY dimer **57** has the highest value of *ATSC6e* equal to 2.15, whereas BODIPY-perylene dyad **32** possesses the lowest value equal to 0.112.

*TPSA(Tot)* ( $\alpha = 13.3\%$ ) is a total topological polar surface area, corresponding to the polar surface area derived from polar contributions of N, O and S atoms and is related to the hydrogen bonding ability of the compound.<sup>68</sup> *TPSA(Tot)* is directly proportional to  $\text{Log } \Phi_{\Delta}$  of studied BODIPYs. Polar substituents increase the value of this descriptor whereas non-polar substituents decrease the value of *TPSA(Tot)*. Compound **53**, containing two phenothiazine groups, has the highest value of the descriptor equal to 75.4 whereas for BODIPY-anthracene dyad **30** *TPSA(Tot)* is equal to 6.48.

*DLS\_04* ( $\alpha = -12.2\%$ ) descriptor is related to drug-like score indices, similar to drug-like filters (7 rules) described by Chen et al.<sup>69</sup> This descriptor considers several characteristics: partition coefficient, the amount of hydrogen bond donors, number of hydrogen bond acceptors, molecular weight, ratio of the number of C(sp<sup>3</sup>) atoms over the total number of non-halogen heavy atoms, the ratio of H atoms to non-halogen heavy atoms, and the ratio of the molecular unsaturation over the total number of non-halogen heavy atoms. In the studied dataset the values of *DLS\_04* fall within the range of 0.4-0.8. Lower values of the *DLS\_04* index indicates that the compound is not good for drug-like purposes and is in accordance with the aim of our study, since efficient photosensitization of  $^1\text{O}_2$  leads to high cytotoxicity. *Mor24m* ( $\alpha = -10.3\%$ ) is a 3D-MoRSE-signal 24 / weighted by atomic masses,<sup>70</sup> which was found to be useful in predicting the toxicity of drugs.<sup>71</sup> 3D-MoRSE descriptors (Molecular Representation of Structures based on Electronic diffraction) are often regarded as “black box”, although the mathematical formula for the MoRSE descriptors is rather simple:

**Table 3.** Values of the descriptors used in Model 1 (toluene).

Compound	DLS_04	Mor24m	ATSC6e	F09[N-N]	R6s+	S1_fosc	TPSA(Tot)
<b>2</b>	0.8	0.362	0.509	0	0.254	0.5982	8.81
<b>3</b>	0.8	0.466	0.489	0	0.187	0.5741	8.81
<b>21</b>	0.8	0.429	0.493	0	0.131	0.3868	8.81
<b>25</b>	0.4	0.424	0.48	0	0.184	0.0147	46.1
<b>26</b> <sup>test [a]</sup>	0.6	0.507	0.788	0	0.142	0.1667	46.1
<b>27</b>	0.6	0.678	0.486	0	0.0646	0.3985	8.81
<b>28</b>	0.4	0.737	0.505	0	0.057	0.3966	8.81
<b>29</b> <sup>test [a]</sup>	0.4	0.568	0.552	0	0.0996	0.8794	8.81
<b>30</b>	0.6	-0.00895	0.909	0	0.0869	0.0265	6.48
<b>31</b>	0.5	-0.12	0.505	0	0.101	0.3872	8.81
<b>32</b>	0.4	0.171	0.112	0	0.0967	0.3404	8.81
<b>33</b>	0.5	0.158	0.516	0	0.0729	0.7044	8.81
<b>34</b>	0.6	-0.761	0.827	0	0.065	0.1024	35
<b>35</b>	0.6	0.0461	0.566	0	0.0532	0.0313	42
<b>36</b> <sup>test [a]</sup>	0.8	-0.581	0.661	0	0.0635	0.2843	19
<b>37</b>	0.5	0.531	0.297	1	0.186	0.117	26.9
<b>38</b>	0.7	-0.6	0.995	0	0.0625	0.4448	19
<b>39</b>	0.4	0.633	0.828	0	0.0702	0.0787	26.9
<b>40</b>	0.5	0.665	0.807	2	0.0695	0.0095	74.5
<b>41</b>	0.5	0.482	0.56	0	0.103	0.4147	26.9
<b>42</b>	0.7	0.473	0.709	1	0.132	0.6649	26.9
<b>43</b> <sup>test [a]</sup>	0.6	0.707	0.251	0	0.109	0.0835	18.7
<b>44</b>	0.8	0.546	0.597	0	0.0815	0.0011	18.7
<b>46</b>	0.7	1.06	1.15	0	0.0756	0.0843	27.5
<b>47</b>	0.6	0.89	0.118	0	0.0881	0.2915	13.7
<b>48</b>	0.8	0.878	0.518	0	0.0653	0.4534	13.7
<b>49</b>	0.4	0.868	0.597	1	0.112	0.701	13.7
<b>50</b>	0.4	0.734	0.608	1	0.122	0.8677	13.7
<b>51</b>	0.4	0.784	0.752	2	0.0695	0.2483	18.7
<b>52</b> <sup>test [a]</sup>	0.4	0.35	0.782	2	0.0641	0.2885	15.3
<b>53</b>	0.4	0.267	0.752	2	0.0845	0.0589	75.2
<b>55</b>	0.6	1.56	0.644	2	0.0836	0.9164	18.7
<b>56</b>	0.6	1.69	0.847	2	0.0342	0.8045	36.7
<b>57</b>	0.7	0.739	2.15	0	0.0826	0.3811	17.6
<b>58</b> <sup>test [a]</sup>	0.6	0.728	2.14	0	0.0603	0.3454	17.6
<b>59</b>	0.6	0.768	2.14	0	0.0609	0.4058	17.6
<b>60</b> <sup>test [a]</sup>	0.8	0.91	2.03	0	0.0644	0.4318	17.6
<b>61</b>	0.7	0.976	1.47	0	0.0796	0.698	17.6
<b>62</b> <sup>test [a]</sup>	0.7	0.972	1.64	0	0.09	0.1135	63.4
<b>63</b>	0.7	0.89	1.27	0	0.0911	0.0819	43.6
<b>64</b> <sup>test [a]</sup>	0.7	0.709	1.08	4	0.0699	0.0011	17.6
<b>BDP-1</b> <sup>ext [b]</sup>	0.6	0.346	0.356	0	0.199	0.3557	18
<b>BDP-2</b> <sup>ext [b]</sup>	0.6	0.576	0.308	0	0.244	0.276	18
<b>BDP-3</b>	0.6	0.55	0.253	0	0.245	0.2689	18
<b>BDP-4</b>	0.6	0.609	0.666	0	0.093	0.3084	27.3
<b>BDP-5</b> <sup>ext [b]</sup>	0.6	0.362	0.51	0	0.113	0.3352	27.3
<b>BDP-6</b>	0.6	0.483	0.727	0	0.0884	0.3005	36.5
<b>BDP-7</b> <sup>ext [b]</sup>	0.6	0.665	0.987	0	0.093	0.0017	36.5

[a] <sup>test</sup> designates compounds belonging to the test set. [b] <sup>ext</sup> relates to the molecules of the external set

$$Mor = \sum_{i=2}^N \sum_{j=1}^{i-1} A_i A_j \frac{s^{i+j} r_{ij}}{s r_{ij}} \quad (4)$$

where  $s$  is the scattering parameter,  $r_{ij}$  is the euclidean distance between  $i$ -th and  $j$ -th atoms,  $N$  is the total number of atoms,  $A_i$  and  $A_j$  are different atomic properties used as weights,<sup>70</sup> in the case of *Mor03s* and *Mor18s* – I-state.

The presence of *Mor24m* in the Model 1 reveals a significant dependence of  $\Phi_{\Delta}$  on the size of a molecule. The descriptor is inversely correlated with  $\log \Phi_{\Delta}$ . Compound **56** has the highest molecular weight among the studied compounds and its *Mor24m* value is the highest in the dataset. BODIPY-phenothiazine **34**, on the contrary, has the lowest value of *Mor24m* descriptor. Two descriptors have minor contributions to Model 1 ( $\alpha < 10\%$ ). *F09[N-N]* ( $\alpha = -5.3\%$ ) is a frequency of topological distance N-N equal to 9. The descriptor is inversely correlated with  $\log \Phi_{\Delta}$ . Phenylene-separated BODIPY dimer **64** possesses the highest value of *F09[N-N]* equal to 4, while for most compounds in the analyzed dataset it is equal to 0. *S1\_fosc* ( $\alpha = 3.3\%$ ) is an oscillator strength of the  $S_0 \rightarrow S_1$  transition. This parameter

correlates with quantum yield of the fluorescence from the lowest singlet excited state ( $\Phi_{\eta}$ ). As was shown in previous works, fluorescence from the  $S_1$  state competes with the charge transfer process in BODIPY dyads and molecules with high  $\Phi_{\eta}$  values show inefficient SOCT-ISC.<sup>38</sup>

### Model 2 (acetonitrile)

A total of 45 compounds from the general dataset are involved in this model. The MLR equation includes six descriptors:

$$\begin{aligned} \log \Phi_{\Delta} = & 3.2341(+/-0.4672) + 0.0872(+/-0.0456) \text{ Mor18s} + \\ & 0.0342(+/-0.0079) \text{ Mor03s} + 0.1974(+/-0.0648) \text{ F06[C-B]} - \\ & 0.0304(+/-0.0138) \text{ RDF065m} - 5.6375(+/-0.9105) \text{ MATS6s} - \\ & 76.4904(+/-12.1236) \text{ R8u+} \end{aligned} \quad (\text{Model 2})$$

Table 1 demonstrates that Model 2 performed as the most internally stable one ( $q^2 = 0.693$ ) and the best in predicting the properties for the external set of compounds ( $R_{\text{external}}^2 = 0.722$ ).

The predicted versus experimental values of  $\text{Log } \Phi_{\Delta}$  are presented in Figure 6b and in Table S4 (ESI).

*MATS6s* ( $\alpha = -28.9$ ) is a 2D Moran autocorrelation of lag 6 / weighted by the I-state as described by Todeschini and Consonni.<sup>72</sup> The correlation coefficient between *MATS6s* and  $\text{Log } \Phi_{\Delta}$  is high and equal to 0.569. The negative regression coefficient before *MATS6s* in Model 2 equation indicates that increased autocorrelation of six-membered structural graphs is unfavorable for high quantum yield  $\Phi_{\Delta}$  values. The importance of topological distance 6 is apparently due to the presence of aryl fragments (electron donors/acceptors) in most of the BODIPYs structures included in the dataset. The Moran coefficients usually fall within the [-1,+1] interval, whereas in the analyzed dataset most compounds possess *MATS6s* in the [-0.2,-0.1] interval. BODIPY **16** bearing dimethylaminophenyl group in the *meso* position has the highest value of *MATS6s* equal to 0.0676 whereas 1,3,5,7-tetramethylBODIPY **2** has the minimal *MATS6s* value in the acetonitrile dataset (-0.214) (Table 4). The reason

for such diverse values of the descriptor for these two compounds is the I-state values of certain atom types: for example, **16** contains tertiary amine N atom having rather low I-state value of 1.0882, whereas **2** is a relatively small molecule and contains four methyl groups: I-state equals to 2.0 which is high compared to other types of compounds.<sup>73</sup>

*R8u+* ( $\alpha = -22.2$ ) is an R maximal autocorrelation of lag 8 / unweighted. The descriptor is inversely correlated with  $\text{Log } \Phi_{\Delta}$ . *meso*-Pyridyl-substituted BODIPY **8** has the highest value of *R8u+* equal to 0.0392, whereas dihydrophenazine-separated BODIPY dimer **45** has the lowest value of the descriptor (0.013). Here, the importance of GETAWAY descriptors is demonstrated once again: Model 1 included *R6s+* descriptor with high relative contribution. Apparently, as in the case of *R6s+*, the maximum leverage influences the activity and *R8u+* value decreases with increasing the number of atoms.

**Table 4.** Values of the descriptors used in Model 2 (acetonitrile).

Compound	R8u+	MATS6s	F06[C-B]	Mor03s	RDF065m	Mor18s
<b>2</b> test [a]	0.0349	-0.214	0	-19.5	1.16	-2.72
<b>3</b>	0.0351	-0.142	2	-22.7	7.86	-5.08
<b>4</b> test [a]	0.0328	-0.124	2	-22.6	10.2	-3.28
<b>5</b>	0.0331	-0.121	2	-35.9	11.8	-5.11
<b>6</b> test [a]	0.0311	-0.0955	2	-28.4	13.3	-5.45
<b>7</b> test [a]	0.0304	0.0526	2	-29.9	15.7	-3.34
<b>8</b>	0.0392	-0.126	2	-20.9	6.67	-2.85
<b>9</b> test [a]	0.0362	-0.142	2	-22	7.88	-4.24
<b>10</b>	0.0243	-0.127	2	-21.7	10.5	-4.32
<b>11</b> test [a]	0.017	-0.147	2	-21.9	14.5	-5.36
<b>12</b> test [a]	0.0211	-0.109	2	-24.1	11.9	-4.74
<b>13</b>	0.0236	-0.13	2	-29.7	14.1	-4.55
<b>14</b>	0.0215	-0.197	2	-24.8	16.2	-4.91
<b>15</b>	0.019	-0.117	2	-18.3	11.3	-5.03
<b>16</b>	0.0185	0.0676	2	-15.8	10.1	-5.2
<b>17</b>	0.0179	-0.109	2	-29.1	9.85	-5.67
<b>18</b>	0.0161	0.0515	2	-25.2	9.11	-5.14
<b>19</b>	0.0182	-0.111	2	-30.8	9.35	-5.72
<b>20</b>	0.0163	0.0555	2	-27.7	8.6	-5.23
<b>21</b>	0.0239	-0.134	3	-23.9	11.6	-5.89
<b>22</b>	0.0177	-0.126	3	-25.3	14.5	-5.3
<b>23</b>	0.0283	-0.141	2	-26.5	12.8	-5.84
<b>24</b>	0.0195	0.0262	2	-23.2	11.9	-5.25
<b>25</b>	0.0235	-0.051	3	-28.1	9.81	-3.89
<b>26</b> test [a]	0.0249	-0.143	3	-26.2	10.8	-5.87
<b>27</b>	0.0158	-0.133	4	-27.1	11.1	-8.06
<b>28</b>	0.0146	-0.126	4	-27.8	22.3	-8.42
<b>29</b>	0.0166	-0.115	6	-32.1	21.8	-7.21
<b>30</b>	0.0163	-0.0437	4	-63	23.5	-5.81
<b>31</b>	0.0183	-0.131	3	-24.5	18.8	-3.55
<b>33</b>	0.0131	-0.124	3	-27.2	27.6	-8.05
<b>45</b>	0.013	0.0582	4	-52.7	25.9	-3.94
<b>47</b>	0.0159	0.0351	2	-33.3	9.88	-3.16
<b>48</b>	0.0131	-0.108	2	-28.2	13.5	-5.63
<b>54</b>	0.0145	-0.121	2	-28.5	21.5	-8.79
<b>61</b>	0.0173	-0.159	5	-51.1	13.3	-4.43
<b>63</b>	0.0157	-0.127	7	-49.4	22.8	-7.31
<b>64</b>	0.0156	-0.128	4	-43.9	29.4	-5.22
<b>BDP-1</b> ext [b]	0.0252	0.0179	2	-26.5	9.32	-1.7
<b>BDP-2</b> ext [b]	0.0292	0.0549	2	-27.1	7.78	-1.88
<b>BDP-3</b>	0.0294	0.0562	2	-25.2	7.5	-1.76
<b>BDP-4</b>	0.019	-0.0496	2	-28.3	12.1	-2.36
<b>BDP-5</b> ext [b]	0.0237	0.0429	2	-28.4	10.5	-2.29
<b>BDP-6</b>	0.0258	2.30E-04	2	-32.2	12.9	-2.04
<b>BDP-7</b> ext [b]	0.0236	-0.132	2	-29.8	13.5	-1.99

[a] test designates compounds belonging to the test set. [b] ext relates to the molecules of the external set

Model 2 involves two 3D-MorSE descriptors weighted by I-state: *Mor18s* ( $\alpha = 20.3$ ) and *Mor03s* ( $\alpha = 10.3$ ). Both descriptors are directly proportional to  $\text{Log } \Phi_{\Delta}$ . Dyad **54**, containing N-phenylcarbazol as an electron donating subunit, has the lowest

value of *Mor18s* (-8.79) whereas **BPD-1** possesses the highest value (-1.7) in the analyzed dataset. All compounds in the validation set (**BDP 1–7**) possess high values of *Mor18s*, which is apparently caused by the presence of methoxy groups in their



structures (-O- atom has a high I-state equal to 3.5). In comparison, dyad **54** is characterized by the presence of multiple aromatic rings with carbon atoms having I-state values of 1.5-2.0.

Regarding *Mor03s*, dyad **16** showed the highest value of -15.8, whereas the lowest value (-63) was obtained for BODIPY-anthracene dyad **30**, which is a relatively small molecule and contains four six-membered rings with carbon atoms having low I-state values. Although the structure of **16** is rather compact, it contains nitrogen atom and four methyl groups, each having high I-state of 2.

*F06[C-B]* ( $\alpha = 12.2\%$ ) is a frequency of topological distance C-B equal to 6. The descriptor is directly correlated with  $\text{Log } \Phi_{\Delta}$ . BODIPY dimer **63** possesses the highest value (7) of *F06[C-B]*, whereas compound **2** shows the lowest value equal to 0. It can be concluded that the descriptor allows to distinguish some cases when a more complicated molecular topology is favorable for efficient ISC.

*RDF065m* is a descriptor with minor relative contribution to Model 2 ( $\alpha = -6.3\%$ ). It is a radial distribution function at 6.5 Å / weighted by atomic masses. In simple terms, *RDF065m* can be regarded as a contribution of the atomic masses within the 6.5 Å radius of the molecule center. The lowest value is equal to 1.16 for compound **2**, having the lowest molecular weight in the dataset, whereas **64** is one of the largest molecules in the

analyzed dataset and possesses the highest value of *RDF065m* equal to 29.4.

### Model 3 (THF)

The total number of compounds involved in this model is 41. The MLR equation includes six descriptors:

$$\text{Log } \Phi_{\Delta} = 4.201(+/-1.4119) + 0.6225(+/-0.1328) \text{ ATSC7i} - 0.1358(+/-0.0243) \text{ F03[C-N]} - 0.0099(+/-0.0039) \text{ S2\_nm} + 0.8736(+/-0.2111) \text{ N-071} - 0.4099(+/-0.5512) \text{ LLS\_01} + 0.3846(+/-0.098) \text{ CATS3D\_07\_PL}$$

(Model 3)

This model possessed the best statistical parameters in terms of correlation coefficient of the training set ( $R = 0.906$ ) and predicting ability towards the test set ( $R_{\text{test}}^2 = 0.879$ ). The predicted versus experimental values of  $\text{Log } \Phi_{\Delta}$  are presented on Figure 6c and in Table S5 (ESI).

*N-071* ( $\alpha = 29.3$ ) has a major contribution to the model. The descriptor counts the number of tertiary nitrogen atoms attached to aromatic carbons. Only six such compounds (**15-20**) are present in the dataset. The lone pair of nitrogen contributes to the electron  $\pi$ -system and causes charge transfer process in these dyads, ultimately leading to SOCT-ISC.<sup>53</sup>

**Table 5.** Values of the descriptors used in Model 3 (THF).

Compound	ATSC7i	LLS_01	N-071	F03[C-N]	CATS3D_07_PL	S2_nm
<b>1</b>	0.0498	1	0	4	0	277.52
<b>2</b> test [a]	0.443	1	0	6	0	237.18
<b>3</b>	1.7	0.667	0	8	0	293.08
<b>4</b>	2	0.5	0	11	0	340.14
<b>5</b>	1.86	0.5	0	10	0	336.33
<b>6</b>	1.76	0.5	0	10	0	334.9
<b>7</b>	2.05	0.333	0	13	0	369.32
<b>8</b> test [a]	1.55	0.833	0	11	0	321.06
<b>9</b>	1.66	0.833	0	9	0	299.85
<b>10</b>	1.99	0.667	0	8	0	335.9
<b>11</b>	2.35	0.667	0	8	0	345
<b>12</b>	2.16	0.667	0	8	0	325.8
<b>13</b>	2.32	0.5	0	8	0	320.85
<b>14</b>	2.53	0.5	0	8	0	368.96
<b>15</b>	1.84	0.667	1	10	0	294.79
<b>16</b>	1.42	0.833	1	8	0	301.55
<b>17</b>	2.05	0.667	1	11	0	293.3
<b>18</b> test [a]	1.63	0.667	1	9	0	304.64
<b>19</b>	1.97	0.667	1	10	0	295.06
<b>20</b>	1.55	0.667	1	8	0	301.8
<b>21</b>	2.24	0.667	0	8	0	335.93
<b>22</b> test [a]	2.4	0.667	0	8	2	335.77
<b>23</b> test [a]	2.01	0.667	0	8	2	337.59
<b>24</b>	1.57	0.667	0	6	2	339.04
<b>25</b>	1.63	0.667	0	6	1	337.27
<b>26</b> test [a]	2.46	0.5	0	8	0	365.96
<b>27</b>	2.89	0.667	0	8	0	357.51
<b>31</b>	2.48	0.667	0	8	1	339.7
<b>33</b>	2.79	0.667	0	8	1	364.79
<b>43</b>	1.72	0.667	0	14	0	368.72
<b>44</b>	2.51	0.5	0	16	0	368.04
<b>45</b> test [a]	3.08	0.667	0	20	0	366.31
<b>46</b>	4.65	0.5	0	24	0	367.39
<b>61</b>	4.1	0.5	0	17	3	369.51
<b>BDP-1</b> ext [b]	1.21	1	0	6	0	320.26
<b>BDP-2</b> ext [b]	1.07	1	0	6	0	324.36
<b>BDP-3</b>	0.973	1	0	6	0	321.65
<b>BDP-4</b>	1.55	0.667	0	6	0	326.55
<b>BDP-5</b> ext [b]	1.37	0.667	0	6	0	319.95
<b>BDP-6</b>	1.53	0.5	0	6	0	324.17
<b>BDP-7</b> ext [b]	1.72	0.5	0	6	0	314.59

[a] test designates compounds belonging to the test set. [b] ext relates to the molecules of the external set

*CATS3D\_07\_PL* ( $\alpha = 24.0$ ) is a Chemically Advanced Template Search (CATS) 3D descriptor, namely the frequency of polar and non-polar groups separated by 7-8 Å. The descriptor is directly proportional to  $\text{Log } \Phi_{\Delta}$ . For most of the compounds in the dataset *CATS3D\_07\_PL* is equal to 0. Dimer **64** has the highest value of the descriptor equal to 3 (Table 5). Seemingly, in the case of **64** the descriptor evaluates the frequency of pairs between nitrogen atoms and methyl groups.

*F03[C-N]* ( $\alpha = -20.2$ ) is a frequency of C and N atoms at a topological distance of 3. The higher the value of the descriptor, the lower the quantum yield of  $^1\text{O}_2$  generation. Parent BODIPY **1** has the lowest value of *F03[C-N]* equal to 4, whereas dimer **46** possesses the highest value of 24.

*S2\_nm* ( $\alpha = -19.7$ ) is the energy of the second lowest singlet excited state in nanometers. The descriptor is inversely correlated with the quantum yield logarithm. Therefore, high  $S_2$  state energy (in eV) is favorable for high quantum yield. Compound **61** has the highest value of the descriptor equal to 370 nm, whereas **2** possesses the lowest value equal to 237 nm. BODIPYs are known to emit from the  $S_2$  state;<sup>74</sup> apparently this process can compete with intersystem crossing and triplet state formation which leads to lower  $\Phi_{\Delta}$  values.

Two descriptors have a minor contribution to Model 3: *LLS\_01* ( $\alpha = -4.3$ ) and *ATSC7i* ( $\alpha = 2.1$ ). *LLS\_01* is a lead-like score derived from the rules proposed by Congreve et al.<sup>75</sup> It takes into account the number of H-bond donors, number of H-bond acceptors, molecular weight, lipophilicity (logP), rotatable bond number, and polar surface area. Compounds with high *LLS\_01* (**BDP-1**, **BDP-2**, and **BDP-3**) show low photosensitization efficiency, in contrast to compounds with the low descriptor value like dyad **12**, which have  $\Phi_{\Delta}$  value of 0.46 in this solvent. *ATSC7i* is a centered Broto-Moreau autocorrelation of lag 7 / weighted by ionization potential. Dimer **46** has the highest *ATSC7i* equal to 4.65 whereas the *ATSC7i* of **1** is equal to 0.0498. The descriptor is directly proportional to  $\text{Log } \Phi_{\Delta}$ . Apparently, structures with high numbers of nitrogen, oxygen, and halogen atoms have high *ATSC7i* values due to higher ionization potential of such atoms.

## Conclusion

Herein we present for the first time a QSPR approach for predicting the efficiency of singlet oxygen generation by heavy-atom-free BODIPY in solvents of different polarity. Models developed using multiple linear regression (MLR) are quantitatively accurate and show good statistical parameters ( $R = 0.88\text{--}0.91$  and  $q^2 = 0.62\text{--}0.69$ ) for  $\Phi_{\Delta}$  prediction in all solvents, outperforming other machine learning methods, such as support vector regression (SVR) and random forest regression (RFR). The models were built using a combination of alvaDesc and quantum-chemical descriptors which can be obtained via simple calculations in a highly efficient manner. Broto-Moreau, GETAWAY, and MoRSE descriptors were found to be the most influential; in terms of atomic properties, intrinsic state, or l-state, of the atoms played a significant role for these descriptors and strongly correlates with the photosensitizing ability of BODIPYs. Interestingly, quantum-chemical descriptors such as frontier molecular orbital energies, HOMO-LUMO gap, energies of the lowest singlet and triplet excited states, as well as the singlet-

triplet energy gap ( $\Delta E_{ST}$ ) were found to have a low relative contribution to the models. These results demonstrate that challenging first-principle computations of triplets formation by charge recombination for predicting SOCT-ISC efficiency can to a certain extent be replaced by QSPR involving molecular descriptors which are computationally much faster to calculate.

The generated predictive models can serve as a simple and effective tool for guiding the design of SOCT-ISC photosensitizers with singlet oxygen quantum yield values optimized for desired range of polarity. Instead of randomly synthesizing donor-acceptor structures, QSPR models can be employed for *in silico* screening of large virtual libraries. Based on these predictions, a focused series of photosensitizers with tailored properties may be specifically selected and synthesized. As a proof of concept, in this work we succeeded to accurately predict  $^1\text{O}_2$  yields for several newly synthesized BODIPYs. Such approach is well-established in medicinal chemistry, where QSPR allow to achieve much higher success rate and speed up the search of lead compounds. However, in the field of photochemistry and photosensitizers design, QSPR methods are still largely unexplored. The results reported here, in conjunction with our previous studies, demonstrate that QSPR prediction of  $^1\text{O}_2$  generation is applicable to various types of organic dyes and that this methodology requires minimal resources and time for accurate prediction of the photosensitizers' activity.

## Experimental Section

### Synthesis of BODIPY

Compounds **BDP 1-3** were prepared according to published procedures.<sup>57,59</sup> The four newly reported BODIPY compounds (**BDP 4-7**) were prepared according to a previously described general procedure.<sup>Error! Bookmark not defined.</sup> All synthetic details and analytical data for new compounds are presented in the supplementary information.

### Computations

Conformational analysis of BODIPY molecules was performed using Spartan v. 16 modeling software from Wavefunction, Inc. (www.wavefun.com). Generation of low-energy conformers was performed using the MMFF force field.<sup>76</sup> Geometry optimization was done using Density Functional Theory. M06-2X functional<sup>77</sup> and 6-31G(d,p) basis set in Spartan v. 16 were used.

A total of 5305 molecular descriptors were calculated using alvaDesc v.1.0.22 program and online chemical modeling environment OCHEM.<sup>78</sup> The number of alvaDesc descriptors was reduced to 87 in the case of toluene, to 101 for acetonitrile, and to 107 for THF using Generic Algorithm v. 4.1 developed by the DTC lab and Kunal Roy.<sup>79</sup> Twenty three quantum-chemical descriptors, such as dipole moment, frontier molecular orbital energies, HOMO-LUMO gap, electronegativity, polarizability, and partial atomic charges were obtained at M06-2X/6-31G(d,p) level of theory for the gas phase. Energies of the two lowest singlet excited states ( $S_1$  and  $S_2$ ), energies of the two lowest triplet states ( $T_1$  and  $T_2$ ), as well as the singlet-triplet energy gap ( $\Delta E_{ST}$ ) and oscillator strengths were calculated using Time-Dependent Density Functional Theory (TD-DFT).

Machine learning (ML) was performed using scikit-learn library of Python programming language. SVR and RFR models search was performed in scikit-learn using grid-search method and 5-fold cross validation. During SVR model search three parameters were varied: C, epsilon, and kernel

(linear, polynomial, sigmoid or radial basis function). RFR search was performed by changing the values of two parameters: number of estimators (trees) and maximal depth. Other parameters were used by default. In the case of MLR, Genetic Algorithm v. 4.179 was used for the model search. Data pre-treatment included variance cut-off equal to 0.001 and inter-correlation cut-off equal to 0.9. Default values of all the parameters in Genetic Algorithm were used, except the equation length: the number of iterations/generations was equal to 100, the mutation probability was equal to 0.3, and the number of equations selected in each generation was equal to 30.

**Statistical parameters.**  $R_{adjusted}^2$  is an adjusted coefficient of determination:

$$R_{adjusted}^2 = 1 - \frac{(1-R^2)(n-1)}{n-p-1} \quad (5)$$

where  $n$  is the total number of compounds in the training set;  $p$  is the number of predictors used by the model. Standard error of estimate (SEE) was calculated using the following formula:

$$SEE = \sqrt{\frac{\sum(y_i - \hat{y}_i)^2}{n-p-1}} \quad (6)$$

where  $y_i$  and  $\hat{y}_i$  are the actual and predicted Log  $\Phi_{\Delta}$  value of the  $i$ -th molecule in the training set. To calculate root mean square error (RMSE) similar equation was used:

$$RMSE = \sqrt{\frac{\sum(y_i - \hat{y}_i)^2}{n}} \quad (7)$$

To calculate  $q^2$  (leave-one-out (LOO) cross-validation parameter) each molecule in the training set was excluded once and Log  $\Phi_{\Delta}$  of the excluded molecule was predicted by using the model developed for the remaining compounds.  $q^2$  describes the internal stability of a model and was calculated using the following formula:

$$q^2 = 1 - \frac{\sum(y_i - \hat{y}_{i,i})^2}{\sum(y_i - y_{mean})^2} \quad (8)$$

where  $y_i$  and  $\hat{y}_{i,i}$  are the actual and predicted Log  $\Phi_{\Delta}$  values of the  $i$ th molecule in the training set, respectively;  $y_{mean}$  is the average Log  $\Phi_{\Delta}$  of all compounds in the training set. To calculate standard deviation error of prediction (SDEP) during LOO cross-validation equation (9) was used:

$$SDEP = \sqrt{\frac{\sum(y_i - \hat{y}_{i,i})^2}{n}} \quad (9)$$

where  $y_i$  and  $\hat{y}_{i,i}$  are the actual and predicted Log  $\Phi_{\Delta}$  values of the  $i$ -th molecule, respectively.

The activity of each compound in the test set was predicted using the model developed with the training set.  $R_{test}^2$  reflects the predictive ability of the model and was calculated using the following equation:

$$R_{test}^2 = 1 - \frac{\sum(y_{act} - y_{pred})^2}{\sum(y_{act} - y_{mean})^2} \quad (10)$$

where  $y_{act}$  and  $y_{pred}$  are the actual and predicted activity of the  $i$ -th compound in the test set, respectively;  $y_{mean}$  is the average value of Log  $\Phi_{\Delta}$  in the training set. Both summations are over all compounds in the test set.  $R_{external}^2$  was calculated in a similar way as  $R_{test}^2$ , but for compounds included in the external set.

### Singlet oxygen quantum yield determination

The singlet oxygen quantum yield measurements were performed according to the literature.<sup>80</sup> Solutions of the  $^1O_2$  trap, 1,9-dimethylantracene (DMA), with an optical density of around 1.4 in air-saturated solvent (acetonitrile, toluene, and tetrahydrofuran respectively) were employed. Corresponding BODIPY was added to the cuvette, and its absorbance was adjusted to around 0.29 at the wavelength of irradiation. The solutions in the cuvette were irradiated with 514 nm laser light at a constant power density of 12 mW cm<sup>-2</sup>. The absorption spectra of the solutions were measured every 30 - 90 s. The slope of plots of absorbance of DMA at 376 nm vs. irradiation time for each photosensitizer was calculated.

Singlet oxygen quantum yields were calculated based on the equation:

$$\Phi_{\Delta} = \Phi_{\Delta}^{ref} \frac{k}{k_{ref}} \frac{I_{abs}^{ref}}{I_{abs}} \quad (11)$$

where  $\Phi_{\Delta}$  is the singlet oxygen quantum yield; the superscript ref stands for 2,6-diiodobodipy (0.85 in toluene)<sup>81</sup>;  $k$  is the slope of the curves of DMA absorption (376 nm) change vs. irradiation time;  $I_{abs}$  represents the absorption correction factor which is given by  $I = 1 - 10^{-OD}$  (OD is the optical density at 514 nm).

### X-ray Crystallography

Diffraction patterns were collected using CuK $\alpha$  and MoK $\alpha$  radiation (Bruker Duo, Bruker AXS package)<sup>82</sup>; solved with direct methods (ShelXT)<sup>83</sup> and refined with ShelXL<sup>84</sup> in the shelxle GUI.<sup>85</sup> Non-H atoms were refined with anisotropic thermal parameters; H-atoms were placed at geometrically ideal positions with riding thermal parameters. Full details are given in the supplementary information.

### Acknowledgements

This work was prepared with the support of funding from the European Union's Horizon 2020 research and innovation programme under the FET-OPEN grant agreement No.828779 and the Technical University of Munich – Institute for Advanced Study through a Hans Fischer Senior Fellowship. M.A.F. and A.S. acknowledge the TU Dublin Research Scholarship programme for support of this work.

**Keywords:** BODIPY • photosensitization • singlet oxygen • quantitative structure-property relationship • machine learning.

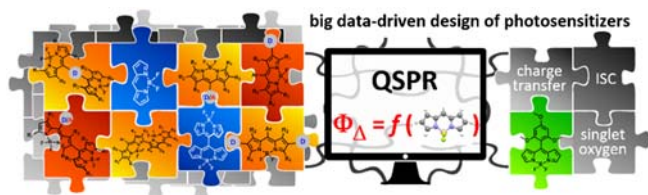
- [1] a) N. A. Romero, D.A. Nicewicz, *Chem. Rev.* **2016**, *116*, 10075-10166; b) M. H. Shaw, J. Twilton, D. W. C. MacMillan, *J. Org. Chem.* **2016**, *81*, 6898-6926; c) F. Glaser, O. S. Wenger, *Coord. Chem. Rev.* **2020**, *405*, 213129.
- [2] a) S. Kwiatkowski, B. Knap, D. Przystupski, J. Saczko, E. Kedzierska, K. Knap-Czop, J. Kotlinska, O. Michel, K. Kotowski, J. Kulbacka, *Biomed. Pharmacother.* **2018**, *106*, 1098-1107; b) S. Callaghan, M. O. Senge, *Photochem. Photobiol. Sci.* **2018**, *17*, 1490-1519.
- [3] a) F. N. Castellano, C. E. McCusker, *Dalton Trans.* **2015**, *44*, 17906-17910; b) J. Zhou, Q. Liu, W. Feng, Y. Sun, F. Li, *Chem. Rev.*, **2015**, *115*, 395-465; c) P. Bharmoria, H. Bildirir, K. Moth-Poulsen, *Chem. Soc. Rev.* **2020**, *49*, 6529-6554.
- [4] J. Zhao, K. Xu, W. Yang, Z. Wang, F. Zhong, *Chem. Soc. Rev.* **2015**, *44*, 8904-8939.
- [5] L. Huang, X. Cui, B. Therrien, J. Zhao, *Chem. Eur. J.* **2013**, *19*, 17472-17482.
- [6] a) J. Zhao, W. Wu, J. Sun, S. Guo, *Chem. Soc. Rev.* **2013**, *42*, 5323-5351; b) J. Zhao, K. Xu, W. Yang, Z. Wang, F. Zhong, *Chem. Soc. Rev.* **2015**, *44*, 8904-8939.
- [7] a) S. P. Pitre, C. D. McTiernan, H. Ismaili, J. C. Scaiano, *J. Am. Chem. Soc.* **2013**, *135*, 13286-13289; b) E. Speckmeier, T. G. Fischer, K. Zeitler, *J. Am. Chem. Soc.* **2018**, *140*, 15353-15365; c) N. J. Treat, H. Sprafke, J. W. Kramer, P. G. Clark, B. E. Barton, J. Read de Alaniz, B. P. Fors, C. J. Hawker, *J. Am. Chem. Soc.* **2014**, *136*, 16096-16101; d) S. M. Sartor, B. G. McCarthy, R. M. Pearson, G. M. Miyake, N. H. Damrauer, *J. Am. Chem. Soc.* **2018**, *140*, 4778-4781; e) D. A. Nicewicz, T. M. Nguyen, *ACS Catal.* **2014**, *4*, 355-360; f) C. Li, Y. Xu, W. Tu, G. Chen, R. Xu, *Green Chem.* **2017**, *19*, 882-899; g) J. Zhao, K. Xu, W. Yang, Z. Wang, F. Zhong, *Chem. Soc. Rev.* **2015**, *44*, 8904-8939.
- [8] J. Zhao, W. Wu, J. Sun, S. Guo, *Chem. Soc. Rev.* **2013**, *42*, 5323-5351.
- [9] M. Bröring, R. Krüger, S. Link, C. Kleeborg, S. Köhler, X. Xie, B. Ventura, L. Flamigni, *Chem. Eur. J.* **2008**, *14*, 2976-2983.

- [10] Y. Cakmak, S. Kolemen, S. Duman, Y. Dede, Y. Dolen, B. Kilic, Z. Kostereli, L. T. Yildirim, A.L. Dogan, D. Guc, E. U. Akkaya, *Angew. Chem. Int. Ed.* **2011**, *50*, 11937-11941; *Angew. Chem.* **2011**, *123*, 12143-12147.
- [11] a) K. Nagarajan, A. R. Mallia, K. Muraleedharan, M. Hariharan, *Chem Sci.* **2017**, *8*, 1776-1782; b) Z. Wang, L. Huang, Y. Yan, A. M. El-Zohry, A. Toffoletti, J. Zhao, A. Barbon, B. Dick, O. F. Mohammed, G. Han, *Angew. Chem. Int. Ed.* **2020**, *59*, 16114-16121; *Angew. Chem. Int. Ed.* **2020**, *132*, 16248-16255.
- [12] D. Sasikumar, A. T. John, J. Sunny, M. Hariharan, *Chem. Soc. Rev.* **2020**, *49*, 6122-6140.
- [13] a) Z. Wang, J. Zhao, *Org. Lett.* **2017**, *19*, 4492-4495; b) S. Kim, Y. Zhou, N. Tohna, H. Nakatsuji, M. Matsusaki, M. Fujitsuka, M. Miyata, T. Majima, *Chem. Eur. J.* **2018**, *24*, 636-645.
- [14] a) J. H. Golden, L. Estergreen, T. Porter, A. C. Tadde, D. M. R. Sylvinson, J. W. Facendola, C. P. Kubiak, S. E. Bradforth, M. E. Thompson, *ACS Appl. Energy Mater.* **2018**, *1*, 1083-1095; b) W. Huang, X. Zhang, B. Chen, H. Miao, C.O. Trindle, Y. Wang, Y. Luo, G. Zhang, *Chem. Commun.* **2019**, *55*, 67-70; c) J.-X. Wang, L.-Y. Niu, P.-Z. Chen, Y.-Z. Chen, Q.-Z. Yang, R. Boulatov, *Chem. Commun.* **2019**, *55*, 7017-7020.
- [15] a) C. Trinh, K. O. Kirlikovali, S. Das, M. E. Ener, H. B. Gray, P. I. Djurovich, S. Bradforth, M. E. Thompson, *J. Phys. Chem. C* **2014**, *118*, 21834-21845; b) S. Das, W. G. Thornbury, A. N. Bartynski, M. E. Thompson, S. E. Bradforth, *J. Phys. Chem. Lett.* **2018**, *9*, 3264-3270.
- [16] S. M. Sartor, B. G. McCarthy, R. M. Pearson, G. M. Miyake, N. H. Damrauer, *J. Am. Chem. Soc.* **2018**, *140*, 4778-4781.
- [17] Y. Tsuga, M. Katou, S. Kuwabara, T. Kanamori, S. Ogura, S. Okazaki, H. Ohtani, H. Yuasa, *Chem. Asian J.* **2019**, *14*, 2067-2071.
- [18] a) Y. Zhao, X. Li, Z. Wang, W. Yang, K. Chen, J. Zhao, G. G. Gurzadyan, *J. Phys. Chem. C* **2018**, *122*, 3756-3772; b) Y. Zhao, R. Duan, J. Zhao, C. Li, *Chem. Commun.* **2018**, *54*, 12329-12332.
- [19] J. W. Verhoeven, *J. Photochem. Photobiol. C* **2006**, *7*, 40-60.
- [20] a) Z. E. X. Dance, S. M. Mickley, T. M. Wilson, A. B. Ricks, A. M. Scott, M. A. Ratner, M. R. Wasielewski, *J. Phys. Chem. A* **2008**, *112*, 4194-4201; b) Z. E. X. Dance, Q. Mi, D. W. McCamant, M. J. Ahrens, M. A. Ratner, M. R. Wasielewski, *J. Phys. Chem. B* **2006**, *110*, 25163-25173; c) D. J. Gibbons, A. Farawar, P. Mazzella, S. Leroy-Lhez, R. M. Williams, *Photochem. Photobiol. Sci.* **2020**, *19*, 136-158.
- [21] G. Grampp, *Angew. Chem. Int. Ed.* **1993**, *32*, 691-693; *Angew. Chem.* **1993**, *105*, 724-726.
- [22] J. T. Buck, A. M. Boudreau, A. DeCarmin, R. W. Wilson, J. Hampsey, T. Mani, *Chem* **2019**, *5*, 138-155.
- [23] V.-N. Nguyen, Y. Yim, S. Kim, B. Ryu, K. M. K. Swamy, G. Kim, N. Kwon, C.-Y. Kim, S. Park, J. Yoon, *Angew. Chem. Int. Ed.* **2020**, *59*, 8957-8962; *Angew. Chem.* **2020**, *132*, 9042-9047.
- [24] Z. Mahmood, N. Rehmat, S. Ji, J. Zhao, S. Sun, M. Di Donato, M. Li, M. Teddei, Y. Huo, *Chem. Eur. J.* **2020**, *26*, 14912-14918.
- [25] a) J. Deckers, T. Cardeynaels, H. Penxten, A. Ethirajan, M. Ameloot, M. Kruk, B. Champagne, W. Maes, *Chem. Eur. J.* **2020**, *26*, 15212-15225; b) Y. Dong, A. Elmali, J. Zhao, B. Dick, A. Karatay, *ChemPhysChem* **2020**, *21*, 1388-1401.
- [26] I. J. Bruno, J. C. Cole, P. R. Edgington, M. Kessler, C. F. Macrae, P. McCabe, J. Pearson, R. Taylor, *Acta Cryst.* **2002**, *B58*, 389-397.
- [28] M. A. Filatov, S. Karuthedath, P. M. Polestshuk, S. Callaghan, K. J. Flanagan, T. Wiesner, F. Laquai, M.O. Senge, *ChemPhotoChem* **2018**, *2*, 606-615.
- [29] a) Z. Wang, J. Zhao, M. Di Donato, G. Mazzone, *Chem. Commun.* **2019**, *55*, 1510-1513; b) Z. Wang, M. Ivanov, Y. Gao, L. Bussotti, P. Foggi, H. Zhang, N. Russo, B. Dick, J. Zhao, M. Di Donato, G. Mazzone, L. Luo, M. Fedin, *Chem. Eur. J.* **2020**, *26*, 1091-1102.
- [30] K. Chen, W. Yang, Z. Wang, A. Iagatti, L. Bussotti, P. Foggi, W. Ji, J. Zhao, M. Di Donato, *J. Phys. Chem. A* **2017**, *121*, 7550-7564.
- [31] Y. Hou, I. Kurganskii, A. Elmali, H. Zhang, Y. Gao, L. Lv, J. Zhao, A. Karatay, L. Luo, M. Fedin, *J. Chem. Phys.* **2020**, *152*, 114701.
- [32] Y. Dong, A. A. Sukhanov, J. Zhao, A. Elmali, X. Li, B. Dick, A. Karatay, V. K. Voronkova, *J. Phys. Chem. C* **2019**, *123*, 22793-22811.
- [33] M. A. Filatov, S. Karuthedath, P. M. Polestshuk, H. Savoie, K. J. Flanagan, C. Sy, E. Sitte, M. Teitlichko, F. Laquai, R. W. Boyle, M. O. Senge, *J. Am. Chem. Soc.* **2017**, *139*, 6282-6285.
- [34] a) S. Callaghan, M. A. Filatov, H. Savoie, R. W. Boyle, M. O. Senge, *Photochem. Photobiol. Sci.* **2019**, *18*, 495-504; b) S. Callaghan, B. E. Vindstad, K. J. Flanagan, T. B. Melø, M. Lindgren, K. Grenstad, O. A. Gederaas, M. O. Senge, *ChemPhotoChem* **2021**, *5*, 131-141.
- [35] N. Kiseleva, M. A. Filatov, M. Oldenburg, D. Busko, M. Jakoby, I. A. Howard, B. S. Richards, M. O. Senge, S. M. Borisov, A. Turshatov, *Chem. Commun.* **2018**, *54*, 1607-1610.
- [36] N. Kiseleva, D. Busko, B. S. Richards, M. A. Filatov, A. Turshatov, *J. Phys. Chem. Lett.* **2020**, *11*, 6560-6566.
- [37] A. B. Nepomnyashchii, A. J. Bards, *Acc. Chem. Res.* **2012**, *45*, 1844-1853.
- [38] M. A. Filatov, *Org. Biomol. Chem.* **2020**, *18*, 10-27.
- [39] X.-F. Zhang, X. Yang, *J. Phys. Chem. B* **2013**, *117*, 9050-9055.
- [40] N. Epelde-Elezcano, E. Palao, H. Manzano, A. Prieto-CastaCeda, A. R. Agarrabeitia, A. Tabero, A. Villanueva, S. de la Moya, C. Ljpez-Arbeloa, V. Martinez-Martinez, M. J. Ortiz, *Chem. Eur. J.* **2017**, *23*, 4837-4848.
- [41] J. F. Lovell, T. W. B. Liu, J. Chen, G. Zheng, *Chem. Rev.* **2010**, *110*, 2839-2857.
- [42] a) C. M. Isborn, B. D. Mar, B. F. E. Curchod, I. Tavernelli, T. J. Martínez, *J. Phys. Chem. B* **2013**, *117*, 12189-12201; b) S. Bhandari, B. D. Dunietz, *J. Chem. Theory Comput.* **2019**, *15*, 4305-4311.
- [43] J. Shi, F. Luan, H. Zhang, M. Liu, Q. Guo, Z. Hu, B. Fan, *QSAR Comb. Sci.* **2006**, *25*, 147-155.
- [44] A. Schüller, G. B. Goh, H. Kim, J.-S. Lee, Y.-T. Chang, *Mol. Inform.* **2010**, *29*, 717-729.
- [45] E. Caruso, M. Gariboldi, A. Sangion, P. Gramatica, S. Banfi, *J. Photochem. Photobiol. B* **2017**, *167*, 269-281.
- [46] J. Zhao, Y. Zhou, C. Li, Q. Xie, J. Chen, G. Chen, W. J. G. M. Peijnenburg, Y. N. Zhang, J. Qu, *Sci. Total Environ.* **2020**, *712*, 136450.
- [47] A. A. Buglak, T. A. Telegina, M. S. Kritsky, *Photochem. Photobiol. Sci.* **2016**, *15*, 801-811.
- [48] A. A. Buglak, A. I. Kononov, *New J. Chem.*, **2018** *42*, 14424-14432.
- [49] A. A. Buglak, M. A. Filatov, M. A. Hussain, M. Sugimoto, *J. Photochem. Photobiol. A* **2020**, *403*, 112833.
- [50] I. S. Turan, G. Gunaydin, S. Ayan, E. U. Akkaya, *Nat. Commun.* **2018**, *9*, 805.
- [51] T. Yogo, Y. Urano, A. Mizushima, H. Sunahara, T. Inoue, K. Hirose, M. Iino, K. Kikuchi, T. Nagano, *Proc. Nat. Acad. Sci. U.S.A.* **2008**, *105*, 28-32.
- [52] C. Schweitzer, R. Schmidt, *Chem. Rev.* **2003**, *103*, 1685-1758.
- [53] a) H. Liang, S. Sun, M. Zafar, Z. Yuan, Y. Dong, S. Ji, Y. Huo, M.-D. Li, J. Zhao, *Dyes Pigment.* **2020**, *173*, 108003; b) Y. Hou, J. Liu, N. Zhang, J. Zhao, *J. Phys. Chem. A* **2020**, *124*, 9360-9374.
- [54] W. Hu, Y. Lin, X.-F. Zhang, M. Feng, S. Zhao, J. Zhang, *Dyes Pigment.* **2019**, *164*, 139-147.
- [55] a) A. E. O'Connor, W. M. Gallagher, A. T. Byrne, *Photochem. Photobiol.* **2009**, *85*, 1053-1074; b) T. M. Baran, *Lasers Surg. Med.* **2018**, *50*, 476-482.
- [56] a) W.-S. Cho, H.-J. Kim, B. J. Littler, M. A. Miller, C.-H. Lee, J. S. Lindsey, *J. Org. Chem.* **1999**, *64*, 7890-7901; b) C.-H. Lee, J. S. Lindsey, *Tetrahedron* **1994**, *50*, 11427-11440.
- [57] a) M. Elisa Milanesio, F. S. Morán, E. Ines Yslas, M. Gabriela Alvarez, V. Rivarola, E. N. Durantini, *Bioorg. Med. Chem.* **2001**, *9*, 1943-1949; b) R. R. Kavali, B. Chul Lee, B. Seok Moon, S. Dae Yang, K. Soo Chun, C. Woon Choi, C.-H. Lee, D. Yoon Chi, *J. Labelled Compd. Rad.* **2005**, *48*, 749-758; c) B. J. Littler, M. A. Miller, C.-H. Hung, R. W. Wagner, D. F. O'Shea, P. D. Boyle, J. S. Lindsey, *J. Org. Chem.* **1999**, *64*, 1391-1396; d) A. Ogawa, K. Oohora, T. Hayashi, *Inorg. Chem.* **2018**, *57*, 14644-14652; e) A. J. Pistner, D. A. Lutterman, M. J. Ghidui, Y.-Z. Ma, J. Rosenthal, *J. Am. Chem. Soc.* **2013**, *135*, 6601-6607; f) W. Senapak, R. Saeeng, J. Jaratjaroonphong, T. Kasemsuk, U. Sirion, *Org. Biomol. Chem.* **2016**, *14*, 1302-1310.
- [58] a) G. Ulrich, R. Ziessel, A. Harriman, *Angew. Chem. Int. Ed.* **2008**, *47*, 1184-1201; *Angew. Chem.* **2008**, *120*, 1202-1219; b) R. W. Wagner, J. S. Lindsey, *Pure Appl. Chem.* **1996**, *68*, 1373-1380.

- 
- [59] a) F. Frank, L. M. Alice, P. Mauker, A. A. Alsimaree, P. G. Waddell, M. R. Probert, T. J. Penfold, J. G. Knight, M. J. Hall, *Tetrahedron* **2020**, *76*, 131113; b) T.-I. Kim, S. B. Maity, J. Bouffard, Y. Kim, *Anal. Chem.* **2016**, *88*, 9259-9263; c) P. E. Kesavan, R. N. Behera, S. Mori, I. Gupta, *J. Fluoresc.* **2017**, *27*, 2131-2144.
- [60] R. I. Roacho, A. J. Metta-Magaña, E. Peña-Cabrera, K. H. Pannell, *J. Phys. Org. Chem.* **2013**, *26*, 345-351.
- [61] T. V. Goud, A. Tutar, J.-F. Biellmann, *Tetrahedron* **2006**, *62*, 5084-5091.
- [62] M. R. Rao, R. Bolligarla, R. J. Butcher, M. Ravikanth, *Inorg. Chem.* **2010**, *49*, 10606-10616.
- [63] P. Luo, E. C. Feinberg, G. Guirado, S. Farid, J. P. Dinnocenzo, *J. Org. Chem.* **2014**, *79*, 9297-9304.
- [64] A. Golbraikh, A. Tropsha, *J. Mol. Graph. Model.* **2002**, *20*, 269-276.
- [65] L. H. Hall, B. Mohny, L. B. Kier, *J. Chem. Inf. Comput. Sci.* **1991**, *31*, 76-81.
- [66] V. Consonni, R. Todeschini, M. Pavan, *J. Chem. Inf. Comput. Sci.* **2002**, *42*, 682-692.
- [67] L. B. Kier, L. H. Hall. *Molecular Connectivity in Chemistry and Drug Research*. Academic Press, New York, 1976.
- [68] P. Ertl, B. Rohde, P. Selzer, *J. Med. Chem.* **2000**, *43*, 3714-3717.
- [69] G. Chen, S. Zheng, X. Luo, J. Shen, W. Zhu, H. Liu, C. Gui, J. Zhang, M. Zheng, C. Puah, K. Chen, H. Jiang, *J. Comb. Chem.* **2005**, *7*, 398-406.
- [70] O. Devinyak, D. Havrylyuk, R. Lesyk, *J. Mol. Graph. Model.* **2014**, *54*, 194-203.
- [71] M. Doga Ertürk, M. Türker Sacan, M. Novic, N. Minovski, *J. Mol. Graph. Model.* **2012**, *38*, 90-100.
- [72] R. Todeschini, V. Consonni, *Handbook of Molecular Descriptors*, Wiley-VCH: Weinheim, Germany, 2000
- [73] L. T. Qin, S. S. Liu, H. L. Liu, *Mol. Divers.* **2010**, *14*, 67-80.
- [74] D. W. Cho, M. Fujitsuka, J. H. Ryu, M. H. Lee, H. K. Kim, T. Majima, C. Im, *Chem. Commun.*, **2012** *48*, 3424-3426.
- [75] M. Congreve, R. Carr, C. Murray, H. Jhoti, *Drug Discov. Today* **2003**, *8*, 876-877.
- [76] T. A. Halgren, *J. Comput. Chem.* **1996**, *17*, 490-519.
- [77] a) Y. Zhao, D. G. Truhlar, *Theor. Chem. Acc.* **2008**, *120*, 215-241; b) Y. Zhao, D. G. Truhlar, *Acc Chem. Res.* **2008**, *41*, 157-167.
- [78] I. Sushko, S. Novotarskyi, R. Körner, A. K. Pandey, M. Rupp, W. Teetz, S. Brandmaier, A. Abdelaziz, V. V. Prokopenko, V. Y. Tanchuk, R. Todeschini, A. Varnek, G. Marcou, P. Ertl, V. Potemkin, M. Grishina, J. Gasteiger, C. Schwab, I. I. Baskin, V. A. Palyulin, E. V. Radchenko, W. J. Welsh, V. Kholodovych, D. Chekmarev, A. Cherkasov, J. Aires-de-Sousa, Q.-Y. Zhang, A. Bender, F. Nigsch, L. Patiny, A. Williams, V. Tkachenko, I. V. Tetko, *J. Comput. Aided Mol. Des.* **2011**, *25*, 533-554.
- [79] K. Roy, *J. Indian Chem. Soc.* **2018**, *95*, 1497-1502.
- [80] L. Gou, C. N. Coretsopoulos, A. B. Scranton, *J. Polym. Sci. Part A Polym. Chem.* **2004**, *42*, 1285-1292.
- [81] Y. Zhao, R. Duan, J. Zhao, C. Li, *Chem. Commun.* **2018**, *54*, 12329-12332.
- [82] APEX 3 and SAINT. Bruker AXS Inc., Madison, Wisconsin, USA, **2015**.
- [83] G. M. Sheldrick, *Acta Cryst.* **2008**, *A64*, 112-122.
- [84] G. M. Sheldrick, *Acta Cryst.* **2015**, *C71*, 3-8.
- [85] C. B. Hübschle, G. M. Sheldrick, B. Dittrich, *J. Appl. Cryst.* **2011**, *44*, 1281-1284.

---

## Entry for the Table of Contents



Data on singlet oxygen generation for a library of heavy-atom-free BODIPYs undergoing spin-orbit charge transfer intersystem crossing (SOCT-ISC) were used to build quantitative structure– property relationship (QSPR) predictive models. These models estimate quantum yields of singlet oxygen ( $^1\text{O}_2$ ) generation for a given photosensitizer structure in non-polar, moderately polar and highly polar solvent. This allows for virtual screening of environment-activatable BODIPY photosensitizers and hence speeding up the development of new lead compounds for photomedicine.

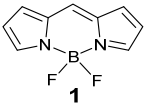
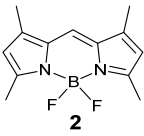
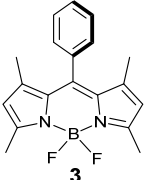
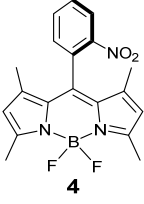
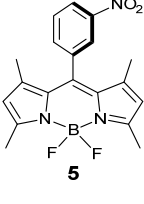
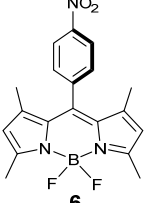

# Supplementary Information

## Contents

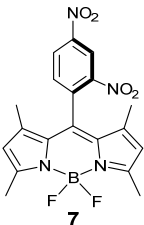
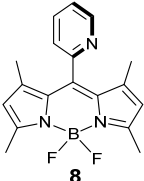
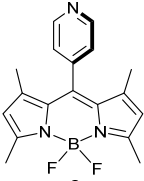
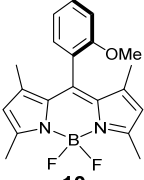
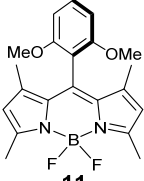
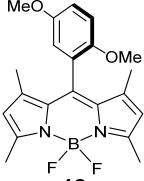
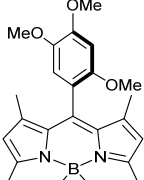
<b>1. BODIPY dataset</b> .....	S2
<b>2. Synthetic Procedures and Characterization</b> .....	S12
<b>2.1 Materials and Instruments</b> .....	S12
<b>2.2 Chemical Synthesis of BDP 1-7</b> .....	S12
<b>2.3 NMR and HRMS Data</b> .....	S14
<b>2.4 Crystallographic Data</b> .....	S24
<b>2.5 Optical Spectra</b> .....	S25
<b>3. Computational methods and results</b> .....	S28
<b>4. Singlet oxygen generation quantum yields measurements</b> .....	S31
<b>5. Supplemental Crystal Structure Images</b> .....	S40
<b>6. References</b> .....	S43

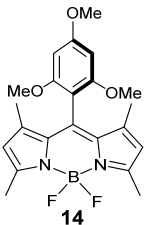
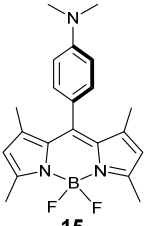
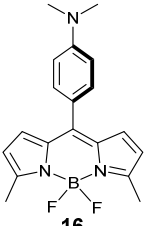
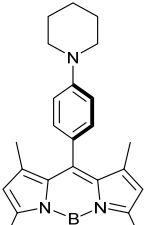
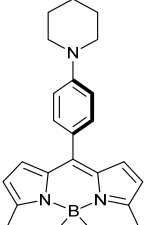
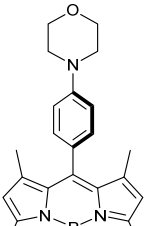
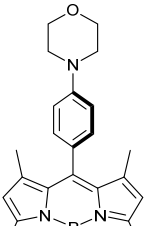
## 1. BODIPY dataset

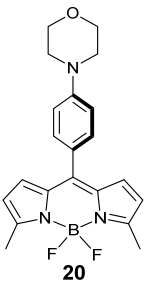
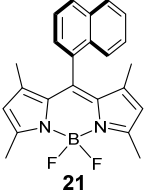
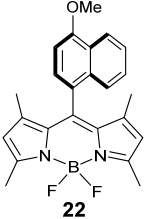
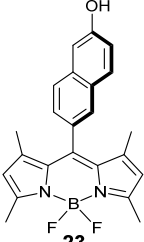
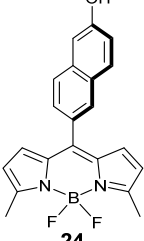
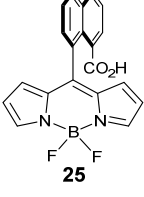
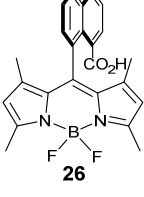
**Table S1.** The structures and singlet oxygen quantum yield values ( $\Phi_{\Delta}$ ) of heavy-atom-free BODIPYs dyes in different solvents, as searched from chemical databases.  $\Phi_{\Delta}$  values used in Models 1-3 are highlighted.

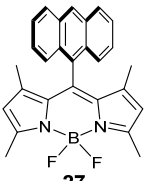
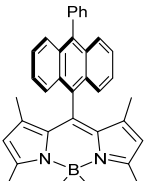
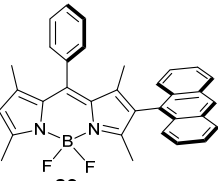
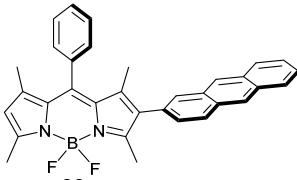
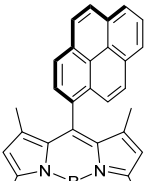
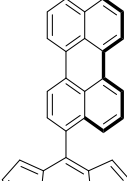
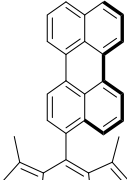
Structure	Solvent	$\Phi_{\Delta}$	Reference
 1	hexane	0.066	1
	toluene	0.12	1
	THF	0.071	1
	MeOH	0.083	1
 2	hexane	0.03	2
	toluene	0.061	2
	CCl <sub>4</sub>	0.100	2
	CH <sub>2</sub> Cl <sub>2</sub>	0.062	2
	THF	0.091	2
	EtOH	0.058	2
 3	hexane	0.038	3
	toluene	0.023	4
	EtOAc	0.052	3
	THF	0.13	4
	pinacolone	0.11	3
	acetone	0.050	3
	EtOH	0.030	4
	MeOH	0.031	3
	CH <sub>3</sub> CN	0.017	4
 4	hexane	0.018	3
	EtOAc	0.027	3
	THF	0.026	3
	pinacolone	0.079	3
	acetone	0.051	3
	MeOH	0.0083	3
 5	hexane	0.01	3
	EtOAc	0.031	3
	THF	0.028	3
	pinacolone	0.07	3
	acetone	0.029	3
	MeOH	0.0062	3
	CH <sub>3</sub> CN	0.0044	3
 6	hexane	0.0067	3
	EtOAc	0.021	3
	THF	0.019	3
	pinacolone	0.047	3
	acetone	0.0093	3
	MeOH	0.0036	3
	hexane	0.021	3
	EtOAc	0.026	3
	THF	0.026	3
	pinacolone	0.073	3
	acetone	0.012	3

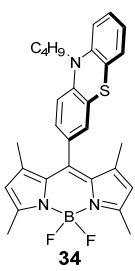
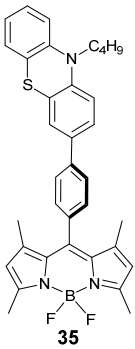
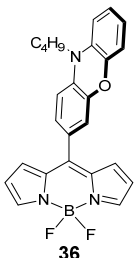
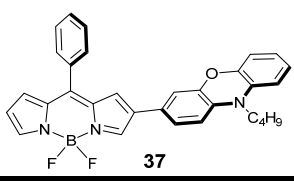
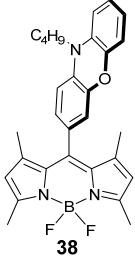
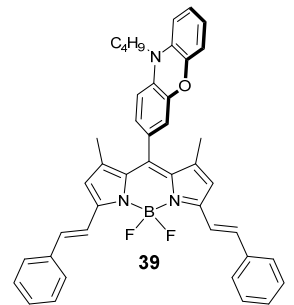


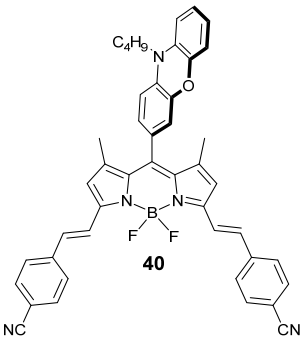
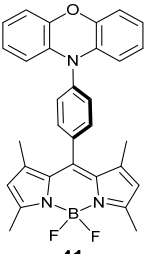
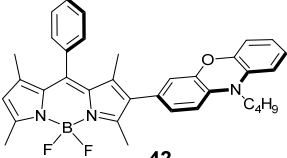
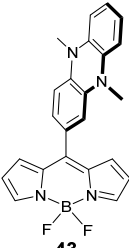
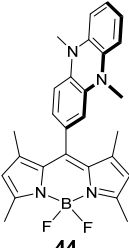
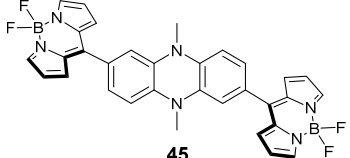
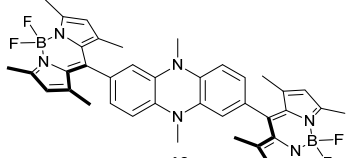
 7	MeOH	0.0055	3
	CH <sub>3</sub> CN	0.0049	3
 8	hexane	0.0052	3
	EtOAc	0.0039	3
	THF	0.012	3
	pinacolone	0.012	3
	acetone	0.012	3
	MeOH	0.013	3
	CH <sub>3</sub> CN	0.024	3
 9	hexane	0.0091	3
	EtOAc	0.032	3
	THF	0.024	3
	pinacolone	0.020	3
	acetone	0.031	3
	MeOH	0.012	3
	CH <sub>3</sub> CN	0.037	3
 10	hexane	0.029	5
	EtOAc	0.057	5
	THF	0.061	5
	pinacolone	0.078	5
	acetone	0.17	5
	MeOH	0.021	5
	CH <sub>3</sub> CN	0.18	5
 11	hexane	0.040	5
	EtOAc	0.073	5
	THF	0.051	5
	pinacolone	0.081	5
	acetone	0.082	5
	MeOH	0.036	5
	CH <sub>3</sub> CN	0.18	5
 12	hexane	0.026	6
	EtOAc	0.178	6
	THF	0.462	6
	pinacolone	0.680	6
	acetone	0.250	6
	MeOH	0.023	6
	CH <sub>3</sub> CN	0.125	6
 13	hexane	0.114	6
	EtOAc	0.291	6
	THF	0.357	6
	pinacolone	0.392	6
	acetone	0.068	6
	MeOH	0.004	6
	CH <sub>3</sub> CN	0.033	6
	hexane	0.024	5
	EtOAc	0.063	5

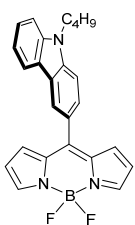
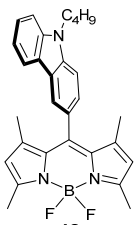
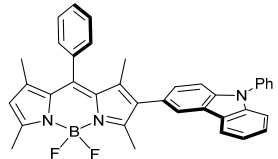
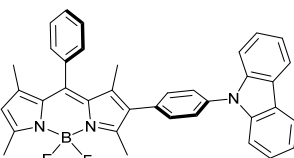
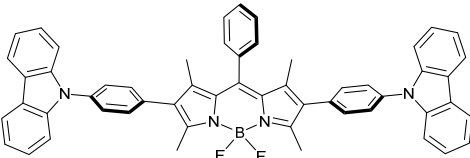
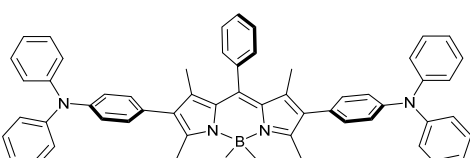
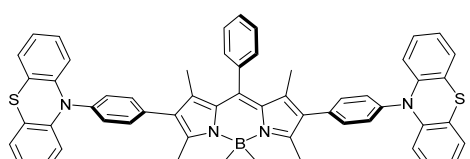
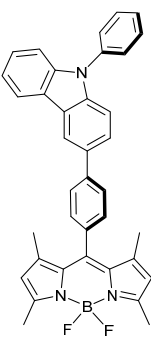
 <p><b>14</b></p>	THF	0.059	5
	pinacolone	0.16	5
	acetone	0.11	5
	MeOH	0.074	5
	CH <sub>3</sub> CN	0.31	5
 <p><b>15</b></p>	hexane	0.102	7
	EtOAc	0.412	7
	THF	0.623	7
	pinacolone	0.490	7
	acetone	0.114	7
	MeOH	0.073	7
	CH <sub>3</sub> CN	0.062	7
 <p><b>16</b></p>	hexane	0.23	7
	EtOAc	0.171	7
	THF	0.321	7
	pinacolone	0.439	7
	acetone	0.087	7
	MeOH	0.019	7
	CH <sub>3</sub> CN	0.052	7
 <p><b>17</b></p>	hexane	0.058	7
	EtOAc	0.511	7
	THF	0.612	7
	pinacolone	0.644	7
	acetone	0.145	7
	MeOH	0.037	7
	CH <sub>3</sub> CN	0.083	7
 <p><b>18</b></p>	hexane	0.258	7
	EtOAc	0.220	7
	THF	0.401	7
	pinacolone	0.457	7
	acetone	0.099	7
	MeOH	0.046	7
	CH <sub>3</sub> CN	0.057	7
 <p><b>19</b></p>	hexane	0.120	7
	EtOAc	0.676	7
	THF	0.535	7
	pinacolone	0.588	7
	acetone	0.192	7
	MeOH	0.038	7
	CH <sub>3</sub> CN	0.083	7
 <p><b>19</b></p>	hexane	0.225	7
	EtOAc	0.290	7
	THF	0.338	7
	pinacolone	0.281	7
	acetone	0.100	7
	MeOH	0.008	7

 <p style="text-align: center;"><b>20</b></p>	CH <sub>3</sub> CN	0.033	7
 <p style="text-align: center;"><b>21</b></p>	hexane	0.05	4
	toluene	0.043	4
	THF	0.13	4
	EtOH	0.041	4
	CH <sub>3</sub> CN	0.057	4
 <p style="text-align: center;"><b>22</b></p>	hexane	0.011	6
	EtOAc	0.165	6
	THF	0.232	6
	pinacolone	0.460	6
	acetone	0.471	6
	MeOH	0.274	6
	CH <sub>3</sub> CN	0.872	6
 <p style="text-align: center;"><b>23</b></p>	hexane	0.047	6
	EtOAc	0.104	6
	THF	0.442	6
	pinacolone	0.382	6
	acetone	0.111	6
	MeOH	0.131	6
	CH <sub>3</sub> CN	0.081	6
 <p style="text-align: center;"><b>24</b></p>	hexane	0.116	6
	EtOAc	0.106	6
	THF	0.19	6
	pinacolone	0.317	6
	acetone	0.070	6
	MeOH	0.046	6
	CH <sub>3</sub> CN	0.011	6
 <p style="text-align: center;"><b>25</b></p>	hexane	n.d.	2
	toluene	0.066	2
	CCl <sub>4</sub>	0.15	2
	CH <sub>2</sub> Cl <sub>2</sub>	0.20	2
	THF	0.15	2
	EtOH	0.30	2
	CH <sub>3</sub> CN	0.084	2
 <p style="text-align: center;"><b>26</b></p>	hexane	0.066	2
	toluene	0.038	2
	CCl <sub>4</sub>	0.061	2
	CH <sub>2</sub> Cl <sub>2</sub>	0.068	2
	THF	0.066	2
	EtOH	0.18	2
	CH <sub>3</sub> CN	0.092	2
	hexane	0.01	8

 <p style="text-align: center;"><b>27</b></p>	toluene	0.045	4
	THF	0.21	4
	EtOH	0.53	8
	CH <sub>3</sub> CN	0.22	4
 <p style="text-align: center;"><b>28</b></p>	hexane	0.04	8
	toluene	0.10	9
	EtOH	0.59	8
	CH <sub>3</sub> CN	0.84	9
 <p style="text-align: center;"><b>29</b></p>	toluene	0.20	9
	CH <sub>2</sub> Cl <sub>2</sub>	0.24	9
	CH <sub>3</sub> CN	0.11	9
 <p style="text-align: center;"><b>30</b></p>	toluene	0.11	9
	CH <sub>2</sub> Cl <sub>2</sub>	0.13	9
	CH <sub>3</sub> CN	0.005	9
 <p style="text-align: center;"><b>31</b></p>	hexane	0.01	10
	toluene	0.086	4
	THF	0.20	4
	EtOH	0.34	10
	CH <sub>3</sub> CN	0.34	4
 <p style="text-align: center;"><b>32</b></p>	hexane	0.1	11
	toluene	0.31	12
 <p style="text-align: center;"><b>33</b></p>	toluene	0.18	11
	THF	0.21	11
	CH <sub>2</sub> Cl <sub>2</sub>	0.42	11
	CH <sub>3</sub> CN	0.11	11
	hexane	0.349	13
	toluene	0.673	13

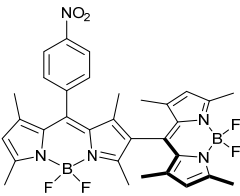
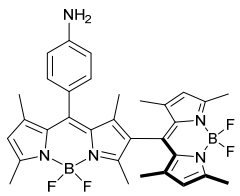
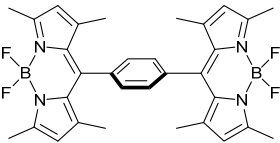
 <p style="text-align: center;"><b>34</b></p>	CH <sub>2</sub> Cl <sub>2</sub>	0.013	13
 <p style="text-align: center;"><b>35</b></p>	hexane	0.018	13
	toluene	0.246	13
 <p style="text-align: center;"><b>36</b></p>	hexane	0.28	14
	toluene	0.08	14
 <p style="text-align: center;"><b>37</b></p>	toluene	0.02	14
 <p style="text-align: center;"><b>38</b></p>	hexane	0.11	14
	toluene	0.42	14
 <p style="text-align: center;"><b>39</b></p>	toluene	0.23	15
	hexane	0.05	15

 <p style="text-align: center;"><b>40</b></p>	toluene	0.18	15
 <p style="text-align: center;"><b>41</b></p>	hexane	0.01	14
	toluene	0.39	14
 <p style="text-align: center;"><b>42</b></p>	hexane	0.02	14
	toluene	0.04	14
 <p style="text-align: center;"><b>43</b></p>	toluene	0.01	16
	THF	0.003	16
 <p style="text-align: center;"><b>44</b></p>	cyclohexane	0.04	16
	toluene	0.014	16
	THF	0.006	16
 <p style="text-align: center;"><b>45</b></p>	THF	0.008	16
	CH <sub>3</sub> CN	0.009	16
 <p style="text-align: center;"><b>46</b></p>	cyclohexane	0.30	16
	toluene	0.05	16
	THF	0.004	16
	toluene	0.033	17
	CH <sub>2</sub> Cl <sub>2</sub>	0.58	17

 <p><b>47</b></p>	CH <sub>3</sub> CN	0.024	17
 <p><b>48</b></p>	toluene	0.023	17
	CH <sub>2</sub> Cl <sub>2</sub>	0.082	17
	CH <sub>3</sub> CN	0.54	17
 <p><b>49</b></p>	toluene	0.083	17
	CH <sub>2</sub> Cl <sub>2</sub>	0.026	17
 <p><b>50</b></p>	toluene	0.09	18
 <p><b>51</b></p>	toluene	0.11	18
 <p><b>52</b></p>	toluene	0.19	18
 <p><b>53</b></p>	toluene	0.32	18
 <p><b>54</b></p>	CH <sub>2</sub> Cl <sub>2</sub>	0.022	17
	CH <sub>3</sub> CN	0.029	17





 <p style="text-align: center;"><b>62</b></p>	CH <sub>2</sub> Cl <sub>2</sub>	0.20	20
 <p style="text-align: center;"><b>63</b></p>	toluene	0.144	20
	CH <sub>2</sub> Cl <sub>2</sub>	0.68	20
	CH <sub>3</sub> CN	0.112	20
 <p style="text-align: center;"><b>64</b></p>	toluene	0.01	20
	CH <sub>2</sub> Cl <sub>2</sub>	0.09	20
	CH <sub>3</sub> CN	0.03	20

## 2. Synthetic Procedures and Characterization

### 2.1 Materials and Instruments

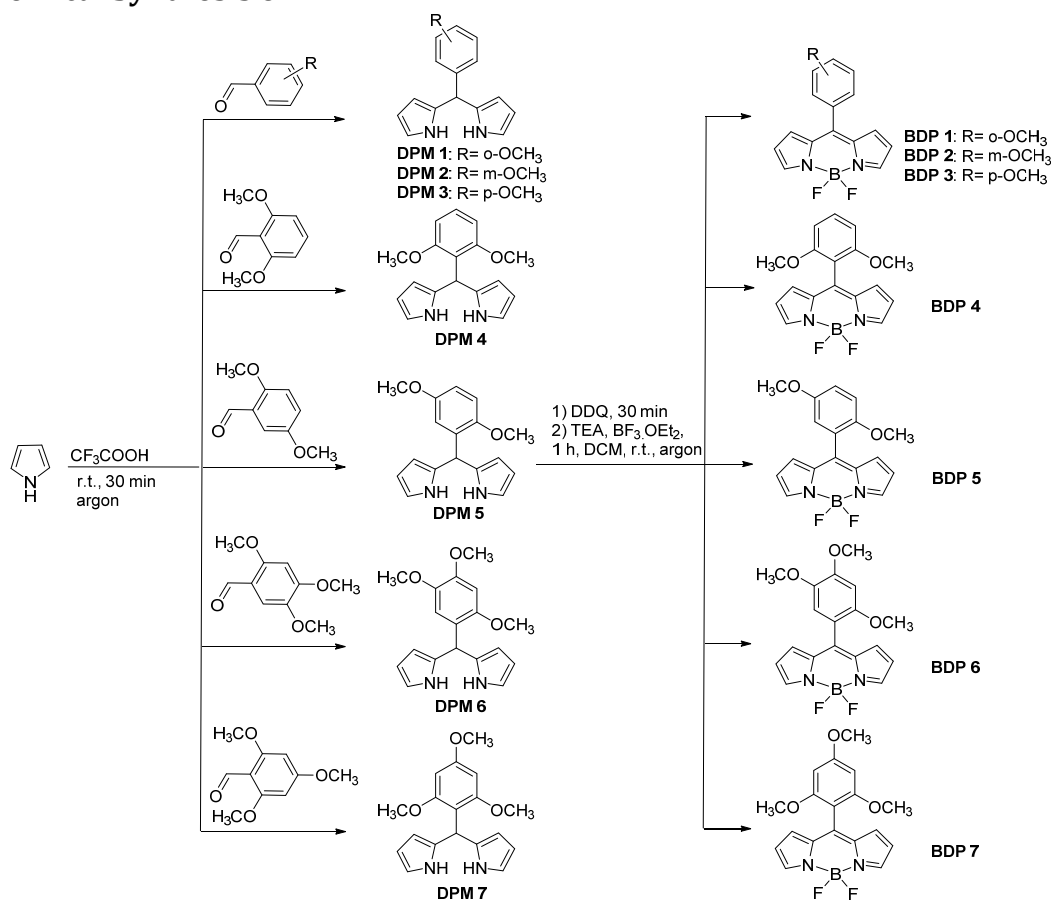
**General Information:** All reactions were performed in standard round-bottomed flasks under an argon atmosphere. All commercial reagents and solvents were used as received without further purification. Syringes were used for the addition of all liquid reagents. Yields refer to chromatographically and spectroscopically ( $^1\text{H}$  NMR) homogeneous material, unless otherwise noted. Reactions were monitored by thin layer chromatography (Merck, TLC Silica gel 60 F<sub>254</sub>) and visualized by UV irradiation ( $\lambda = 254$  nm). Flash column chromatography was carried out on silica gel 60 \*Merck, 230–400 mesh (mobile phases are given as (v/v)). Room temperature refers to 20–25 °C.

**Instrumentation:** Melting points are uncorrected and were measured on a Reichert Thermovar Apparatus. NMR spectra were recorded on a Bruker Advance III 400 MHz spectrometer for  $^1\text{H}$  (400 MHz),  $^{13}\text{C}$  (101 MHz),  $^{19}\text{F}$  (377 MHz) and  $^{11}\text{B}$  (128 MHz) NMR spectra. All NMR spectra were recorded at 25 °C. Resonances  $\delta$  are given in ppm units and referenced to the deuterium peak in the NMR solvent:  $\text{CDCl}_3$  ( $\delta_{\text{H}} = 7.26$  ppm,  $\delta_{\text{C}} = 77.2$  ppm). Signal multiplicities are abbreviated as follows: singlet = s, doublet = d, triplet = t, doublet of doublets = dd, multiplet = m. HRMS analyses were acquired in positive modes as required, using a Micromass time-of-flight mass spectrometer (TOF) interfaced to a Waters 2960 HPLC or a Bruker microTOF-Q III spectrometer interfaced to a Dionex UltiMate 3000 LC.

UV-Vis spectra were recorded in solutions using a PerkinElmer Lambda 900 UV/VIS/NIR Spectrometer (1 cm path length quartz cell). Emission spectra were measured using a PerkinElmer LS 55 Luminescence Spectrometer. Emission quantum yields of the compounds were measured relative to the fluorescence of rhodamine 6G in EtOH ( $\Phi_{\text{F}} = 0.95$ ).<sup>22</sup>

Photo-irradiations were performed in quartz cuvettes (1 cm) using a Melles Griot 43 series ion laser (543R-AP-AO1, average intensity of 12 mW cm<sup>-2</sup>).

### 2.2 Chemical Synthesis of BDP 1-7



**Scheme S1.** Synthesis of BODIPY compounds.

**General Procedure 1:** Dipyrromethane (**DPM 4-7**) (1 equiv) was dissolved in CH<sub>2</sub>Cl<sub>2</sub>, degassed with an Ar stream for 5 min and oxidized with DDQ (1.2 equiv) for half an hour. To this mixture TEA (40 equiv) and BF<sub>3</sub>·OEt<sub>2</sub> (50 equiv) were added without any time delay under Ar atm. and allowed to stir at room temperature for 1 h. After 1 h, extractions were carried out with water and the organic extract was collected, dried with anhydrous Na<sub>2</sub>SO<sub>4</sub> and the solvents were removed under reduced pressure. The crude products were subjected to silica gel column chromatography in order to obtain the desired pure compounds.

**BDP 4.** Synthesized via General Procedure 1 from dipyrromethane (**DPM 4**) (200 mg, 0.71 mmol), DDQ (193 mg, 0.85 mmol), TEA (3.9 mL, 28.32 mmol) and TFA (4.4 mL, 35.4 mmol) in 90 mL CH<sub>2</sub>Cl<sub>2</sub>. The crude material was purified by silica gel column chromatography. Desired product was eluted with (70/30) CH<sub>2</sub>Cl<sub>2</sub>/hexane mixture. Final purification was performed through recrystallization in a MeOH/H<sub>2</sub>O mixture giving **BDP 4** as a green solid. Yield= 160 mg of **BDP 4** (0.49 mmol, 69%). m.p. = 131-140 °C; *R<sub>f</sub>* = 0.50 (SiO<sub>2</sub>, CH<sub>2</sub>Cl<sub>2</sub>/hexane, 7:3, v/v); <sup>1</sup>H NMR (400 MHz, CDCl<sub>3</sub>): δ = 7.86 (s, 2H), 7.41 (t, *J* = 8.4 Hz, 1H), 6.74 (d, *J* = 4.1 Hz, 2H), 6.66 (d, *J* = 8.4 Hz, 2H), 6.43 (d, *J* = 3.0 Hz, 2H), 3.69 ppm (s, 6H); <sup>13</sup>C NMR (101 MHz, CDCl<sub>3</sub>): δ = 158.59, 143.60, 136.37, 131.45, 130.37, 117.98, 111.03, 104.00, 56.09 ppm; <sup>19</sup>F NMR (377 MHz, CDCl<sub>3</sub>): δ = δ -145.33 ppm (dd, *J* = 58.4, 29.1 Hz, 2 F); <sup>11</sup>B NMR (128 MHz, CDCl<sub>3</sub>): δ = 0.34 ppm (t, *J* = 28.8 Hz); UV-Vis (CH<sub>2</sub>Cl<sub>2</sub>): λ<sub>max</sub> {log (ε [L mol<sup>-1</sup> cm<sup>-1</sup>])} = 507 nm (4.75); HRMS (ESI-QTOF): *m/z* calcd for C<sub>17</sub>H<sub>15</sub>BF<sub>2</sub>N<sub>2</sub>NaO<sub>2</sub> [M+Na]<sup>+</sup> 351.108996; found 351.108910.

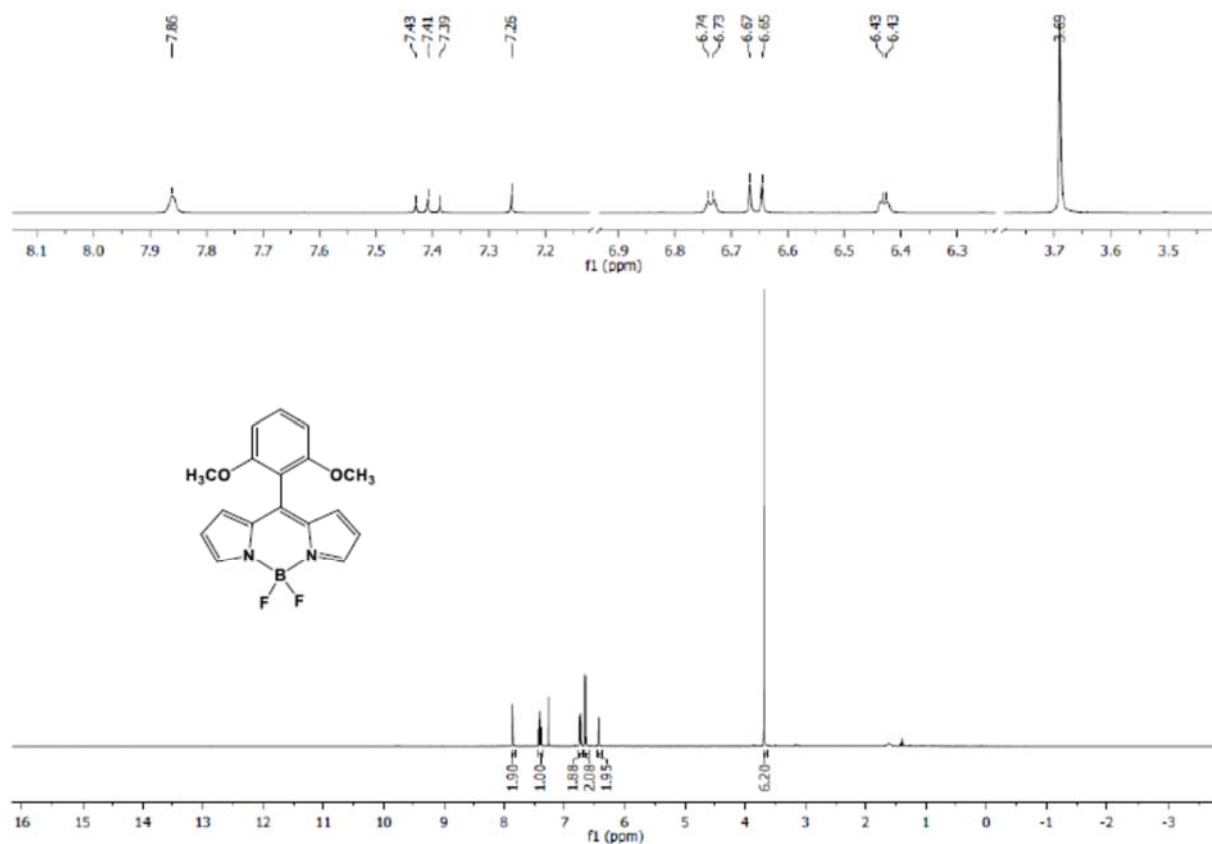
**BDP 5.** Synthesized via General Procedure 1 from **DPM 5** (200 mg, 0.71 mmol), DDQ (193 mg, 0.85 mmol), TEA (3.9 mL, 28.32 mmol) and TFA (4.4 mL, 35.4 mmol) in 90 mL CH<sub>2</sub>Cl<sub>2</sub>. The crude material was purified by silica gel column chromatography. Desired product was eluted with (60/40) CH<sub>2</sub>Cl<sub>2</sub>/hexane mixture. Final purification was performed through recrystallization in a MeOH/H<sub>2</sub>O mixture giving **BDP 5** as an orange powder. Yield= 152 mg of **BDP 5** (0.46 mmol, 65%). m.p. = 108-110 °C; *R<sub>f</sub>* = 0.55 (SiO<sub>2</sub>, CH<sub>2</sub>Cl<sub>2</sub>/hexane, 3:2, v/v); <sup>1</sup>H NMR (400 MHz, CDCl<sub>3</sub>): δ = 7.89 (s, 2H), 7.03 (dd, *J* = 9.0, 3.0 Hz, 1H), 6.97 (d, *J* = 9.0 Hz, 1H), 6.88 (d, *J* = 3.0 Hz, 1H), 6.83 (d, *J* = 4.0 Hz, 2H), 6.48 (d, *J* = 3.3 Hz, 2H), 3.79 (s, 3H), 3.69 (s, 3H) ppm; <sup>13</sup>C NMR (101 MHz, CDCl<sub>3</sub>): δ = 153.16, 151.40, 144.11, 135.75, 131.30, 123.26, 118.38, 117.40, 116.58, 112.87, 56.45, 56.00 ppm; <sup>19</sup>F NMR (377 MHz, CDCl<sub>3</sub>): δ = -144.37 (m, 1 F), -146.09 (m, 1 F) ppm; <sup>11</sup>B NMR (128 MHz, CDCl<sub>3</sub>): δ = 0.29 (t, *J* = 28.7 Hz) ppm; UV-Vis (CH<sub>2</sub>Cl<sub>2</sub>): λ<sub>max</sub> {log (ε [L mol<sup>-1</sup> cm<sup>-1</sup>])} = 506 nm (4.85); HRMS (ESI-QTOF): *m/z* calcd for C<sub>17</sub>H<sub>15</sub>BF<sub>2</sub>N<sub>2</sub>NaO<sub>2</sub> [M+Na]<sup>+</sup> 351.108996; found 351.108698.

**BDP 6.** Synthesized via General Procedure 1 from dipyrromethane (**DPM 6**) (200 mg, 0.64 mmol), DDQ (175 mg, 0.77 mmol), TEA (3.6 mL, 25.61 mmol) and TFA (3.9 mL, 32.01 mmol) in 80 mL CH<sub>2</sub>Cl<sub>2</sub>. The crude material was purified by silica gel column chromatography. Desired product was eluted with (90/10) CH<sub>2</sub>Cl<sub>2</sub>/hexane mixture. Final purification was performed through recrystallization in a MeOH/H<sub>2</sub>O mixture giving the final BODIPY compound as a green solid. Yield= 200 mg of **BDP 6** (0.56 mmol, 87%). m.p. = 115-124 °C; *R<sub>f</sub>* = 0.46 (SiO<sub>2</sub>, CH<sub>2</sub>Cl<sub>2</sub>/hexane, 9:1, v/v); <sup>1</sup>H NMR (400 MHz, CDCl<sub>3</sub>): δ = 7.88 (s, 2H), 6.91 – 6.81 (m, 3H), 6.64 (s, 1H), 6.49 (dd, *J* = 4.1, 1.5 Hz, 2H), 3.99 (s, 3H), 3.83 (s, 3H), 3.72 (s, 3H) ppm; <sup>13</sup>C NMR (101 MHz, CDCl<sub>3</sub>): δ = 152.11, 151.70, 143.62, 142.87, 135.92, 131.21, 118.20, 115.45, 113.88, 97.84, 56.78, 56.75, 56.33 ppm; <sup>19</sup>F NMR (377 MHz, CDCl<sub>3</sub>): δ = -144.31 (m, 1 F), -146.25 (m, 1 F) ppm; <sup>11</sup>B NMR (128 MHz, CDCl<sub>3</sub>): δ = 0.29 (t, *J* = 28.8 Hz) ppm; UV-Vis (CH<sub>2</sub>Cl<sub>2</sub>): λ<sub>max</sub> {log (ε [L mol<sup>-1</sup> cm<sup>-1</sup>])} = 506 nm (4.68); HRMS (ESI-QTOF): *m/z* calcd for C<sub>17</sub>H<sub>15</sub>BF<sub>2</sub>N<sub>2</sub>NaO<sub>2</sub> [M+Na]<sup>+</sup> 381.119579; found 381.119879.

**BDP 7.** Synthesized via General Procedure 1 from **DPM 7** (200 mg, 0.64 mmol), DDQ (175 mg, 0.77 mmol), TEA (3.6 mL, 25.61 mmol) and TFA (3.9 mL, 32.01 mmol) in 80 mL CH<sub>2</sub>Cl<sub>2</sub>. The crude material was purified by silica gel column chromatography. Desired product was eluted with CH<sub>2</sub>Cl<sub>2</sub>/EtOH (1%) mixture. Final purification was performed through recrystallization in a MeOH/H<sub>2</sub>O mixture giving **BDP 7** as an orange solid. Yield= 125 mg of **BDP 7** (0.35 mmol, 55%). m.p. = 114-126 °C; *R<sub>f</sub>* = 0.60 (SiO<sub>2</sub>, CH<sub>2</sub>Cl<sub>2</sub>/EtOH, 9.9:0.1, v/v); <sup>1</sup>H NMR (400 MHz, CDCl<sub>3</sub>): δ = 7.84 (s, 2H), 6.76 (d, *J* = 4.2 Hz, 2H), 6.46 – 6.38 (m, 2H), 6.21 (s, 2H), 3.89 (s, 3H), 3.67 (s, 6H) ppm; <sup>13</sup>C NMR (101 MHz, CDCl<sub>3</sub>): δ = 162.89, 159.43, 143.30, 136.79, 130.42, 117.86, 103.92, 90.77, 56.01, 55.62 ppm; <sup>19</sup>F NMR (377 MHz, CDCl<sub>3</sub>): δ = -145.36

(dd,  $J = 58.5, 29.0$  Hz, 2 F) ppm;  $^{11}\text{B}$  NMR (128 MHz,  $\text{CDCl}_3$ ):  $\delta = 0.33$  (t,  $J = 28.9$  Hz) ppm; UV-Vis ( $\text{CH}_2\text{Cl}_2$ ):  $\lambda_{\text{max}} \{\log(\epsilon [\text{L mol}^{-1} \text{cm}^{-1}])\} = 507$  nm (4.81); HRMS (ESI-QTOF):  $m/z$  calcd for  $\text{C}_{17}\text{H}_{15}\text{BF}_2\text{N}_2\text{NaO}_2$  [ $\text{M}+\text{Na}$ ] $^+$  381.119579; found 381.119449.

### 2.3 NMR and HRMS Data



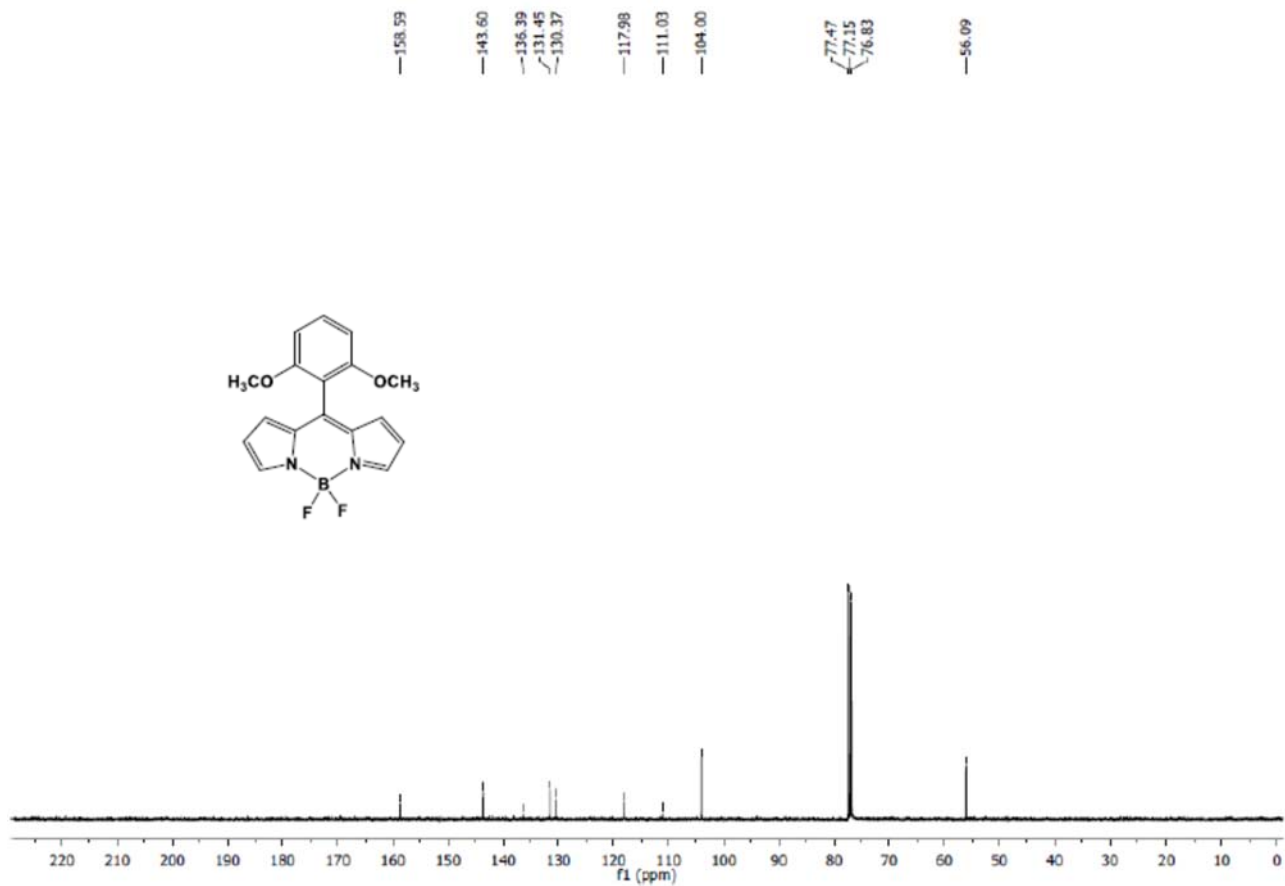


**Figure S2.** <sup>13</sup>C NMR spectrum of BDP-4 (101 MHz, CDCl<sub>3</sub>, 25 °C).

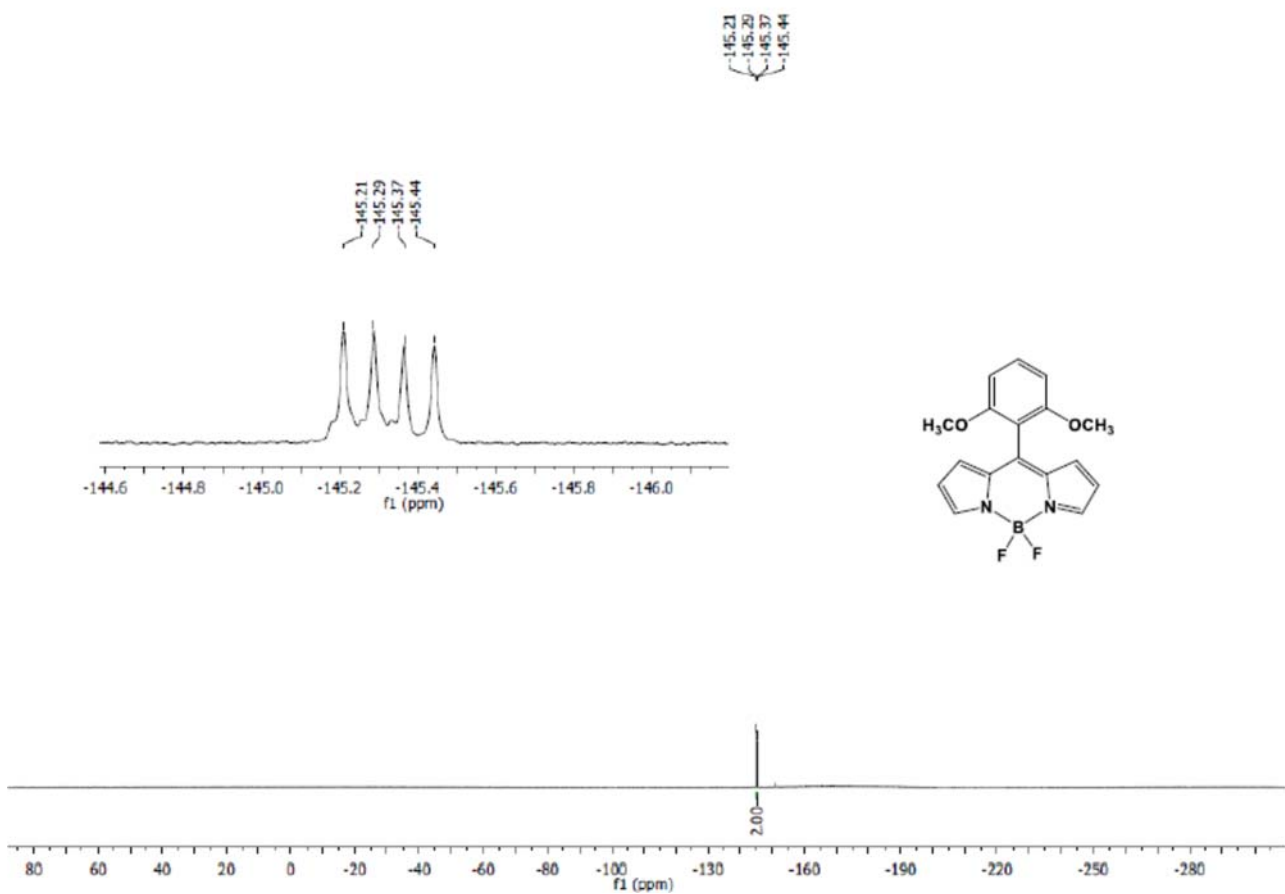


**Figure S3.** <sup>19</sup>F NMR spectrum of BDP-4 (377 MHz, CDCl<sub>3</sub>, 25 °C).

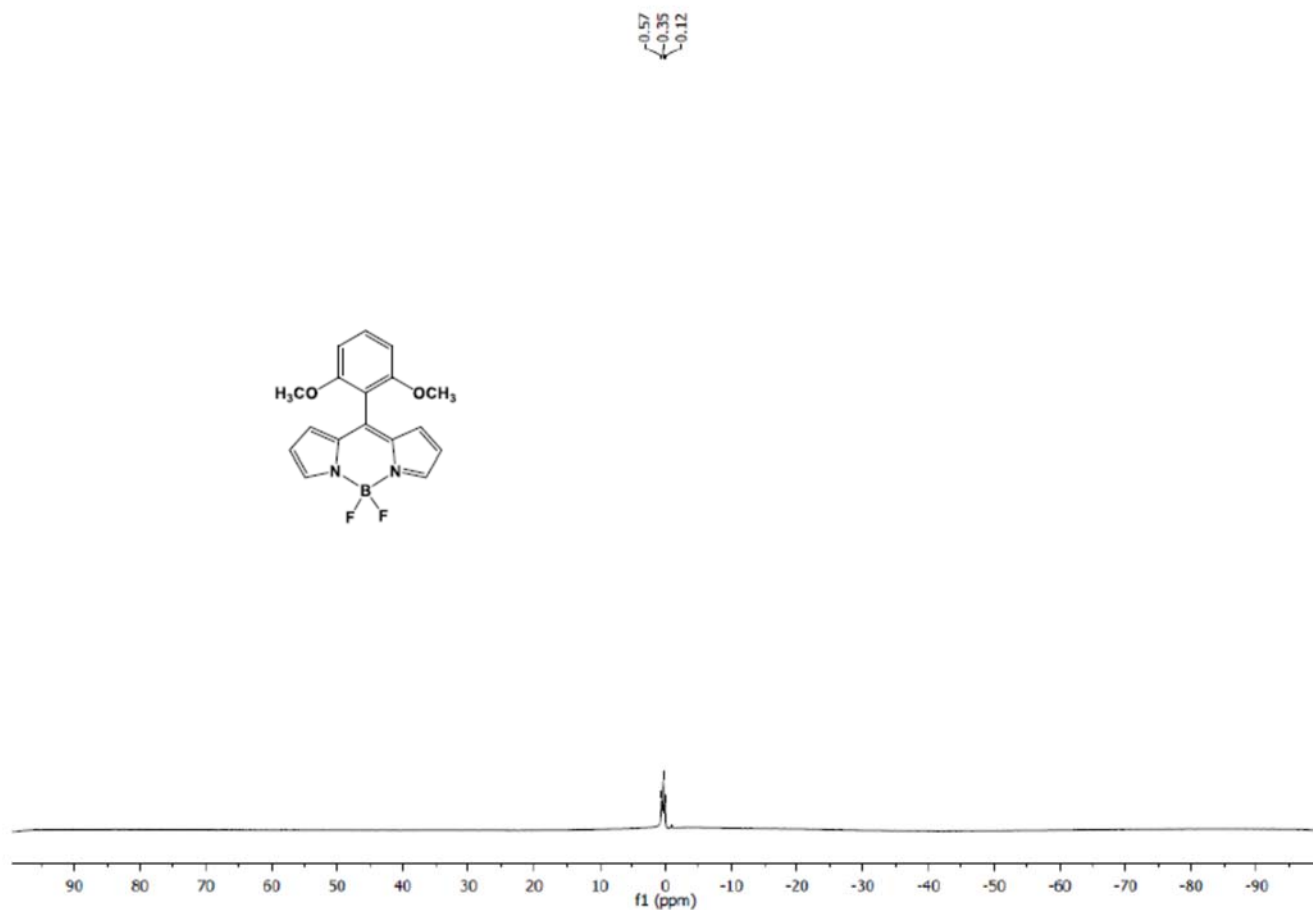


**Figure S4.**  $^{11}\text{B}$  NMR spectrum of **BDP-4** (128 MHz,  $\text{CDCl}_3$ , 25 °C).

Sample-ID		Station
Submitter		Supervisor
Analysis Name	AST-2020-11_RA6_01_23760.d	Acquisition Date
Sample Description		30/09/2020 11:59:26

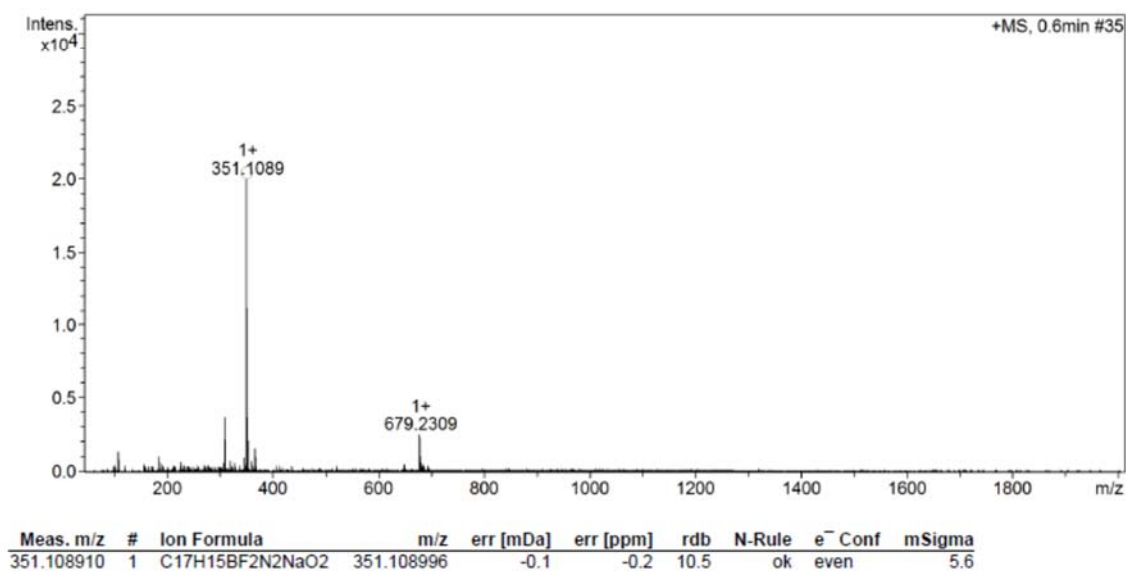


**Figure S5.** ESI-MS of **BDP-4**.

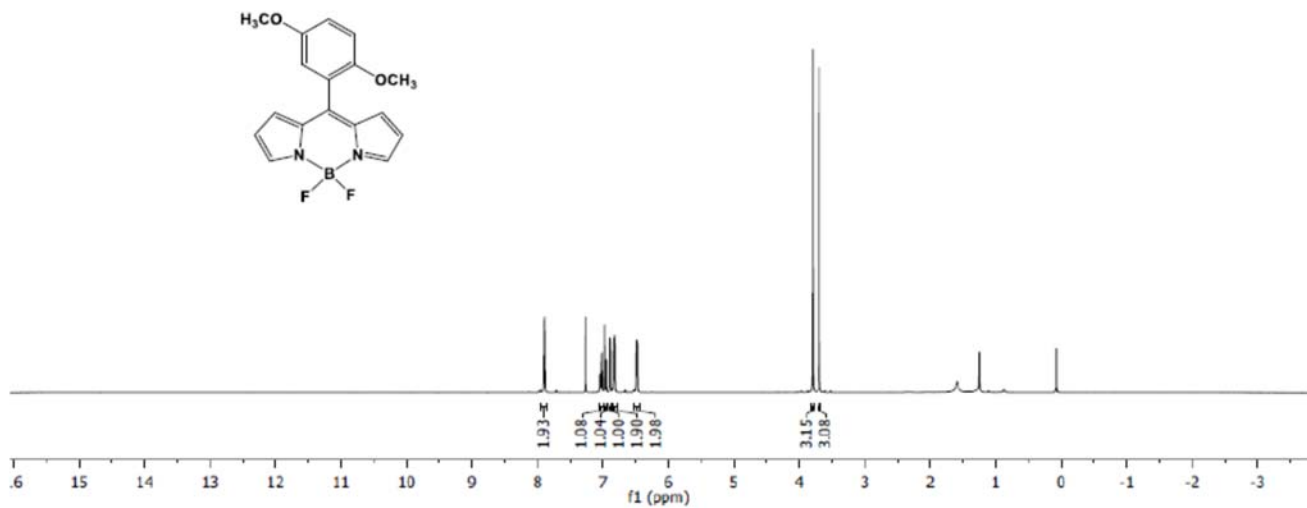
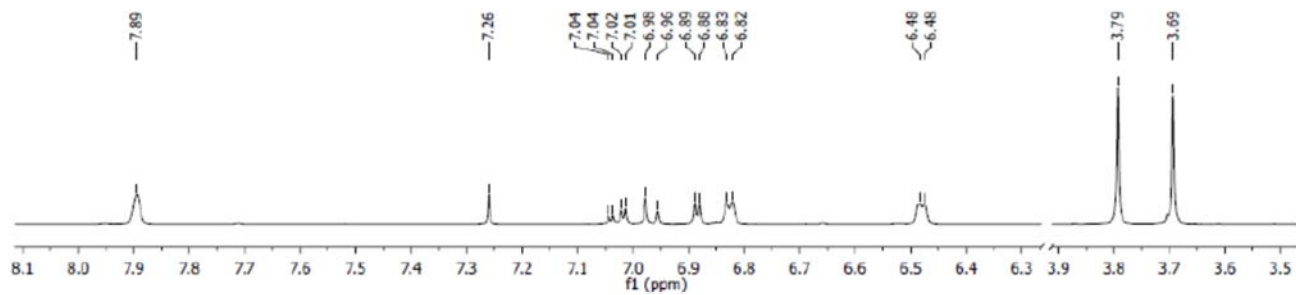


**Figure 6.**  $^1\text{H NMR}$  spectrum of **BDP-5** (400 MHz,  $\text{CDCl}_3$ , 25 °C).

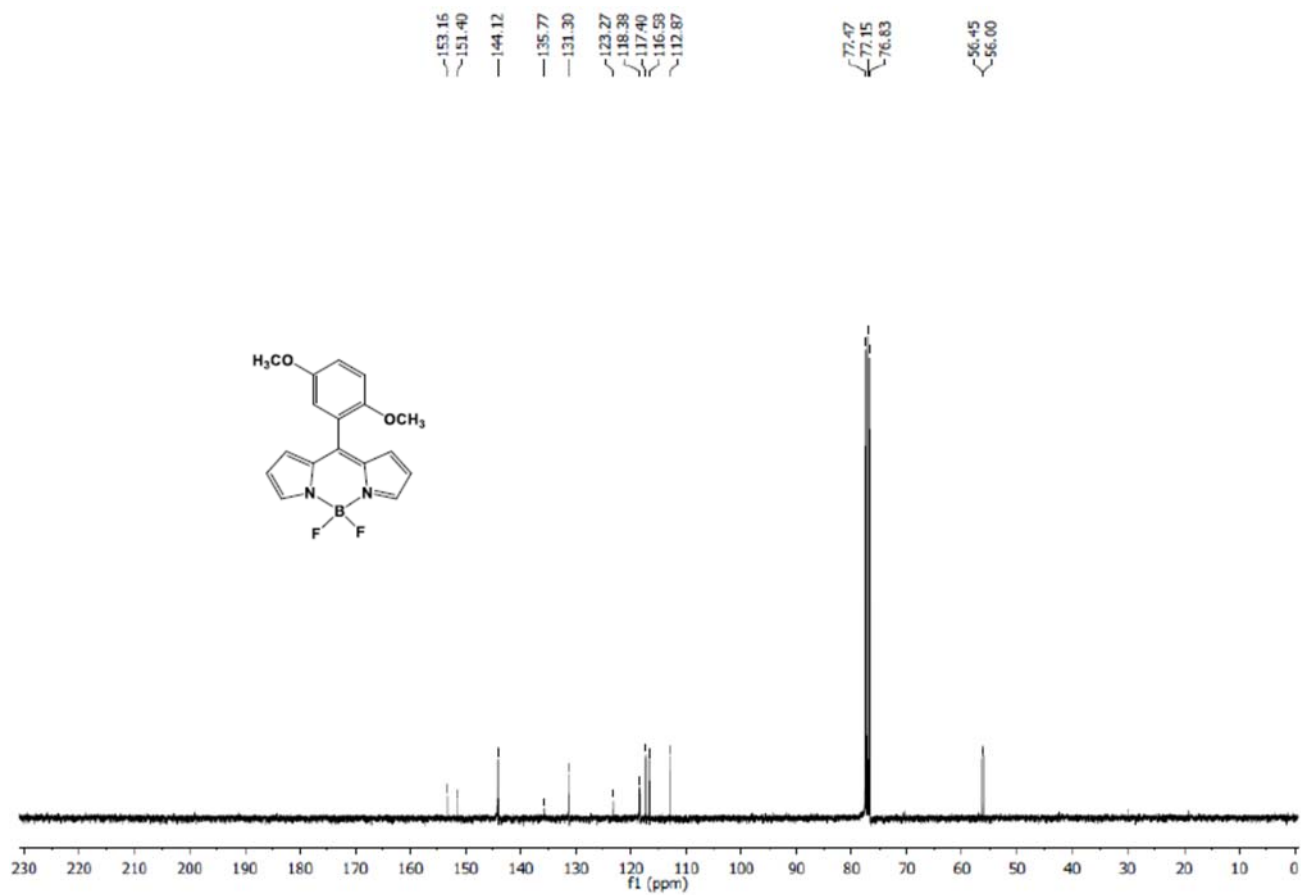


**Figure S7.**  $^{13}\text{C NMR}$  spectrum of **BDP-5** (101 MHz,  $\text{CDCl}_3$ , 25 °C).

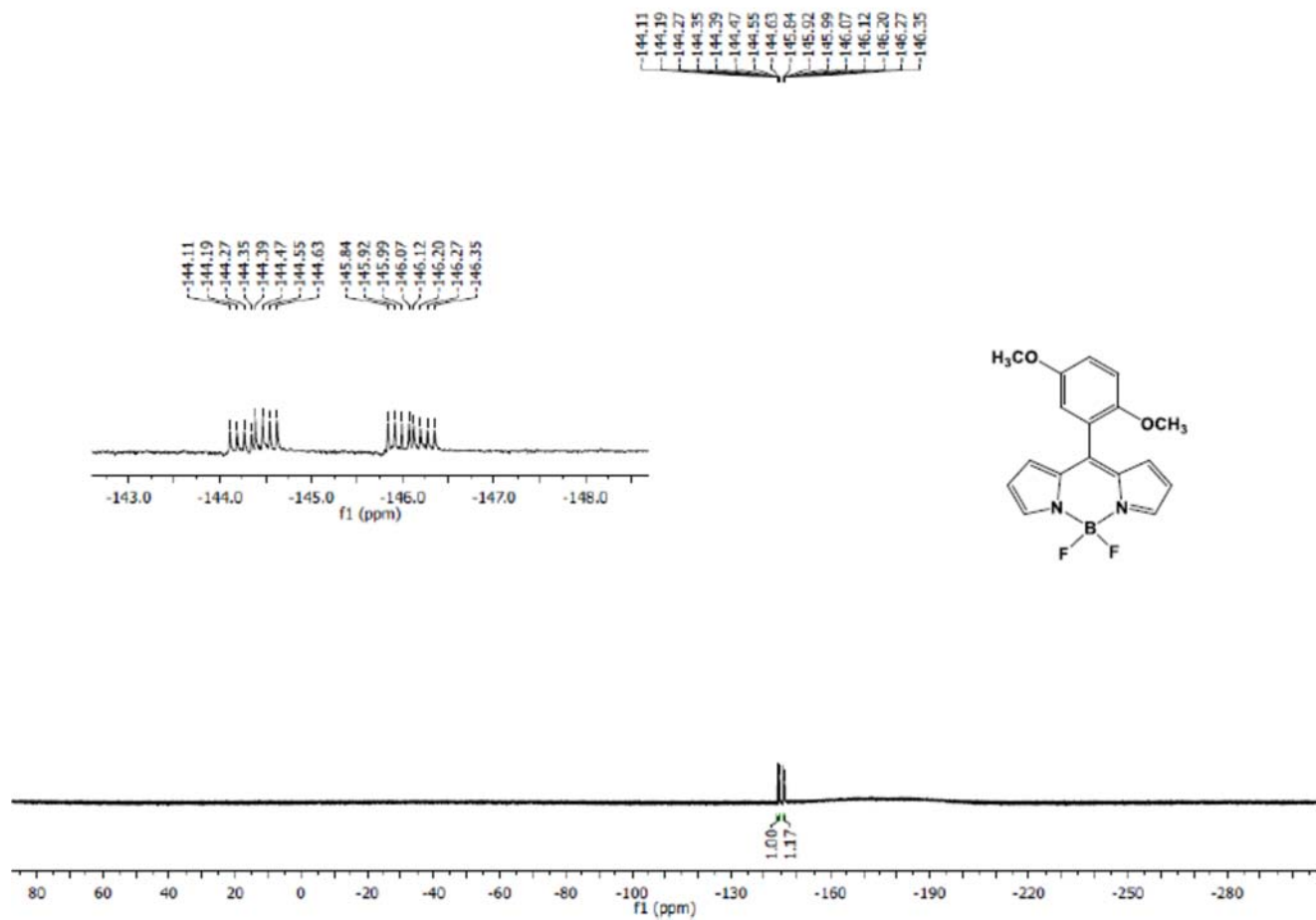


**Figure S8.** <sup>19</sup>F NMR spectrum of BDP-5 (377 MHz, CDCl<sub>3</sub>, 25 °C).

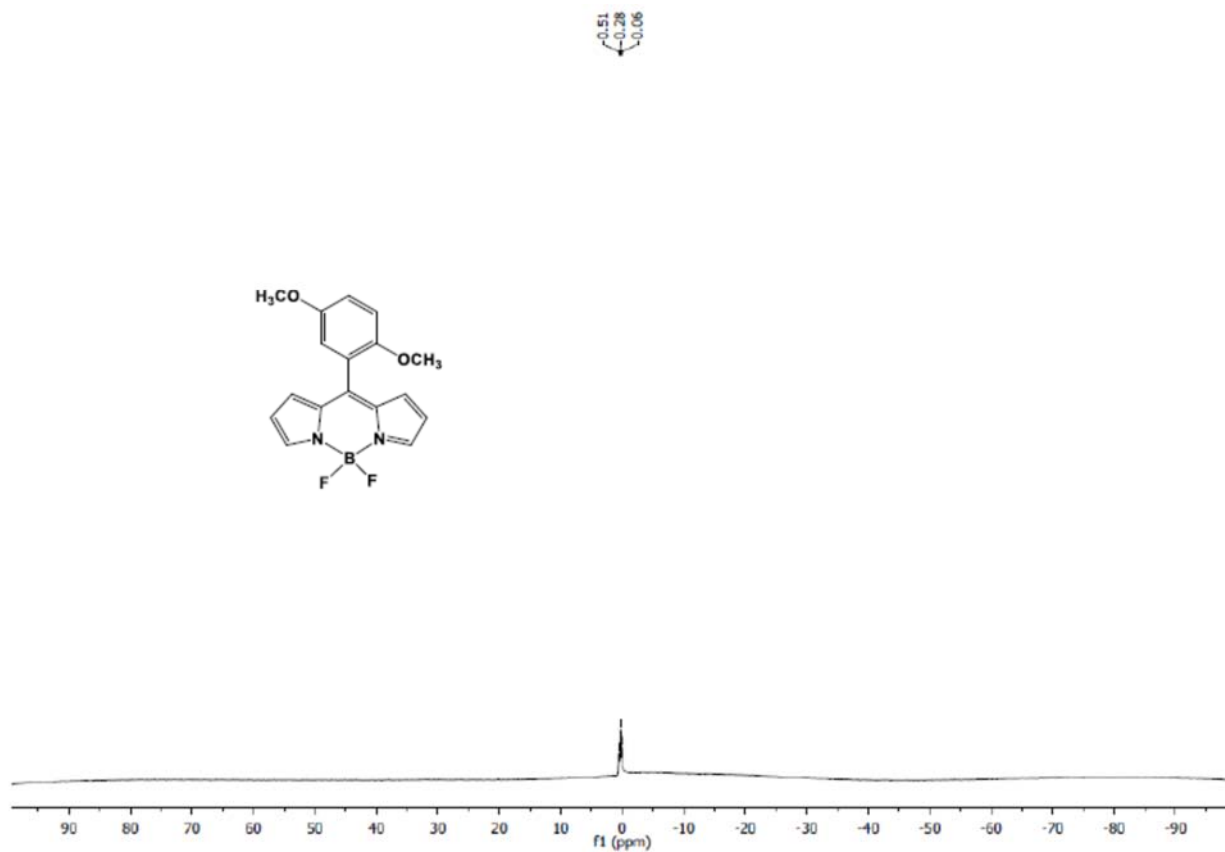


**Figure S9.** <sup>11</sup>B NMR spectrum of BDP-5 (128 MHz, CDCl<sub>3</sub>, 25 °C).



Sample-ID  
 Submitter  
 Analysis Name AST-2020-12\_RA7\_01\_23761.d  
 Sample Description

Station  
 Supervisor  
 Acquisition Date 30/09/2020 12:02:46

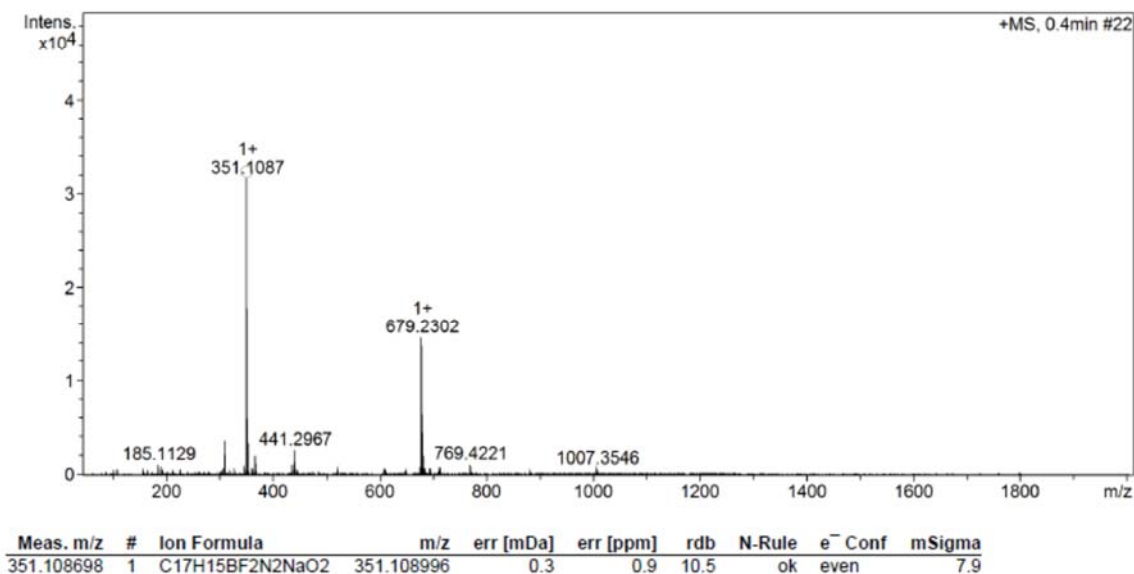


Figure S10. ESI-MS of BDP-5.

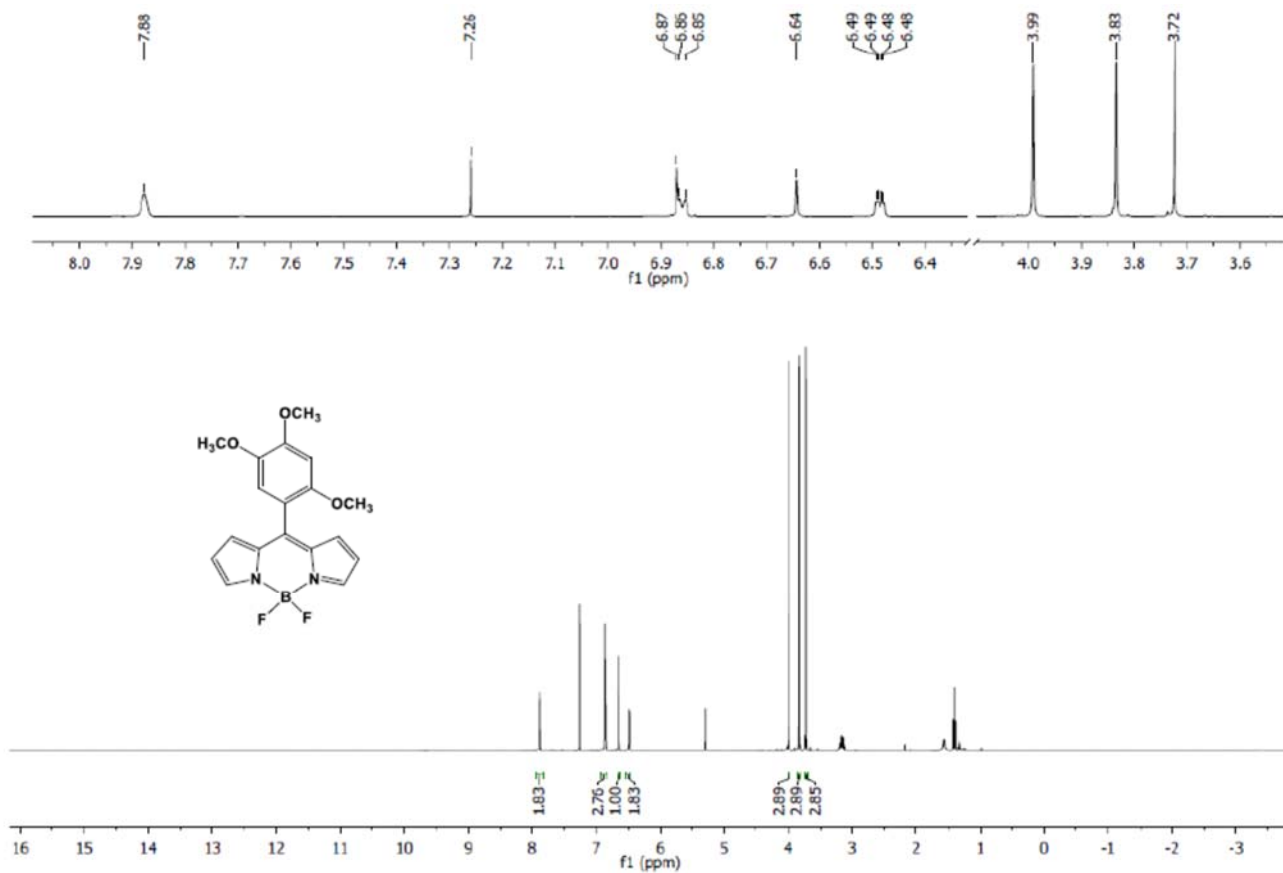


Figure S11. <sup>1</sup>H NMR spectrum of BDP-6 (400 MHz, CDCl<sub>3</sub>, 25 °C).

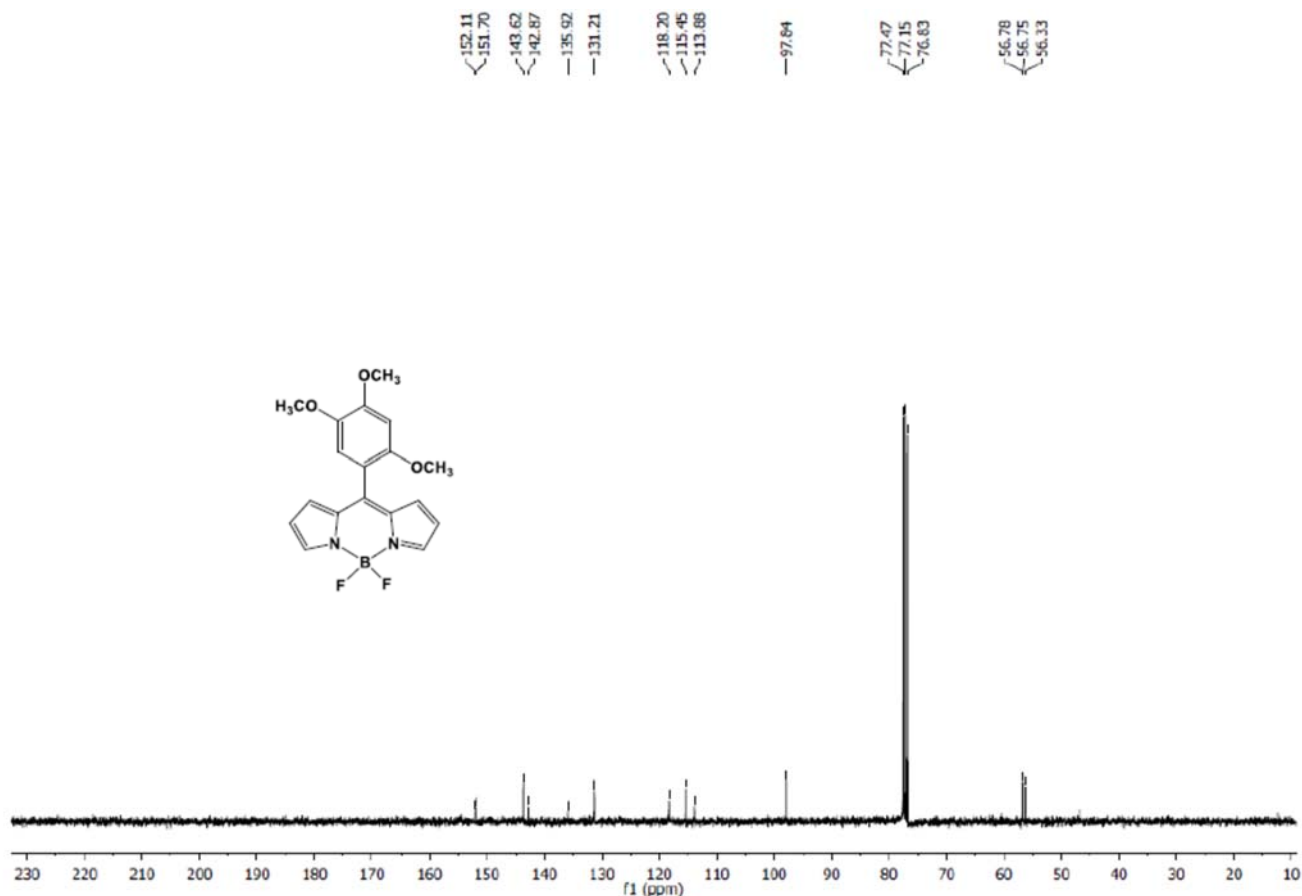


Figure S12.  $^{13}\text{C}$  NMR spectrum of BDP-6 (101 MHz,  $\text{CDCl}_3$ , 25 °C).

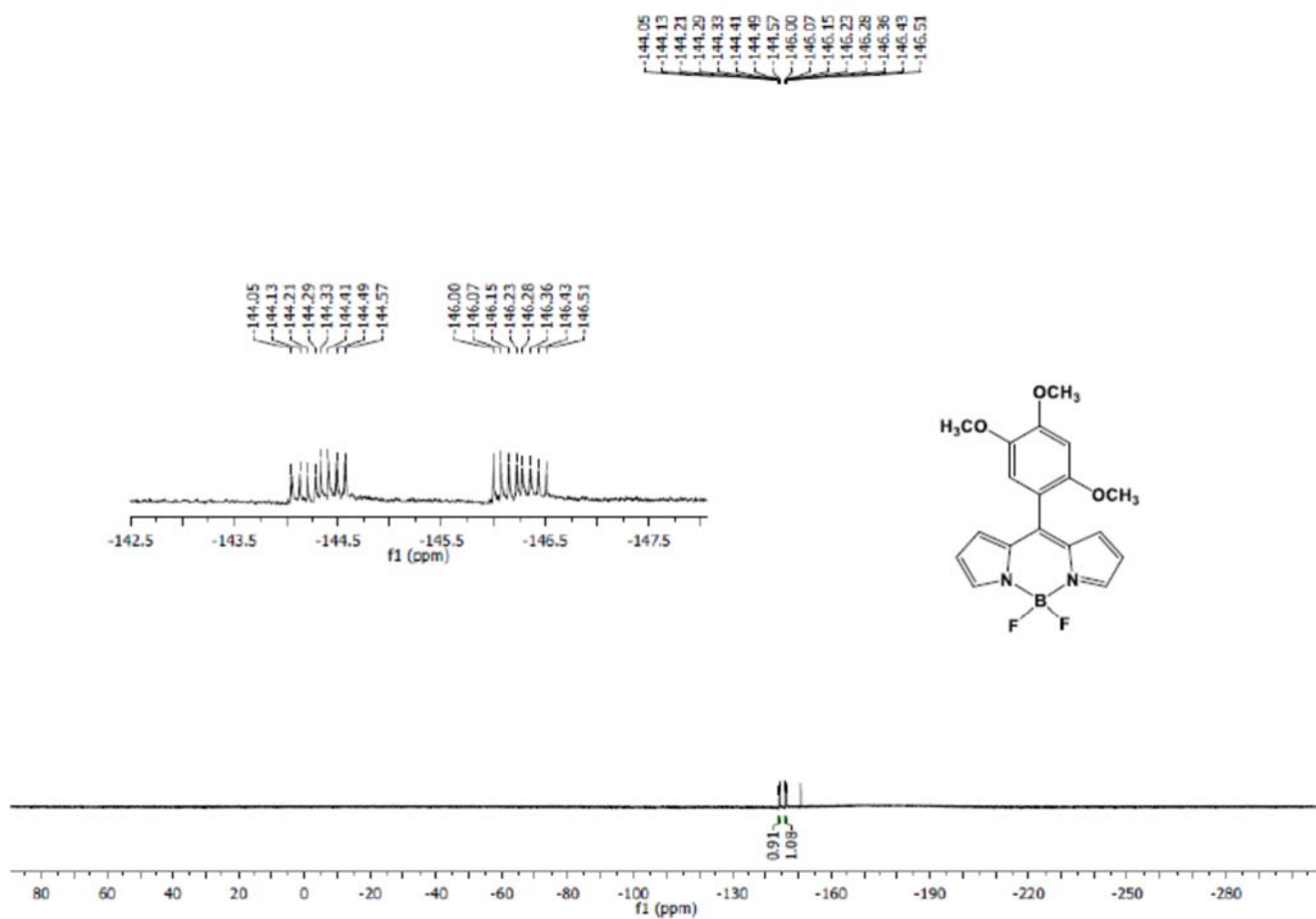
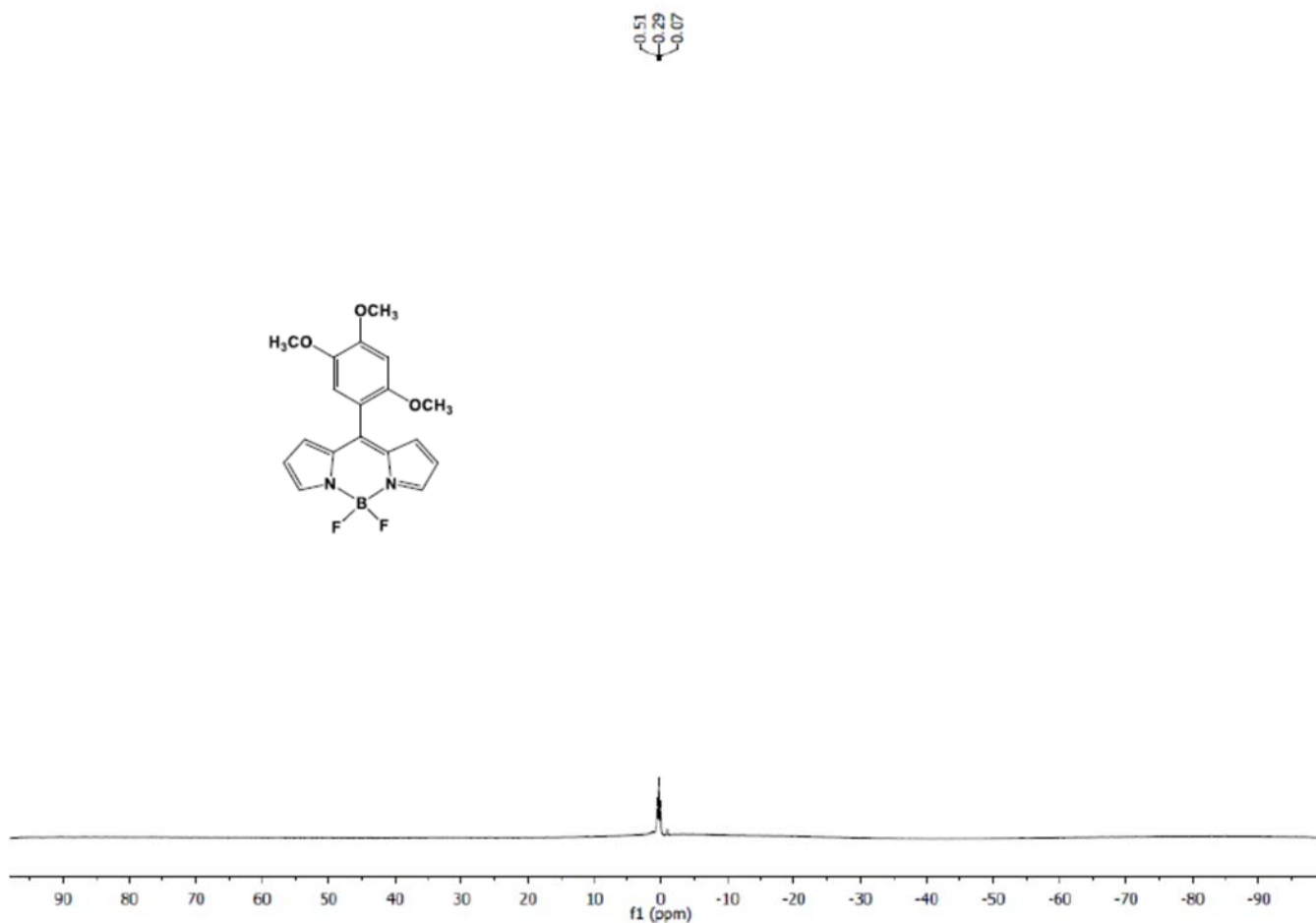
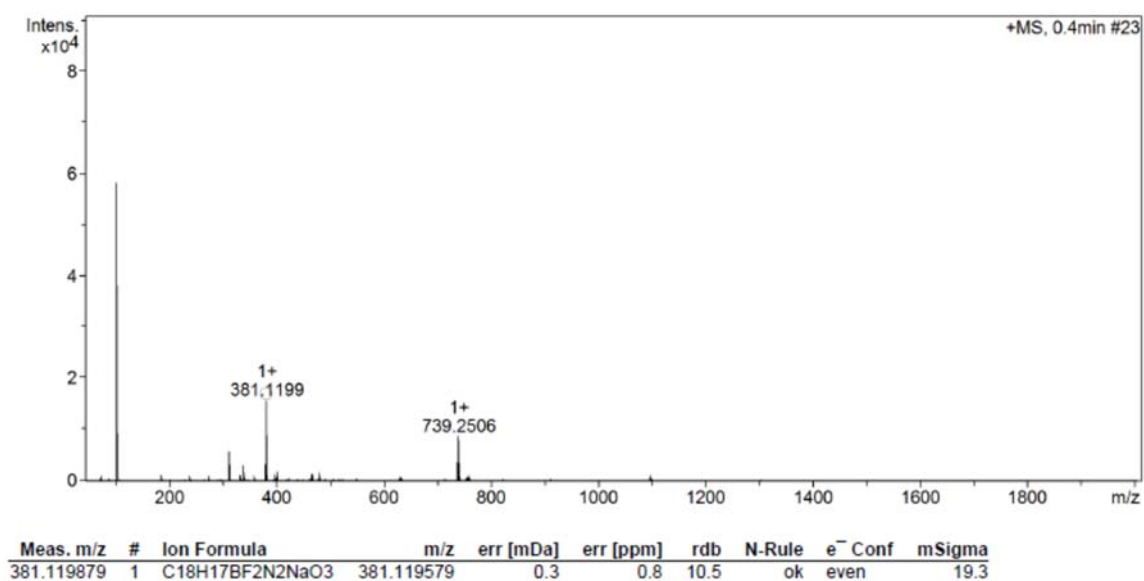


Figure S13.  $^{19}\text{F}$  NMR spectrum of BDP-6 (377 MHz,  $\text{CDCl}_3$ , 25 °C).



**Figure S14.**  $^{11}\text{B}$  NMR spectrum of **BDP-6** (128 MHz,  $\text{CDCl}_3$ , 25 °C).

Sample-ID		Station
Submitter		Supervisor
Analysis Name	AST-2020-13_RA8_01_23762.d	Acquisition Date
Sample Description		30/09/2020 12:06:05



**Figure S15.** ESI-MS of **BDP-6**.

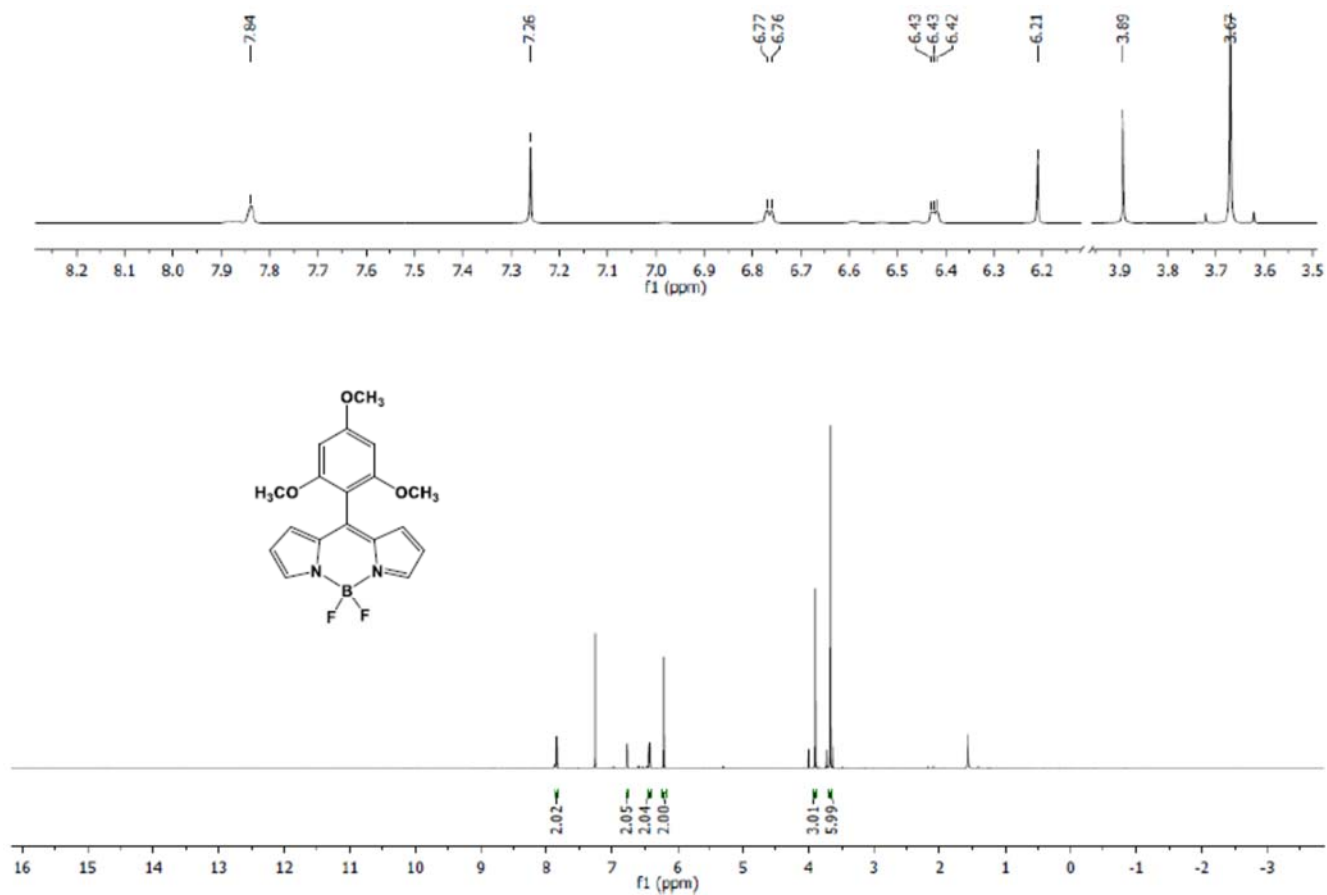


**Figure S16.** <sup>1</sup>H NMR spectrum of **BDP-7** (400 MHz, *CDCl*<sub>3</sub>, 25 °C).

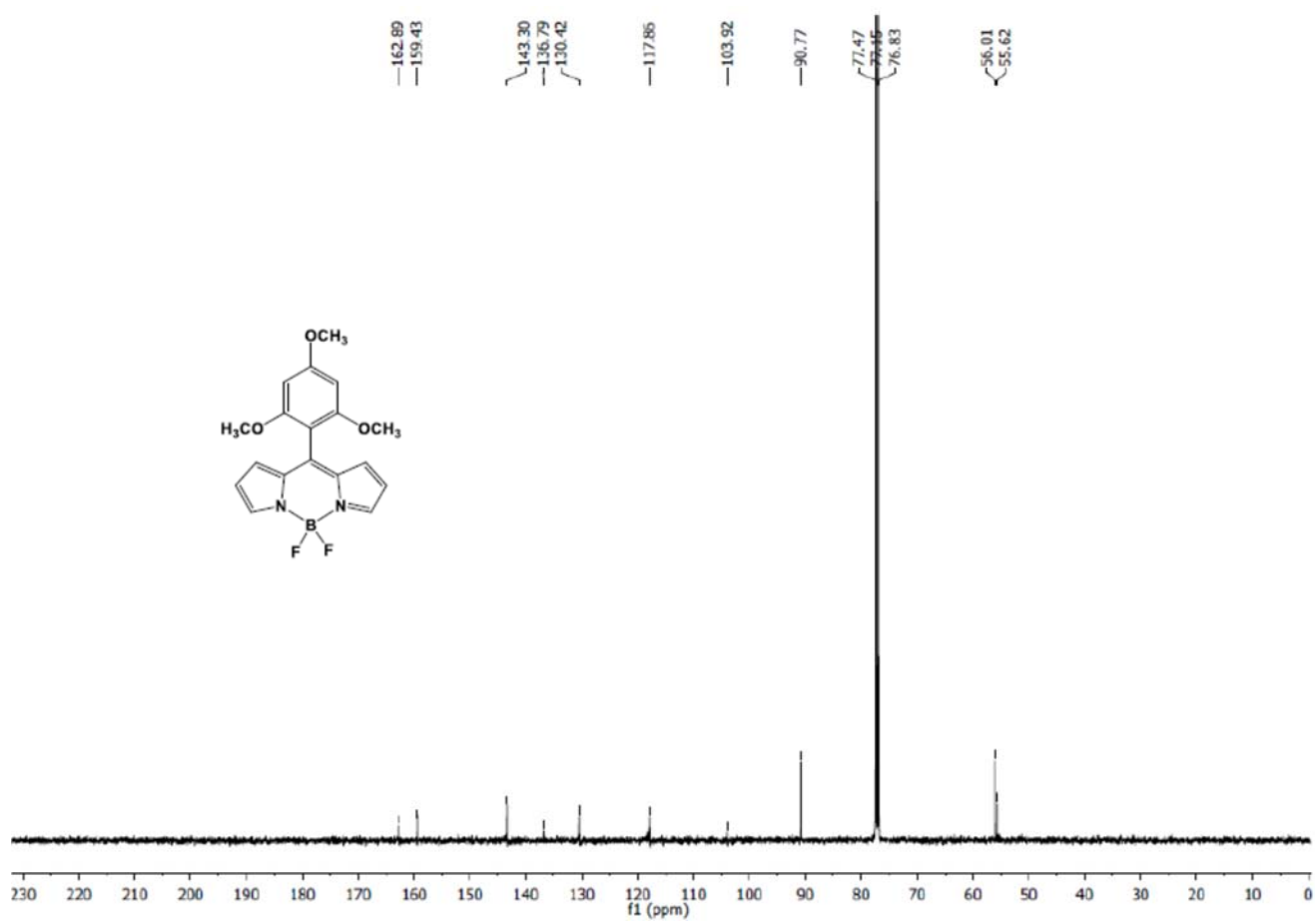


**Figure S17.** <sup>13</sup>C NMR spectrum **BDP-7** (101 MHz, *CDCl*<sub>3</sub>, 25 °C).

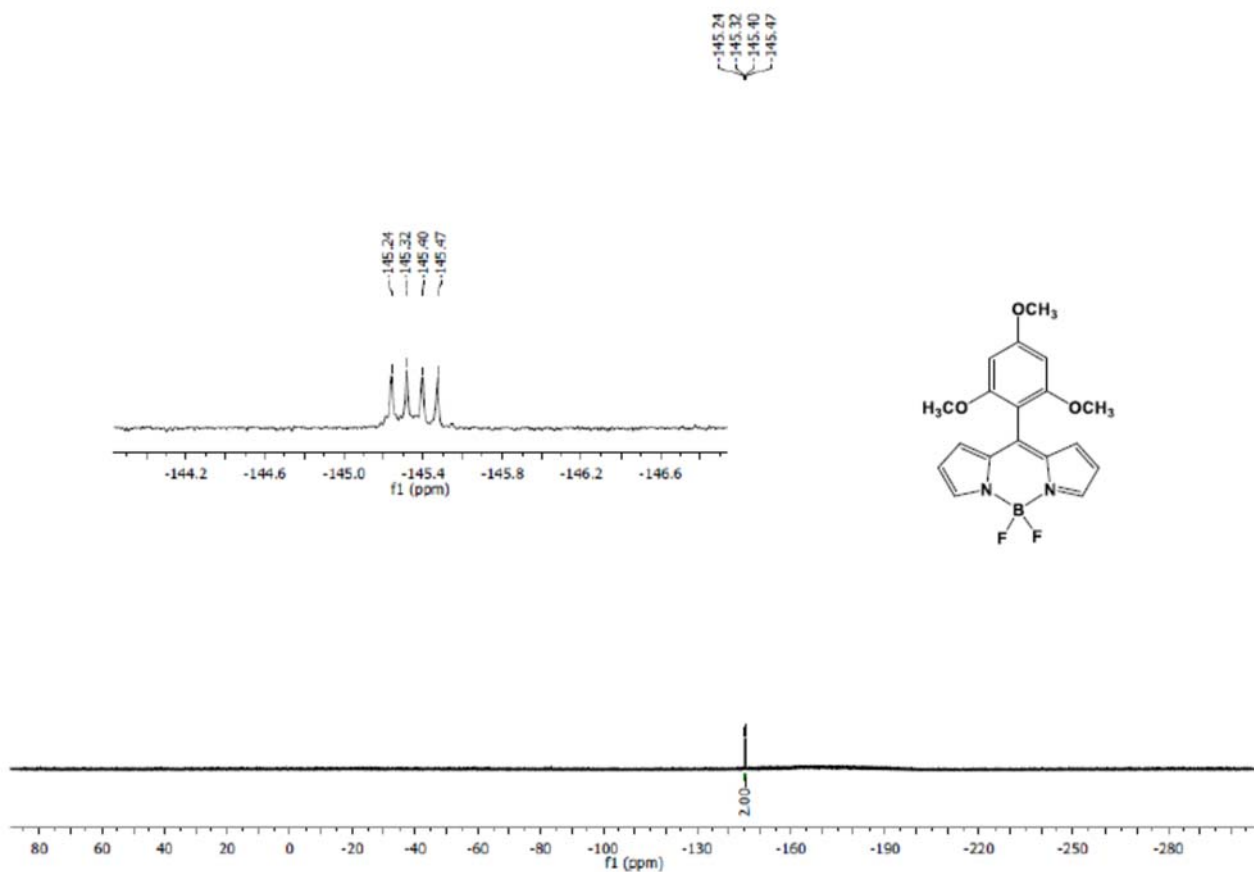


**Figure S18.**  $^{19}\text{F}$  NMR spectrum of **BDP-7** (377 MHz,  $\text{CDCl}_3$ , 25 °C).

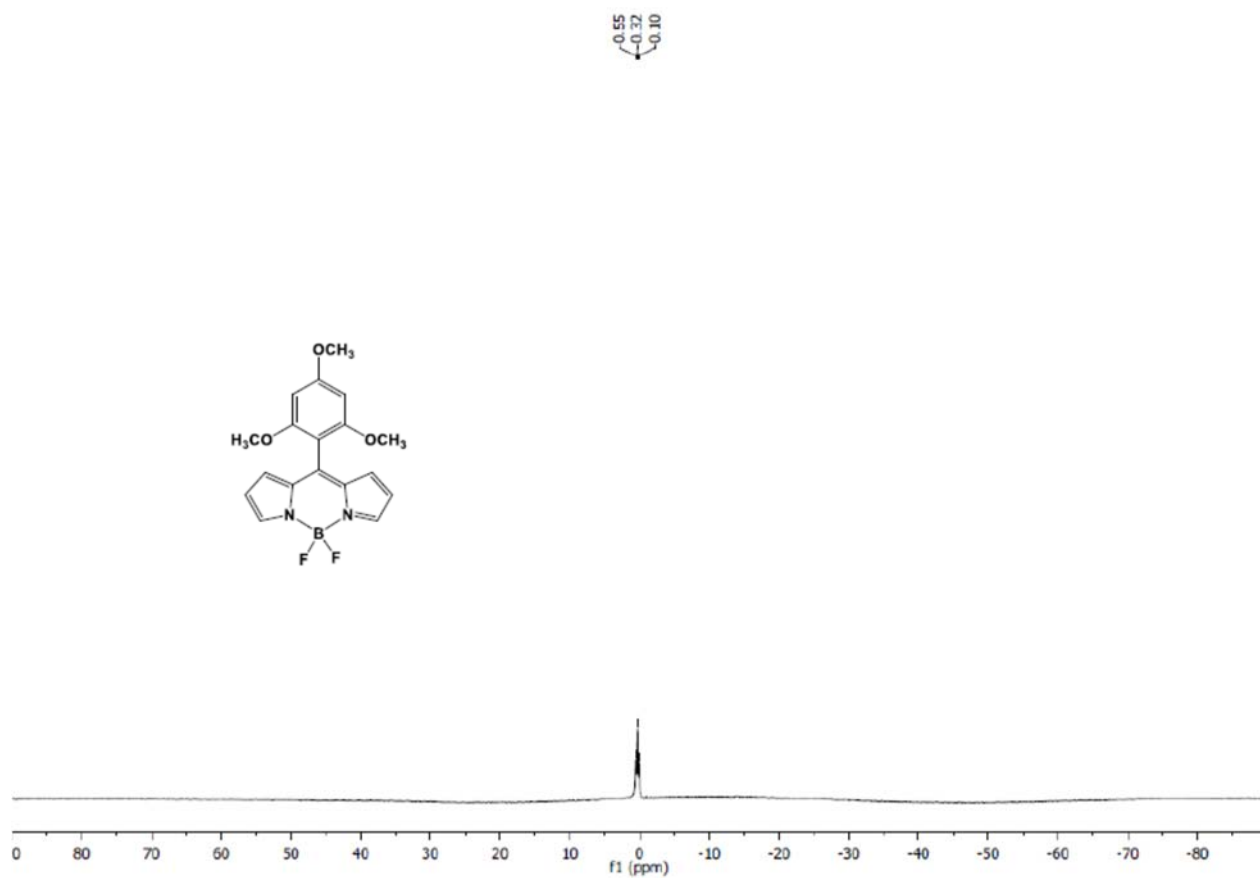


**Figure S19.**  $^{11}\text{B}$  NMR spectrum of **BDP-7** (128 MHz,  $\text{CDCl}_3$ , 25 °C).

Sample-ID		Station
Submitter		Supervisor
Analysis Name	AST-2020-14_RB1_01_23763.d	Acquisition Date
Sample Description		30/09/2020 12:09:25

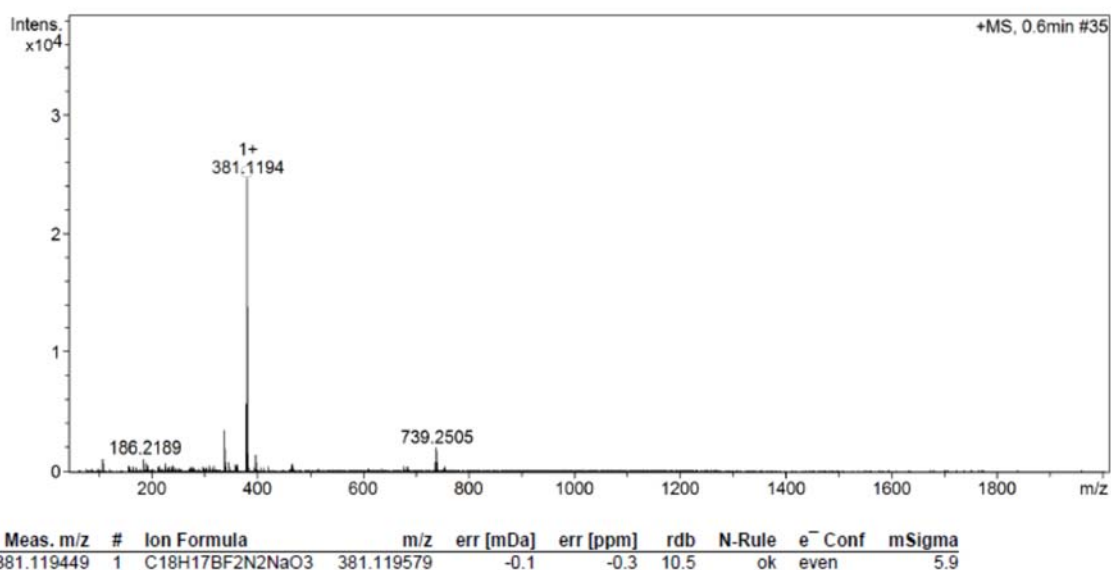


**Figure S20.** ESI-MS of **BDP 7**.

## 2.4 Crystallographic Data

A summary of values related to the crystal structure collections is presented in Table S2; Full crystallographic data is available from the Cambridge Crystallographic Data Centre at <https://www.ccdc.cam.ac.uk/structures/> under the deposition numbers listed in Table S2.

All non-H atoms were refined with anisotropic thermal parameters; H-atoms were constrained to geometrically idealized positions with isotropic thermal parameters riding on the bound C-atom (HFIX 43 and 137). No special constraints were placed on the molecules presented.

**Table S2.** Data relating to the crystal structure refinement of compounds **BDP 4-7**.

Identification code	BDP 4	BDP 5	BDP 6	BDP 7
Deposition Number (CCDC)	2069560	2069563	2069562	2069561
Chemical formula	C <sub>17.5</sub> H <sub>16</sub> BClF <sub>2</sub> N <sub>2</sub> O <sub>2</sub>	C <sub>17</sub> H <sub>15</sub> BF <sub>2</sub> N <sub>2</sub> O <sub>2</sub>	C <sub>18</sub> H <sub>17</sub> BF <sub>2</sub> N <sub>2</sub> O <sub>3</sub>	C <sub>18</sub> H <sub>17</sub> BF <sub>2</sub> N <sub>2</sub> O <sub>3</sub>
Formula weight	370.58 g/mol	328.12 g/mol	358.14 g/mol	358.14 g/mol
Crystal size (mm)	0.094 × 0.102 × 0.309	0.112 × 0.301 × 0.734	0.110 × 0.114 × 0.298	0.072 × 0.391 × 0.566
Crystal system	monoclinic	monoclinic	orthorhombic	triclinic
Space group	<i>P</i> 2 <sub>1</sub> / <i>c</i>	<i>P</i> 2 <sub>1</sub> / <i>n</i>	<i>P</i> 2 <sub>1</sub> 2 <sub>1</sub> 2 <sub>1</sub>	<i>P</i> -1
Unit cell dimensions				
a (Å)	12.5473(4)	10.9508(2)	7.5935(6)	9.4819(8)
b (Å)	20.8955(7)	7.63110(10)	9.4846(8)	9.5287(8)
c (Å)	14.4543(5)	18.1705(3)	23.2455(19)	10.2985(9)
α (°)	90	90	90	63.849(3)
β (°)	115.5179(14)	96.4790(8)	90	84.311(4)
γ (°)	90	90	90	79.654(3)
Volume (Å <sup>3</sup> )	3420.0(2)	1508.75(4)	1674.2(2)	821.43(12)
Z	8	4	4	2
ρ (calc.) (g/cm <sup>3</sup> )	1.439	1.445	1.421	1.448
2θ max. (°)	136.70	90.78	61.02	73.46
Radiation	CuK <sub>α</sub>	MoK <sub>α</sub>	MoK <sub>α</sub>	MoK <sub>α</sub>
Wavelength (Å)	1.54178	0.71073	0.71073	0.71073
Scan mode	ω and φ	ω and φ	ω and φ	ω and φ
Temperature (K)	100(2)	100(2)	100(2)	100(2)
Reflections collected	28641	139995	63985	53828
Independent reflections	6276	12704	5111	8150

<b>Absorption coefficient (mm<sup>-1</sup>)</b>	2.296	0.111	0.111	0.113
<b>Absorption correction</b>	Multi-Scan	Multi-Scan	Multi-Scan	Multi-Scan
<b>Max. and min. transmission</b>	0.7531 and 0.6219	0.7489 and 0.6689	0.7461 and 0.6228	0.7471 and 0.5839
<b>Structure solution technique</b>	direct methods	direct methods	direct methods	direct methods
<b>Structure solution program</b>	SHELXT 2018/2	SHELXT 2018/2	SHELXT 2018/2	SHELXT 2018/2
<b>Refinement program</b>	SHELXL-2018/3	SHELXL-2018/3	SHELXL-2018/3	SHELXL-2018/3
<b>Data / restraints / parameters</b>	6276 / 0 / 464	12704 / 0 / 219	5111 / 0 / 238	8150 / 0 / 238
<b>H-atom treatment</b>	constr.	constr.	constr.	constr.
<b>R1 (I&gt;2σ(I))</b>	0.0468,	0.0459	0.0455	0.0574
<b>R1 (all data)</b>	0.0522	0.0586	0.0727	0.0925
<b>wR2 (I&gt;2σ(I))</b>	0.1304	0.1165	0.1011	0.1507
<b>wR2 (all data)</b>	0.1353	0.1262	0.1143	0.1776
<b>Goodness-of-fit on F<sup>2</sup></b>	1.067	1.182	1.044	1.037
<b>Refinement Method</b>	Full-matrix least-squares on F <sup>2</sup>	Full-matrix least-squares on F <sup>2</sup>	Full-matrix least-squares on F <sup>2</sup>	Full-matrix least-squares on F <sup>2</sup>
<b>Largest diff. peak and hole (eÅ<sup>-3</sup>)</b>	0.904 and -1.102	0.738 and -0.282	0.295 and -0.243	0.696 and -0.464
<b>Flack parameter</b>	-	-	0.2(3) <sup>23</sup>	-

SHELXL-2018/3;<sup>24</sup> SHELXT-2018/2;<sup>25</sup> \*refined as a minimisation of  $\Sigma w(F_o^2 - F_c^2)^2$

## 2.5 Optical Spectra

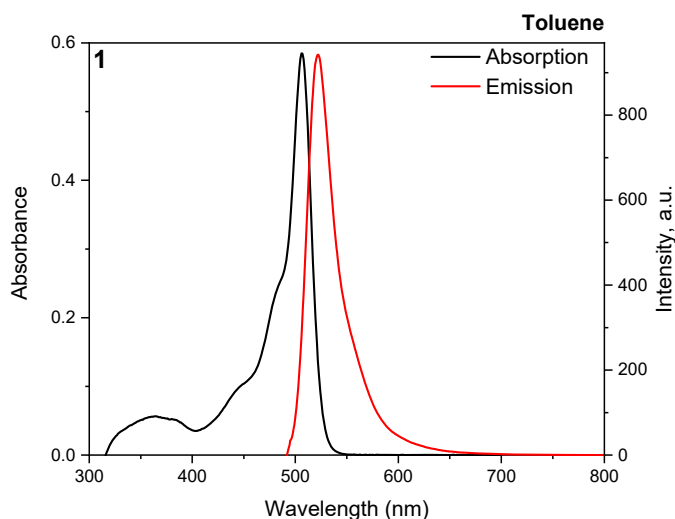


**Figure S21.** Absorption and emission spectra of **BDP-1**.

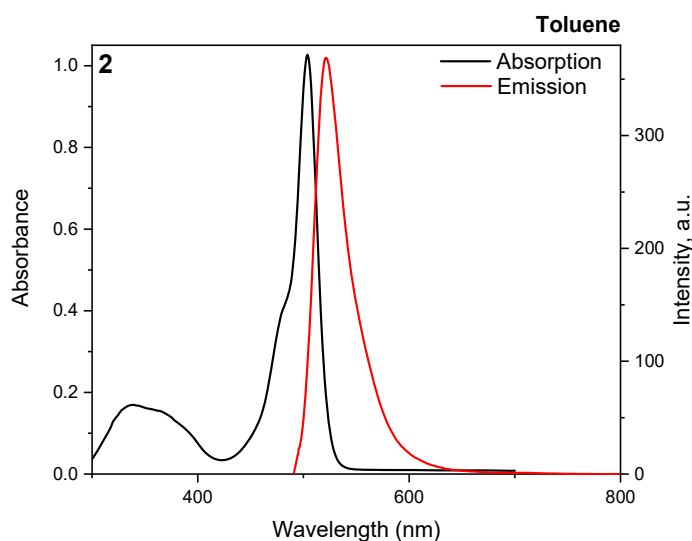


**Figure S22.** Absorption and emission spectra of **BDP-2**.

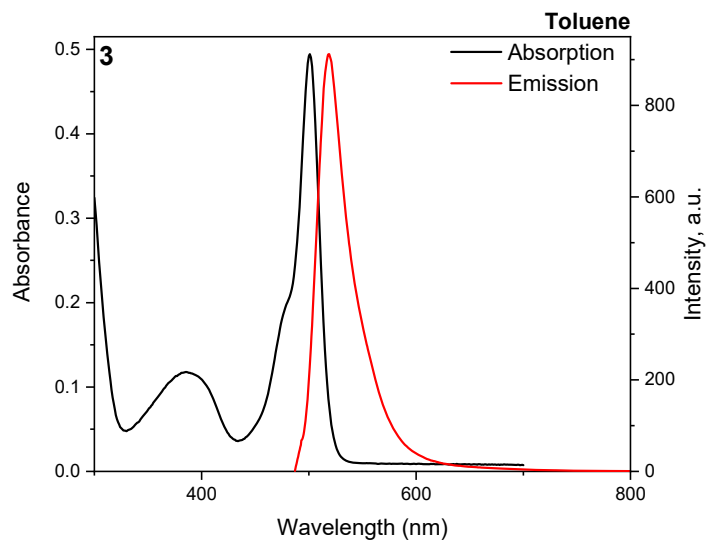


Figure S23. Absorption and emission spectra of **BDP-3**.

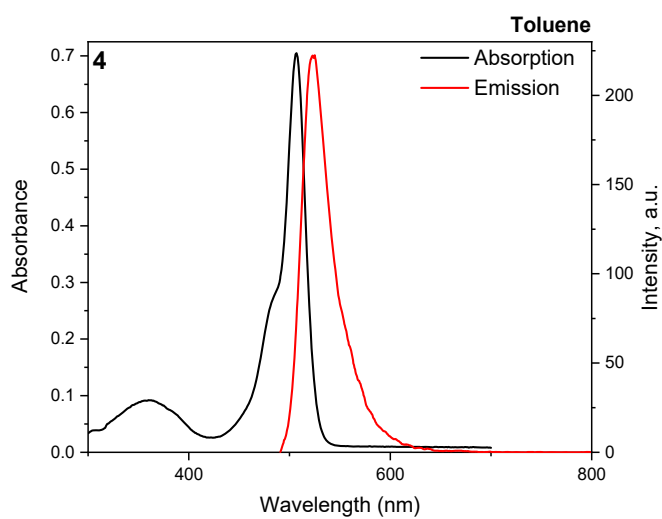


Figure S24. Absorption and emission spectra of **BDP-4**.

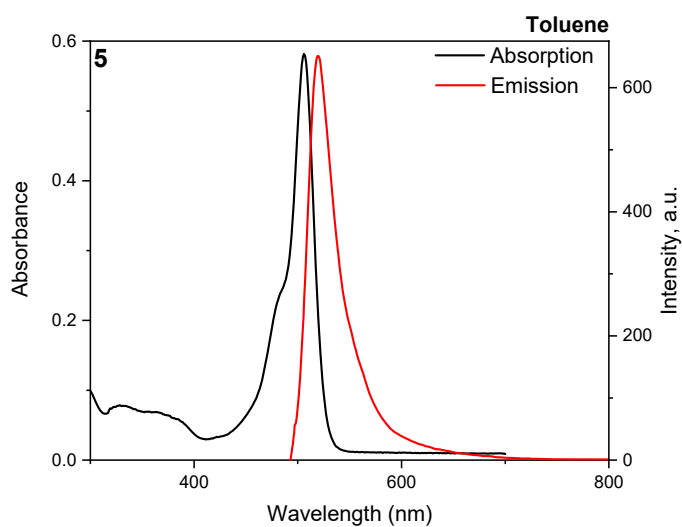


Figure S25. Absorption and emission spectra of **BDP-5**.



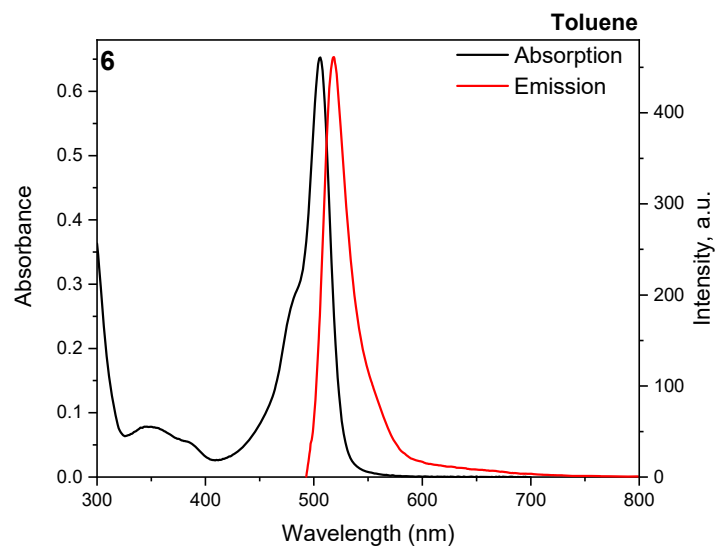


Figure S26. Absorption and emission spectra of **BDP-6**.

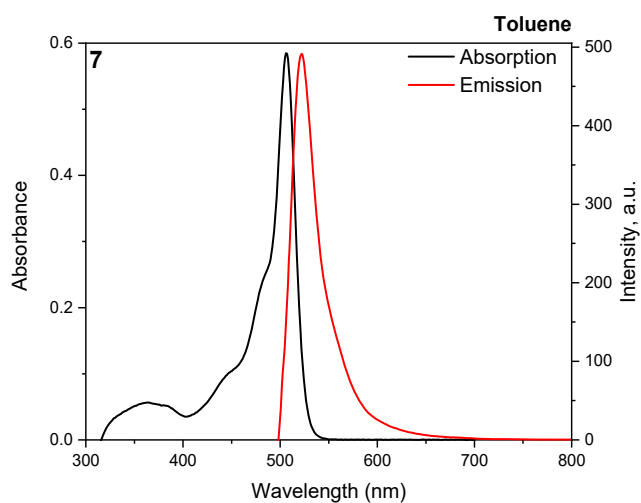


Figure S27. Absorption and emission spectra of **BDP-7**.

### 3. Computational methods and results

**Table S3.** Experimental and predicted Log  $\Phi_{\Delta}$  values of 48 BODIPYs according to Model 1 (toluene).

Compound	$\Phi_{\Delta}$ exp. %	Log $\Phi_{\Delta}$ exp.	Log $\Phi_{\Delta}$ pred.	Residual Log $\Phi_{\Delta}$
3	12	0.785	0.208	0.577
4	6.1	0.362	0.351	0.011
26	2.3	0.633	0.425	0.209
30	4.3	0.820	0.902	-0.082
31 <sup>test</sup>	6.6	0.580	0.993	-0.413
38	3.8	0.653	0.790	-0.137
40	4.5	1.000	1.060	-0.060
41 <sup>test</sup>	10	1.301	1.367	-0.066
42	20	1.041	0.986	0.055
48	11	0.934	1.205	-0.271
50	8.6	1.491	0.978	0.513
51	31	1.255	1.387	-0.132
53	18	1.828	1.743	0.085
54	67.3	1.391	1.270	0.121
55 <sup>test</sup>	24.6	0.903	1.272	-0.368
56	8	0.301	0.372	-0.071
58	2	1.623	1.697	-0.073
59	42	1.362	1.193	0.169
60	23	1.255	1.241	0.014
61	18	1.591	1.130	0.461
62	39	0.602	0.904	-0.302
63 <sup>test</sup>	4	0.000	0.393	-0.393
64	1	0.146	0.412	-0.266
66	1.4	0.699	0.731	-0.032
67	5	0.519	0.398	0.120
68	3.3	0.362	0.526	-0.164
69	2.3	0.919	1.004	-0.085
70	8.3	0.954	1.161	-0.207
71	9	1.041	0.879	0.162
72 <sup>test</sup>	11	1.279	1.123	0.156
73	19	1.505	1.539	-0.034
75	32	0.602	0.592	0.010
76	4	1.079	0.899	0.181
77	12	1.602	1.473	0.129
78 <sup>test</sup>	40	1.602	1.656	-0.054
79	40	1.477	1.676	-0.199
80 <sup>test</sup>	30	1.477	1.290	0.187
81	30	1.380	1.249	0.131
82 <sup>test</sup>	24	1.643	1.363	0.280
83	44	1.158	0.990	0.169
84 <sup>test</sup>	14.4	0.000	0.257	-0.257
BDP-1 <sup>ext</sup>	1	-0.046	0.513	-0.559
BDP-2 <sup>ext</sup>	0.9	-0.301	0.169	-0.470
BDP-3	0.5	-0.301	0.146	-0.447
BDP-4	0.5	0.342	0.948	-0.606
BDP-5 <sup>ext</sup>	2.2	1.400	0.947	0.452
BDP-6	25.1	1.199	1.146	0.052
BDP-7 <sup>ext</sup>	15.8	1.041	0.959	0.082

**Table S4.** Experimental and predicted Log  $\Phi_{\Delta}$  values of 45 BODIPYs according to Model 2 (acetonitrile).

Compound	$\Phi_{\Delta}$ exp. %	Log $\Phi_{\Delta}$ exp.	Log $\Phi_{\Delta}$ pred.	Residual Log $\Phi_{\Delta}$
3 test	6.9	0.839	0.832	0.007
4	1.7	0.230	0.286	-0.056
9 test	2	0.301	0.450	-0.149
10	0.44	-0.357	-0.253	-0.104
11 test	0.43	-0.367	-0.062	-0.304
12 test	0.49	-0.310	-0.784	0.474
13	2.4	0.380	0.175	0.205
14 test	3.7	0.568	0.299	0.269
15	18	1.255	1.048	0.207
16 test	18	1.255	1.500	-0.245
17 test	12.5	1.097	1.030	0.067
18	3.3	0.519	0.715	-0.197
19	31	1.491	1.326	0.165
20	6.2	0.792	1.427	-0.635
21	5.2	0.716	0.532	0.184
22	8.3	0.919	1.085	-0.166
23	5.7	0.756	0.520	0.236
24	8.3	0.919	1.026	-0.107
25	3.3	0.519	0.405	0.114
26	5.7	0.756	1.070	-0.314
27	87.2	1.941	1.414	0.526
28	8.1	0.908	0.454	0.454
29	1.1	0.041	0.377	-0.335
30	8.4	0.924	0.718	0.206
31 test	9.2	0.964	0.992	-0.028
38	22	1.342	1.598	-0.255
40	84	1.924	1.254	0.670
41	11	1.041	1.408	-0.366
42	0.5	-0.301	-0.352	0.051
48	34	1.531	1.446	0.086
51	11	1.041	1.051	-0.010
65	0.9	-0.046	-0.232	0.186
67	2.4	0.380	0.500	-0.120
68	54	1.732	1.370	0.362
74	2.9	0.462	0.807	-0.344
81	25	1.398	1.257	0.141
83	11.2	1.049	1.111	-0.062
84	3	0.477	0.701	-0.224
BDP-1 ext	4.1	0.613	0.263	0.350
BDP-2 ext	0.4	-0.398	-0.241	-0.157
BDP-3	0.7	-0.155	-0.180	0.025
BDP-4	5.9	0.771	0.914	-0.143
BDP-5 ext	0.3	-0.523	0.084	-0.607
BDP-6	0.4	-0.398	-0.017	-0.381
BDP-7 ext	19.3	1.286	0.965	0.321

**Table S5.** Experimental and predicted Log  $\Phi_{\Delta}$  values of 41 BODIPYs according to Model 3 (THF).

Compound	$\Phi_{\Delta}$ exp. %	Log $\Phi_{\Delta}$ exp.	Log $\Phi_{\Delta}$ pred.	Residual Log $\Phi_{\Delta}$
1	7.1	0.851	0.533	0.318
3 <sup>test</sup>	9.1	0.959	0.905	0.054
4	13	1.114	1.000	0.114
9	2.6	0.415	0.382	0.033
10	2.8	0.447	0.468	-0.021
11	1.9	0.279	0.420	-0.141
12	2.6	0.415	-0.079	0.494
13 <sup>test</sup>	1.2	0.079	0.154	-0.075
14	2.4	0.380	0.704	-0.324
15	6.1	0.785	0.757	0.029
16	5.1	0.708	0.891	-0.183
17	46.2	1.665	0.962	0.702
18	35.7	1.553	1.179	0.373
19	5.9	0.771	0.834	-0.063
20	62.3	1.794	1.672	0.122
21	32.1	1.507	1.547	-0.041
22	61.2	1.787	1.682	0.105
23 <sup>test</sup>	40.1	1.603	1.580	0.024
24	53.5	1.728	1.750	-0.022
25	33.8	1.529	1.694	-0.165
26	13	1.114	0.912	0.202
27 <sup>test</sup>	23.2	1.365	1.782	-0.417
28 <sup>test</sup>	44.2	1.645	1.522	0.124
29	19	1.279	1.505	-0.226
30	15	1.176	1.175	0.001
31 <sup>test</sup>	6.6	0.820	0.820	-0.001
38	21	1.322	1.103	0.219
48	20	1.301	1.409	-0.108
51	21	1.322	1.353	-0.031
63	0.3	-0.523	-0.551	0.028
64	0.6	-0.222	-0.255	0.034
65 <sup>test</sup>	0.8	-0.097	-0.495	0.398
66	0.4	-0.398	-0.003	-0.395
81	86	1.934	1.738	0.197
BDP-1 <sup>ext</sup>	1.1	0.041	0.561	-0.519
BDP-2 <sup>ext</sup>	0.8	-0.097	0.433	-0.530
BDP-3	2.1	0.322	0.399	-0.077
BDP-4	3.6	0.556	0.847	-0.290
BDP-5 <sup>ext</sup>	6.1	0.785	0.800	-0.015
BDP-6	1.1	0.041	0.926	-0.885
BDP-7 <sup>ext</sup>	36.3	1.560	1.139	0.421

#### 4. Singlet oxygen generation quantum yields measurements

The singlet oxygen quantum yield measurements were performed according to the literature.<sup>26</sup> Solutions of the <sup>1</sup>O<sub>2</sub> trap, 1,9-dimethylantracene (DMA), with an optical density of around 1.4 in air-saturated solvent (acetonitrile, toluene, and tetrahydrofuran respectively) were employed. Corresponding BODIPY was added to the cuvette, and its absorbance was adjusted to around 0.29 at the wavelength of irradiation. The solutions in the cuvette were irradiated with 514 nm laser light at a constant power density of 12 mW cm<sup>-2</sup>. The absorption spectra of the solutions were measured every 30 - 90 s. The slope of plots of absorbance of DMA at 376 nm vs. irradiation time for each photosensitizer was calculated.

Singlet oxygen quantum yields were calculated based on the equation:

$$\Phi_{\Delta} = \Phi_{\Delta}^{ref} \times \frac{k}{k_{ref}} \times \frac{I_{abs}^{ref}}{I_{abs}}$$

where  $\Phi_{\Delta}$  is the singlet oxygen quantum yield; the superscript ref stands for 2,6-diiodoBODIPY (0.85 in toluene)<sup>27</sup>;  $k$  is the slope of the curves of DMA absorption (376 nm) change vs. irradiation time;  $I_{abs}$  represents the absorption correction factor which is given by  $I = 1 - 10^{-OD}$  (OD is the optical density at 514 nm).

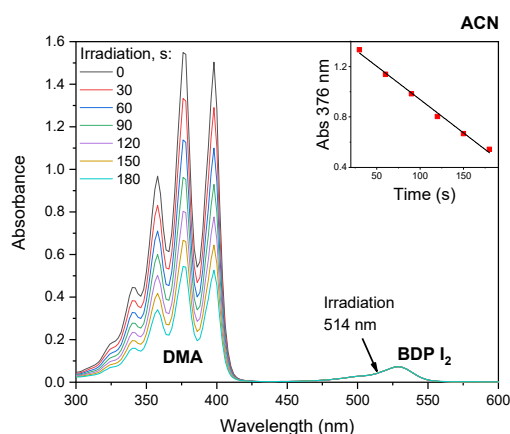


**Figure S28.** Photooxidation of 1,9-dimethylantracene in air-saturated acetonitrile solution containing reference photosensitizer - 2,6-diiodoBODIPY. Inset: dependence of absorbance at 376 nm on the irradiation time.

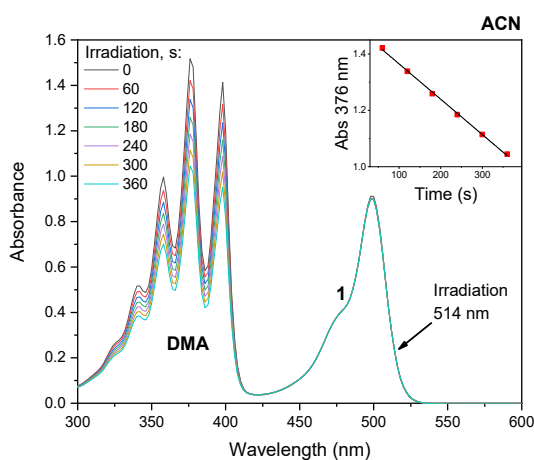


**Figure S29.** Photooxidation of 1,9-dimethylantracene in air-saturated acetonitrile solution containing BDP-1. Inset: dependence of absorbance at 376 nm on the irradiation time.

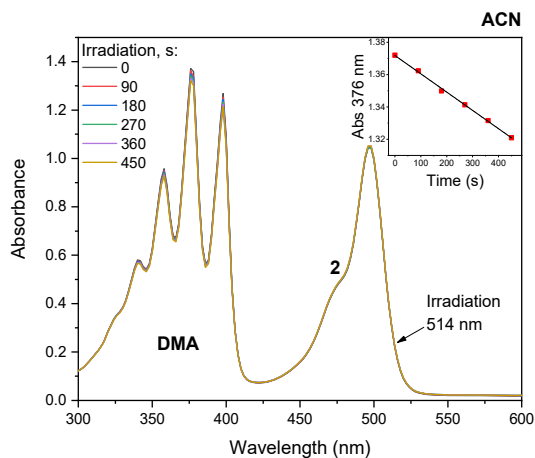


**Figure S30.** Photooxidation of 1,9-dimethylantracene in air-saturated acetonitrile solution containing BDP-2. Inset: dependence of absorbance at 376 nm on the irradiation time.

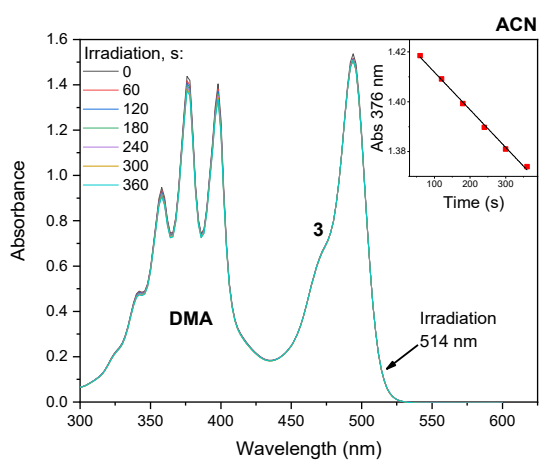


**Figure S31.** Photooxidation of 1,9-dimethylantracene in air-saturated acetonitrile solution containing BDP-3. Inset: dependence of absorbance at 376 nm on the irradiation time.

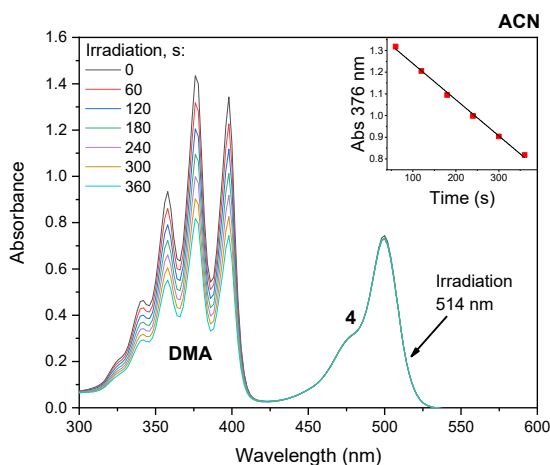


**Figure S32.** Photooxidation of 1,9-dimethylantracene in air-saturated acetonitrile solution containing BDP-4. Inset: dependence of absorbance at 376 nm on the irradiation time.

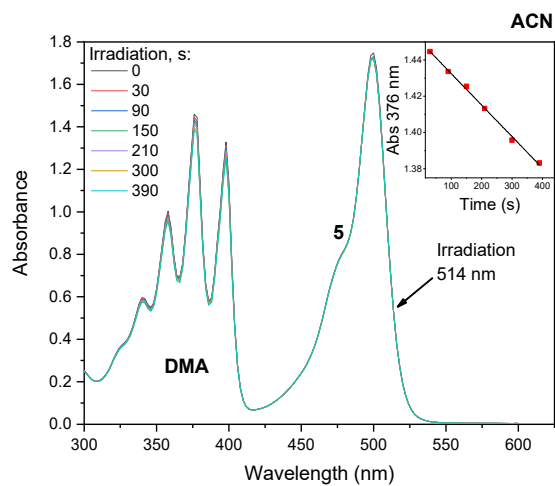


**Figure S33.** Photooxidation of 1,9-dimethylantracene in air-saturated acetonitrile solution containing BDP-5. Inset: dependence of absorbance at 376 nm on the irradiation time.

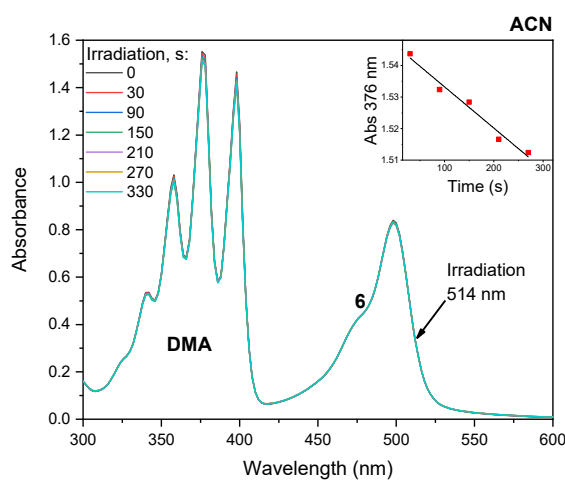


**Figure S34.** Photooxidation of 1,9-dimethylantracene in air-saturated acetonitrile solution containing BDP-6. Inset: dependence of absorbance at 376 nm on the irradiation time.

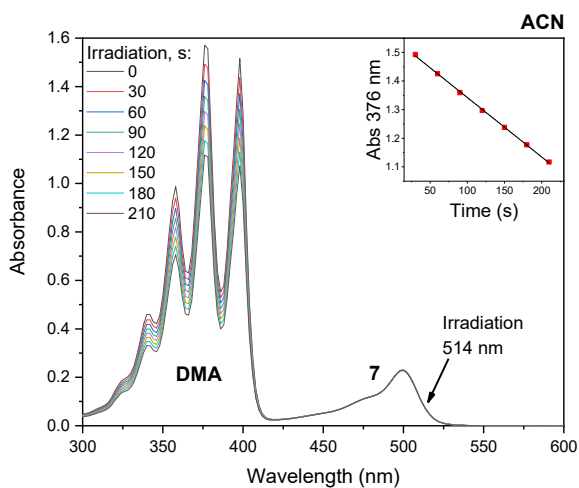


**Figure S35.** Photooxidation of 1,9-dimethylantracene in air-saturated acetonitrile solution containing BDP-7. Inset: dependence of absorbance at 376 nm on the irradiation time.

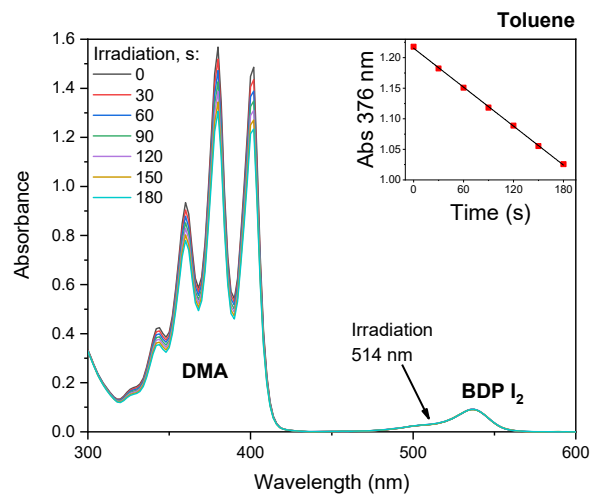


**Figure S36.** Photooxidation of 1,9-dimethylantracene in air-saturated toluene solution containing reference photosensitizer - 2,6-diiodoBODIPY. Inset: dependence of absorbance at 376 nm on the irradiation time.

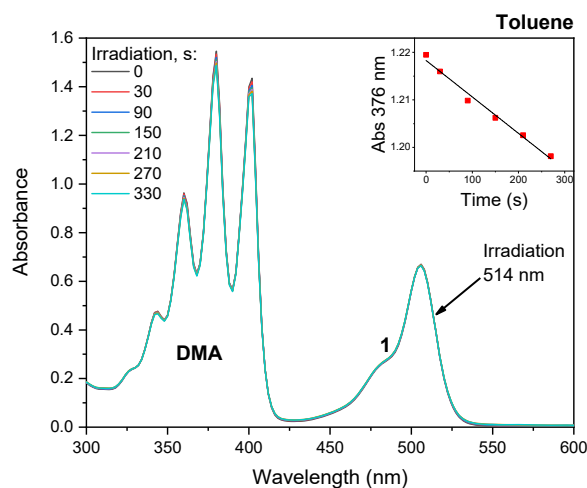


**Figure S37.** Photooxidation of 1,9-dimethylantracene in air-saturated toluene solution containing BDP-1. Inset: dependence of absorbance at 376 nm on the irradiation time.

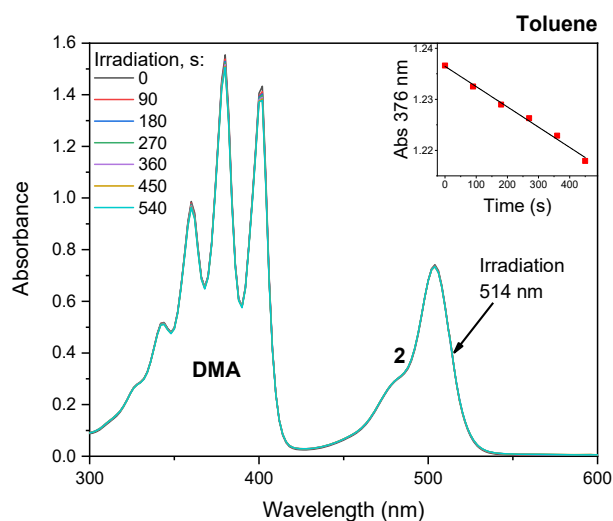


**Figure S38.** Photooxidation of 1,9-dimethylantracene in air-saturated toluene solution containing BDP-2. Inset: dependence of absorbance at 376 nm on the irradiation time.



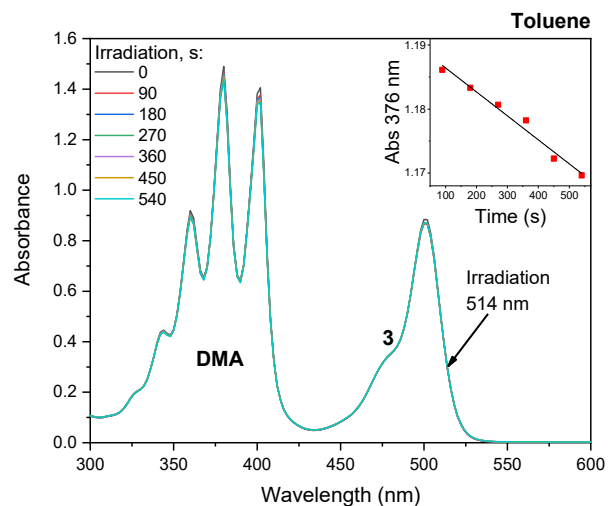


**Figure S39.** Photooxidation of 1,9-dimethylanthracene in air-saturated toluene solution containing BDP-3. Inset: dependence of absorbance at 376 nm on the irradiation time.

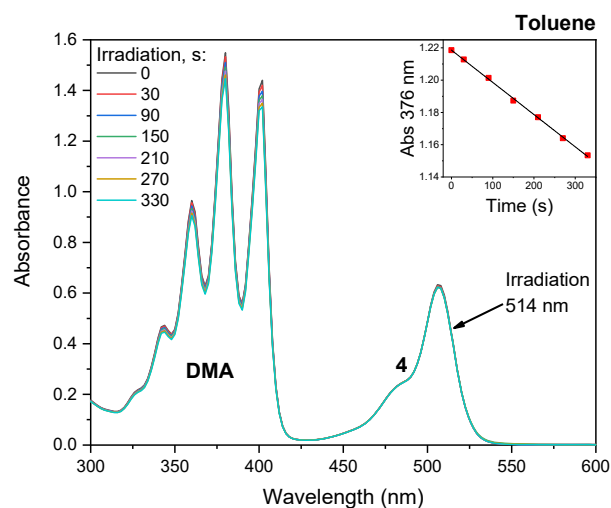


**Figure S40.** Photooxidation of 1,9-dimethylanthracene in air-saturated toluene solution containing BDP-4. Inset: dependence of absorbance at 376 nm on the irradiation time.

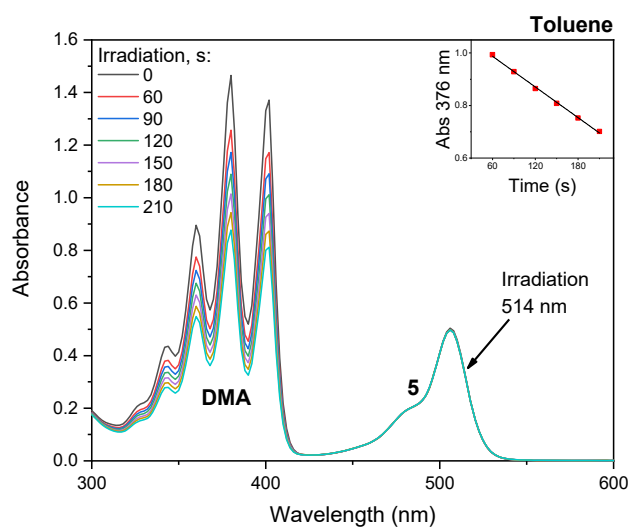


**Figure S41.** Photooxidation of 1,9-dimethylanthracene in air-saturated toluene solution containing BDP-5. Inset: dependence of absorbance at 376 nm on the irradiation time.

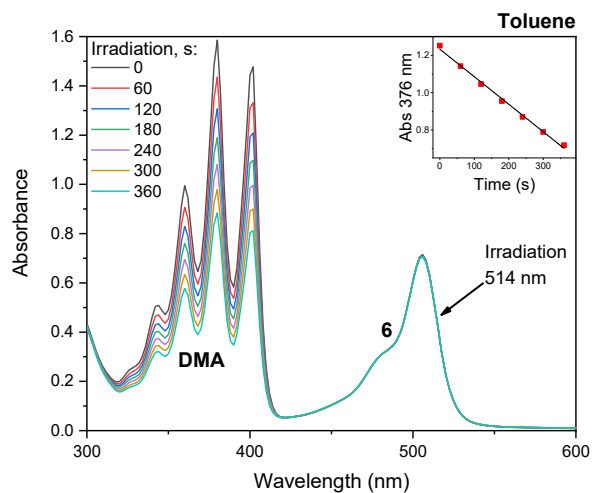


**Figure S42.** Photooxidation of 1,9-dimethylantracene in air-saturated toluene solution containing BDP-6. Inset: dependence of absorbance at 376 nm on the irradiation time.

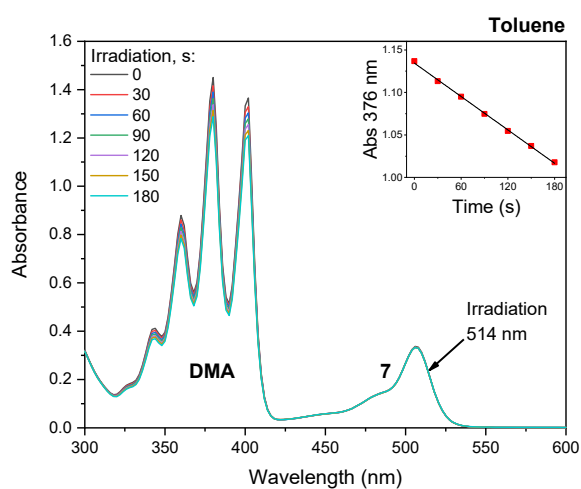


**Figure S43.** Photooxidation of 1,9-dimethylantracene in air-saturated toluene solution containing BDP-7. Inset: dependence of absorbance at 376 nm on the irradiation time.

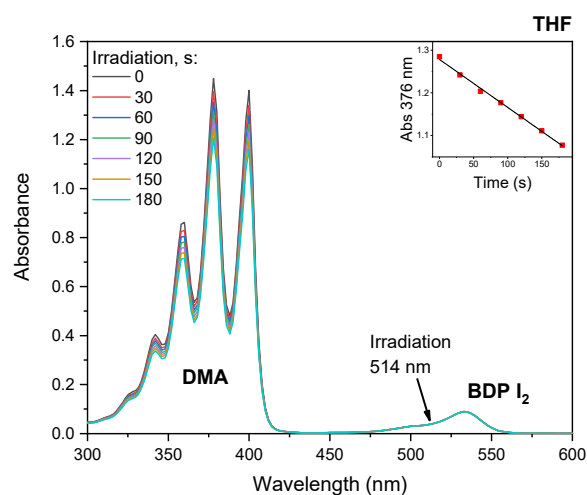


**Figure S44.** Photooxidation of 1,9-dimethylantracene in air-saturated THF solution containing reference photosensitizer - 2,6-diiodobodipy. Inset: dependence of absorbance at 376 nm on the irradiation time.

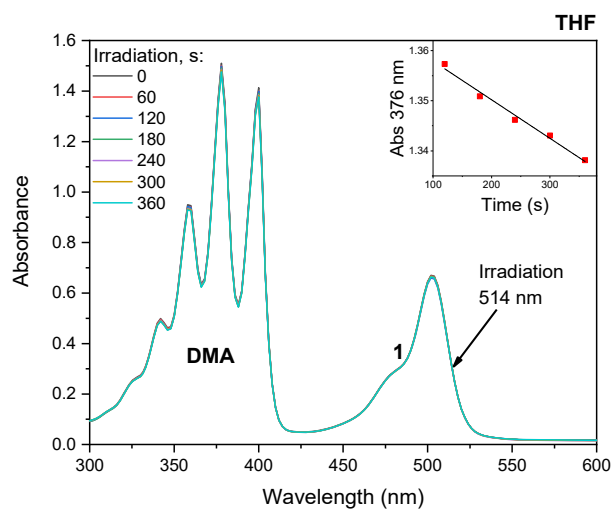


**Figure S45.** Photooxidation of 1,9-dimethylantracene in air-saturated THF solution containing **BDP-1**. Inset: dependence of absorbance at 376 nm on the irradiation time.

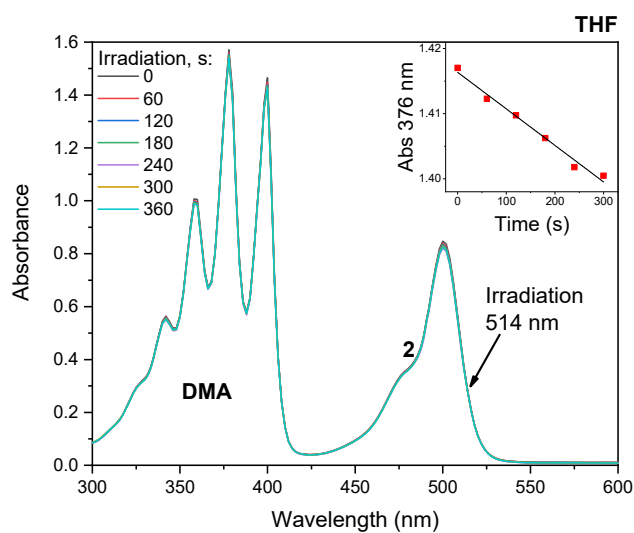


**Figure S46.** Photooxidation of 1,9-dimethylantracene in air-saturated THF solution containing **BDP-2**. Inset: dependence of absorbance at 376 nm on the irradiation time.

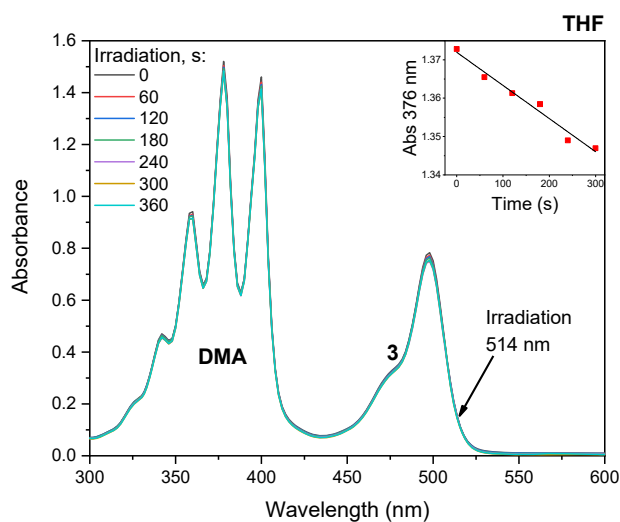


**Figure S47.** Photooxidation of 1,9-dimethylantracene in air-saturated THF solution containing **BDP-3**. Inset: dependence of absorbance at 376 nm on the irradiation time.

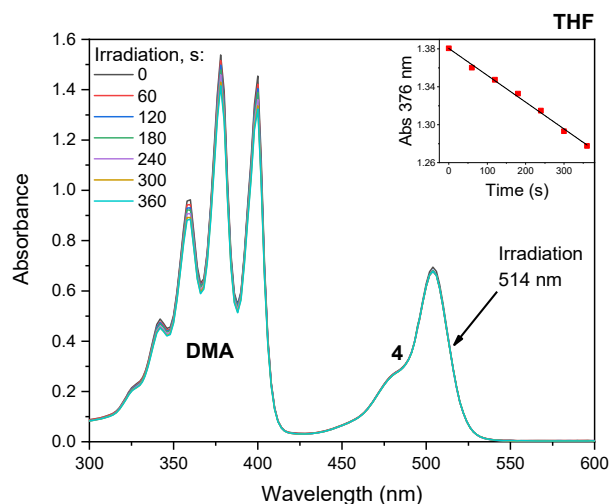


**Figure S48.** Photooxidation of 1,9-dimethylantracene in air-saturated THF solution containing **BDP-4**. Inset: dependence of absorbance at 376 nm on the irradiation time.

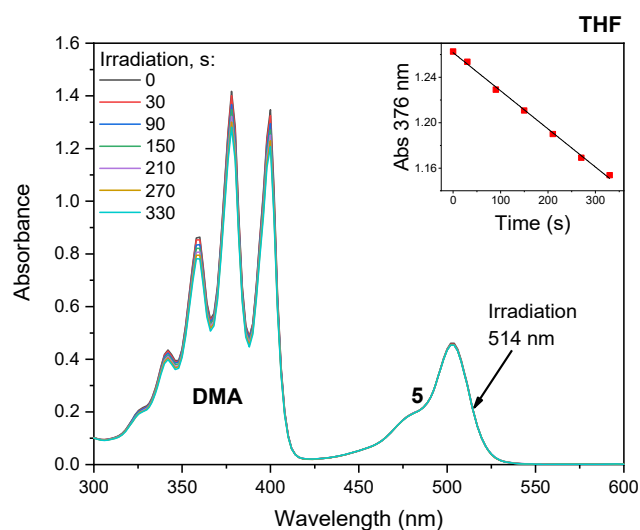


**Figure S49.** Photooxidation of 1,9-dimethylantracene in air-saturated THF solution containing **BDP-5**. Inset: dependence of absorbance at 376 nm on the irradiation time.

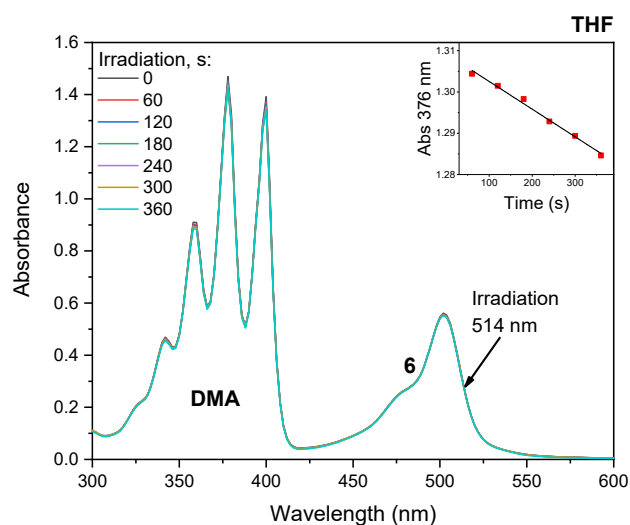


**Figure S50.** Photooxidation of 1,9-dimethylantracene in air-saturated THF solution containing **BDP-6**. Inset: dependence of absorbance at 376 nm on the irradiation time.

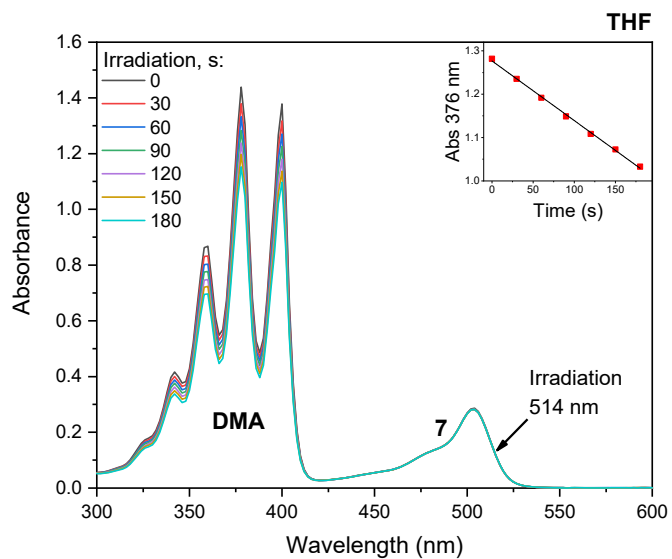


**Figure S51.** Photooxidation of 1,9-dimethylantracene in air-saturated THF solution containing **BDP-7**. Inset: dependence of absorbance at 376 nm on the irradiation time.

## 5. Supplemental Crystal Structure Images

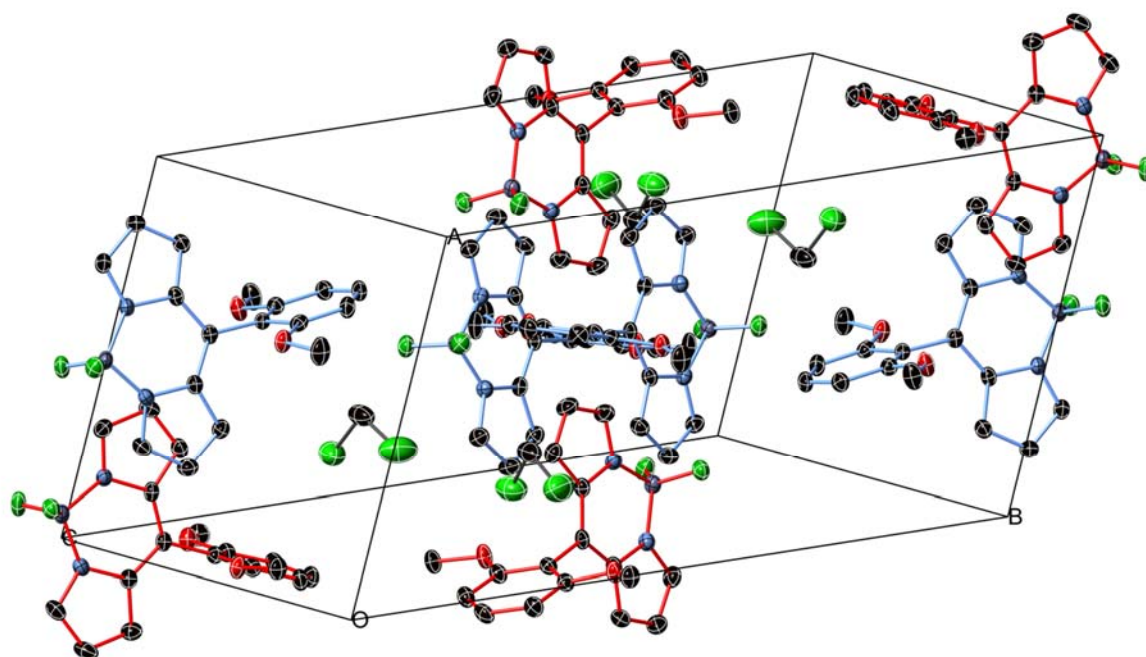


**Figure S52.** View of the crystallographic unit cell of **BDP-4·½(DCM)**, with the two inequivalent molecules (containing C1 and C101) shown in blue and red bonds, respectively; Thermal ellipsoids are shown at the 50% probability level, H-atoms omitted from view.

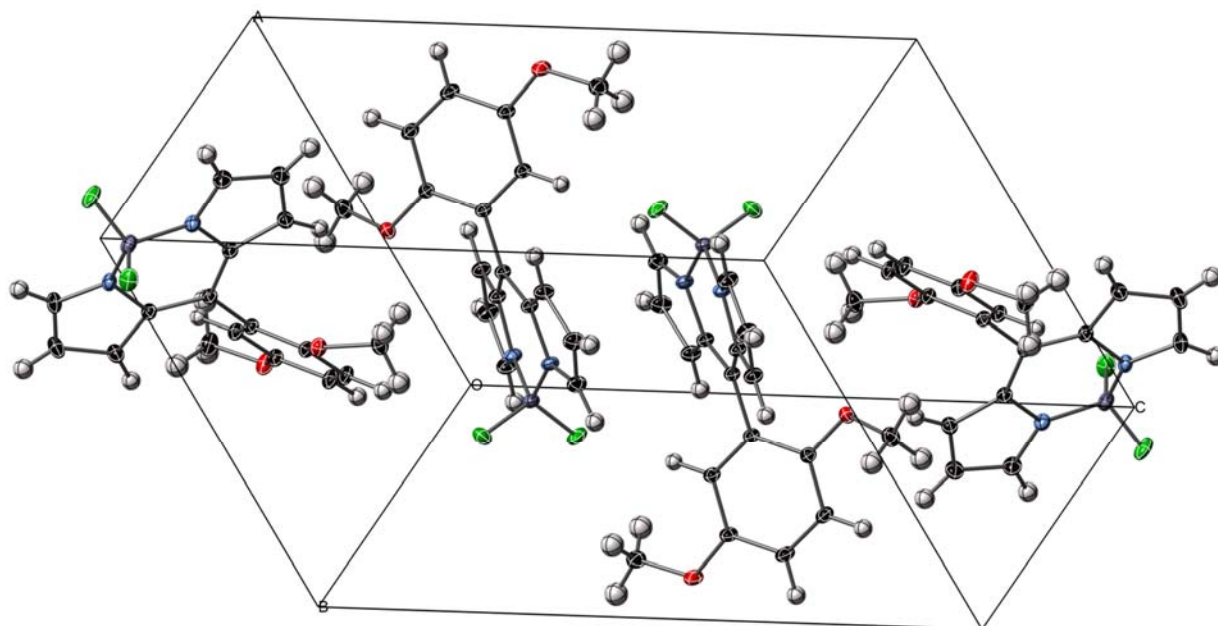


**Figure S53.** View of the crystallographic unit cell of **BDP-5**; Thermal ellipsoids are shown at the 50% probability level.

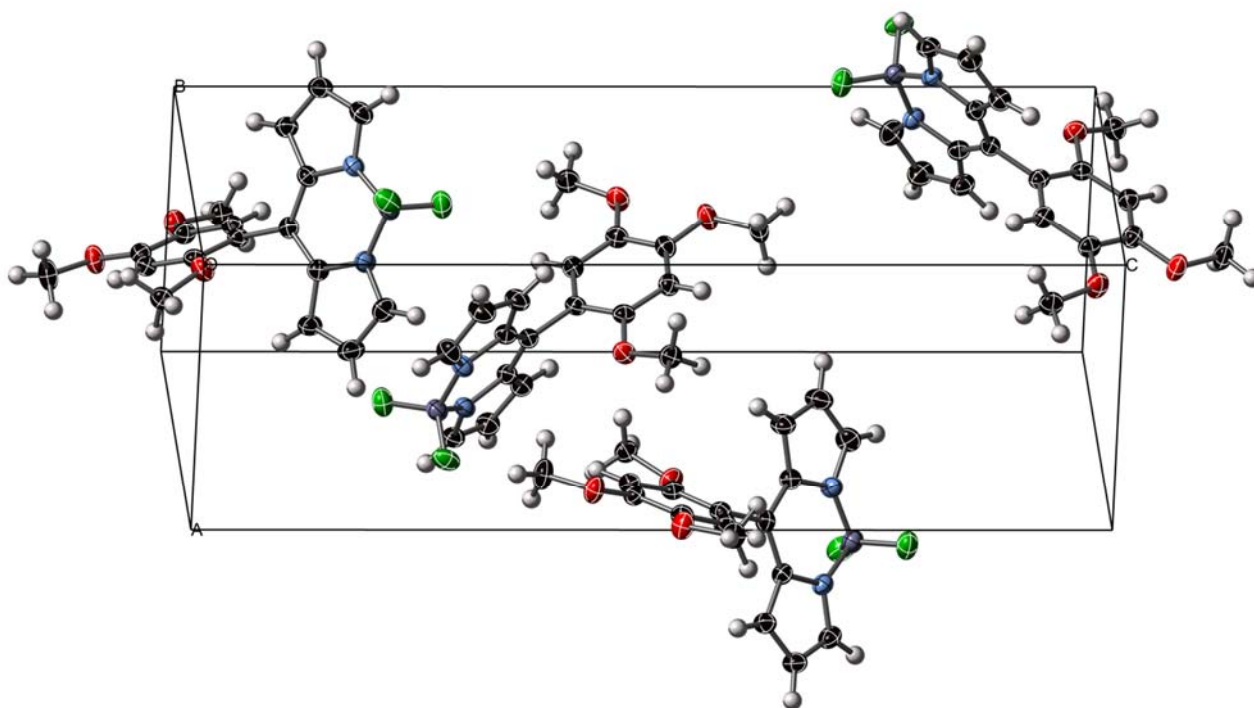


**Figure S54.** View of the crystallographic unit cell of BDP-6; Thermal ellipsoids are shown at the 50% probability level, H-atoms are represented as spheres of fixed radius.

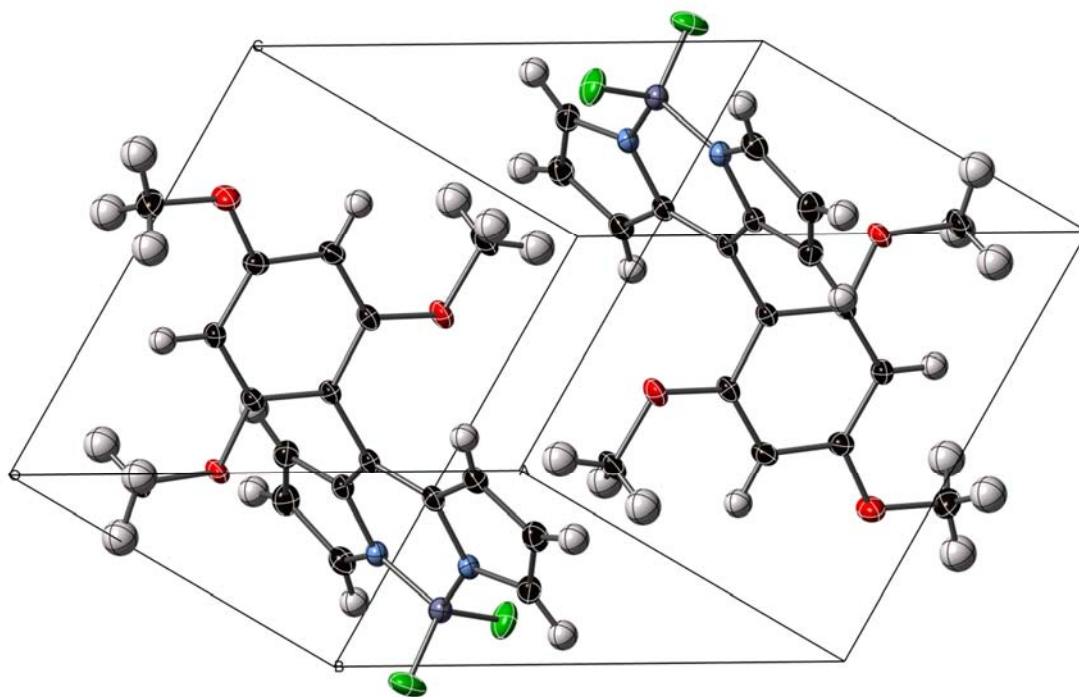


**Figure S55.** View of the crystallographic unit cell of BDP-7; Thermal ellipsoids are shown at the 50% probability level.

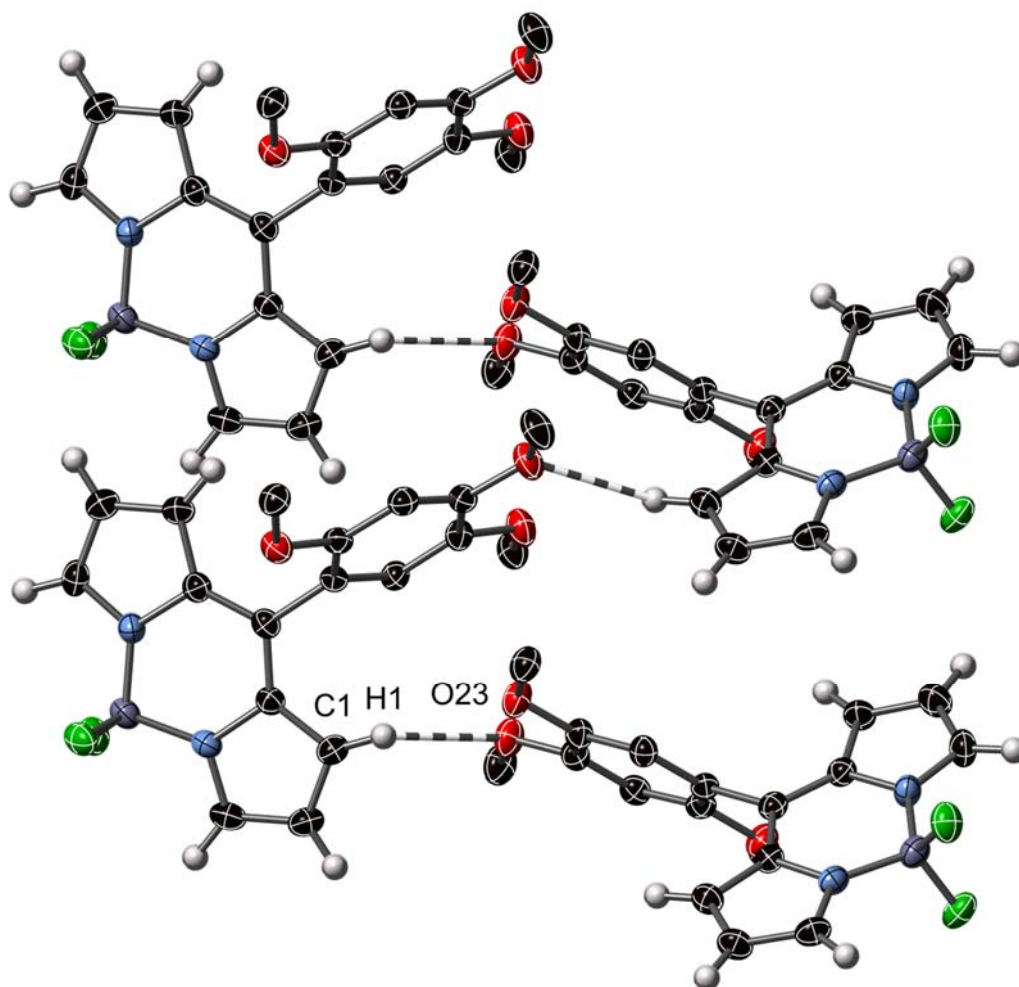


**Figure S56.** Intermolecular C-H $\cdots$ O interactions in the crystal structure of BDP-6, at 3.28 Å C $\cdots$ O; Thermal ellipsoids are shown at the 50% probability level, H-atoms are represented as spheres of fixed radius.



## 6. References

---

- <sup>1</sup> X.-F. Zhang, J. Zhu, *J. Luminescence*, 2019, **205**, 148.
- <sup>2</sup> X.-F. Zhang, N. Feng, *Spectrochim. Acta A*, 2018, **189**, 13.
- <sup>3</sup> W. Hu, M. Liu, X.-F. Zhang, Y. Wang, Y. Wang, H. Lan, H. Zhao, *J. Phys. Chem. C*, 2019, **123**, 15944.
- <sup>4</sup> X.-F. Zhang, N. Feng, *Chem. Asian J.*, 2017, **12**, 2447.
- <sup>5</sup> W. Hu, Y. Lin, X.-F. Zhang, M. Feng, S. Zhao, J. Zhang, *Dyes Pigm.*, 2019, **164**, 139.
- <sup>6</sup> W. Hua, X.-F. Zhang, X. Lu, S. Lan, D. Tian, T. Li, L. Wang, S. Zhao, M. Feng, J. Zhang, *J. Lumin.*, 2018, **194**, 185.
- <sup>7</sup> W. Hua, X.-F. Zhang, X. Lu, S. Lan, D. Tian, T. Li, L. Wang, S. Zhao, M. Feng, J. Zhang, *Dyes Pigm.*, 2018, **149**, 306.
- <sup>8</sup> M.A. Filatov, S. Karuthedath, P.M. Polestshuk, S. Callaghan, K.J. Flanagan, M. Telitchko, T. Wiesner, F. Laquai, M.O. Senge, *Phys. Chem. Chem. Phys.*, 2018, **20**, 8016.
- <sup>9</sup> Z. Wang, J. Zhao, *Org. Lett.*, 2017, **19**, 4492.
- <sup>10</sup> M.A. Filatov, S. Karuthedath, P.M. Polestshuk, S. Callaghan, K. Flanagan, T. Wiesner, F. Laquai, M.O. Senge, *ChemPhotoChem*, 2018, **2**, 606.
- <sup>11</sup> Z. Wang, M. Ivanov, Y. Gao, L. Bussotti, P. Foggi, H. Zhang, N. Russo, B. Dick, J. Zhao, M. Di Donato, G. Mazzone, L. Luo, M. Fedin, *Chem. Eur. J.*, 2020, **26**, 1091.
- <sup>12</sup> Z. Wang, J. Zhao, M. Di Donato, G. Mazzone, *Chem. Commun.*, 2019, **55**, 1510.
- <sup>13</sup> K. Chen, W. Yang, Z. Wang, A. Iagatti, L. Bussotti, P. Foggi, W. Ji, J. Zhao, M. Di Donato, *J. Phys. Chem. A*, 2017, **121**, 7550.
- <sup>14</sup> Y. Dong, A.A. Sukhanov, J. Zhao, A. Elmali, X. Li, B. Dick, A. Karatay, V.K. Voronkova, *J. Phys. Chem. C*, 2019, **123**, 22793.
- <sup>15</sup> Y. Dong, A. Elmali, J. Zhao, B. Dick, A. Karatay, *ChemPhysChem*, 2020, **21**, 1388.
- <sup>16</sup> K. Chen, M. Taddei, L. Bussotti, P. Foggi, J. Zhao, M. Di Donato, *ChemPhotoChem*, doi: 10.1002/cptc.201900294
- <sup>17</sup> Y. Hou, I. Kurganskii, A. Elmali, H. Zhang, Y. Gao, L. Lv, J. Zhao, A. Karatay, L. Luo, M. Fedin, *J. Chem. Phys.*, 2020, **152**, 114701.
- <sup>18</sup> V.-N. Nguyen, Y. Yim, S. Kim, B. Ryu, K. M. K. Swamy, G. Kim, N. Kwon, C.-Y. Kim, S. Park, J. Yoon, *Angew. Chem. Int. Ed.*, 2020, **59**, 8957.
- <sup>19</sup> B. Ventura, G. Marconi, M. Bröring, R. Krüger, L. Flamigni, *New J. Chem.*, 2009, **33**, 428.
- <sup>20</sup> L. Ya, J. Zhao, A. Iagatti, L. Bussotti, P. Foggi, E. Castellucci, M. Di Donato, K. Han, *J. Phys. Chem. C*, 2018, **122**, 2502.
- <sup>21</sup> N. Epelde-Elezcano, E. Palao, H. Manzano, A. Prieto-CastaCeda, A.R. Agarrabeitia, A. Tabero, A. Villanueva, S. de la Moya, C. Ljpez-Arbeloa, V. Martinez-Martinez, M.J. Ortiz, *Chem. Eur. J.*, 2017, **23**, 4837
- <sup>22</sup> M. Taniguchi and J. S. Lindsey, *Photochem. Photobiol.*, 2018, **94**, 290.
- <sup>23</sup> S. Parsons, H. D. Flack, T. Wagner, *Acta Cryst.*, **2013**, B69, 249.
- <sup>24</sup> G. M. Sheldrick, *Acta Cryst.*, **2015**, C71, 3.
- <sup>25</sup> G. M. Sheldrick, *Acta Cryst.*, **2015**, A71, 3.
- <sup>26</sup> L. Gou, C. N. Coretsopoulos and A. B. Scranton, *J. Polym. Sci. Part A Polym. Chem.*, 2004, **42**, 1285.
- <sup>27</sup> Y. Zhao, R. Duan, J. Zhao and C. Li, *Chem. Commun.*, 2018, **54**, 12329.